Development of an X-band Radar Depth Inversion Model at the Sand Motor

J. Friedman

MSc Thesis

TU Delft Delft University of Technology

Deltares Enabling Delta Life

Development of an X-band Radar Depth Inversion Model at the Sand Motor

Master of Science Thesis

J. Friedman

June 4, 2014

Graduation committee:	
prof. dr. ir. M. Stive	Delft University of Technology (Chairman)
prof. dr. ir. A. Reniers	Delft University of Technology
ir. A. Luijendijk	Deltares, Delft University of Technology
ir. R. Hoekstra	Deltares
ir. C. Swinkels	Deltares
ir. M. Radermacher	Delft University of Technology

Department of Hydraulic Engineering
Faculty of CiTG, Delft University of Technology
Delft, The Netherlands
www.citg.tudelft.nl

Unit of Hydraulic Engineering
Deltares
Rotterdamseweg 185
Delft, The Netherlands
www.deltares.nl

Abstract

A large-scale nourishment known as the Sand Motor has been implemented along the Dutch coast as a *"Building with Nature"* solution designed for the upcoming 20 years. Given the longterm period of the project, a combination of *in situ* measurements and remote sensing techniques are currently in use. An X-band radar system is deployed at the Sand Motor, but requires further research into its applicability in such a dynamic coastal climate. Radar data can be processed into hydrodynamic parameters such as waves, currents and bathymetry information through use of a 3D Fast Fourier Transform (FFT). This technology is highly desirable for coastal engineering applications since it presents a relatively effortless method to capture high resolution spatial and temporal hydrodynamic parameters.

The objective of this research is to develop an X-band radar depth inversion model at the Sand Motor for further investigation into remote sensing as an accurate tool for estimating nearshore bathymetry and hydrodynamics. The developed model should be able to accurately estimate hydrodynamic parameters from raw X-band radar images with high temporal and spatial resolution.

This thesis explains the development, calibration and validation of the **X**-band **M**ATLAB® Fitting (**XM**Fit) model at the Sand Motor for a single storm in October 2013. **XM**Fit proved to be a valuable remote sensing tool for extracting nearshore hydrodynamics based on *in situ* comparisons. The SeaDarQ software developed by Nortek B.V. is also used as a quality benchmark. The storm results showed that **XM**Fit is more robust and accurate relative to the currently available SeaDarQ software.

A sensitivity analysis was completed to further analyze the spatial and temporal patterns associated with **XM**Fit accuracy. Spatial statistics indicated high error around the edges of the radar domain, which led to a reduced radar footprint by implementing a spatial cutoff of 2.5 km. The smaller domain results in much less scatter with a near-constant linear bias of 2 m. The following metocean limits were found to be associated with periods of high accuracy in **XM**Fit.

- Significant wave height greater than **1 m**
- Wind speed should be greater than **12 m/s**
- Wind and waves should align within **45°**

The metocean limits help conclude that **XM**Fit requires spectra spreading in $k - \omega$ space to help *constrain* the dispersion shell. This finding directly links with locally generated wind waves, more commonly referred to as *wind sea*. Ideal results based on the spatial and temporal limits further reduced the linear bias to approximately 1.6 m. The ideal conditions show a much better agreement between radar-derived and *in situ* bathymetry and hydrodynamics.

A relationship between the inaccuracy of **XM**Fit during flood tide was linked to complex nearshore hydrodynamics around the Sand Motor. Note that the flood tide at the Sand Motor exhibits complex flow structures (i.e. stratification and large scale eddy formation on the lee side). **XM**Fit averages these complex 3D flow structures evident during flood tide into a single large computational cube, which drastically simplifies the hydrodynamics.

Lastly, this work concludes by emphasizing the need for additional research into **XM**Fit since it proved applicable at the Ameland inlet along the Dutch coast. Instantaneous results increase confidence in **XM**Fit given its ability to extract the complex ebb-tidal delta, the orientation of the flood channel and coherent wave-induced currents.

Table of Contents

List of Figures

List of Tables

Acknowledgements

First of all, I would like to acknowledge the members of my committee who supervised me throughout this thesis work - prof. Marcel Stive, prof. Ad Reniers, Arjen Luijendijk, Roderik Hoekstra, Cilia Swinkels and Max Radermacher. Thank you all for keeping me focused on the end result and providing insightful guidance along the way. It was a pleasure to present and exchange ideas during our frequent meetings.

I would also like to extend my gratitude to Nortek B.V., whose cooperation and contact was instrumental in both learning more about the SeaDarQ system and building a working relationship. The results presented in this report would not be as exciting without the help of Javier Perez and Jos van Heesen. Thank you.

I would like to specifically thank Tim for helping me recognize the importance of olive oil and Pieter for opening my eyes to the world north of Amsterdam. A thank you is also necessary for all students working at Deltares in the tetra building for keeping me sane throughout this thesis work. The frequent coffee breaks were always an excellent distraction from working.

Last but certainly not least, thank you Kristina for enduring my perpetual radar chatter and for always reminding me that *"my flow is too strong!"*

Enjoy the report!

Josh Friedman
Delft, June 2014

Chapter 1

Introduction

Marine radar is typically situated on-board a ship for navigational purposes, but can also assess the surrounding hydrodynamic conditions. This is done using the sea clutter or commonly referred to as Bragg scatter, which is the interaction of the electromagnetic signal with small wind ripples on the sea surface (Nieto Borge et al., 2004). This interaction can be exploited by analyzing a specific band of the electromagnetic spectrum (8.0 to 12.0 GHz), known as the X-band (Dankert et al., 2003b). The signal can be processed into hydrodynamic parameters such as waves, currents and bathymetry information through use of a 3D Fast Fourier Transform (FFT) of the raw radar images.

The large swath of X-band radar coupled with its high frequency rotation results in high resolution spatial and temporal data, which exceeds the capabilities of typical *in situ* methods. Thus, this technology is highly desirable for coastal engineering applications since it presents a relatively effortless method to capture high resolution spatial and temporal hydrodynamic parameters.

Remote sensing using X-band radar systems for coastal engineering purposes is still a relatively young technology. X-band radar depth inversion algorithms have been rather common since the publication of Bell (1999) but lack robustness. There have been plenty of novel uses for X-band radar in the coastal environment such as, but not limited to:

- Dankert et al. (2003a) developed routines to extract wave groups in space and time,
- McNinch (2007) used a mobile X-band radar system to measure nearshore sandbars and maximum runup; and
- Ruessink et al. (2002) computed the location of submerged sandbar crests with X-band images.

Although there is plenty of published literature surrounding the use of X-band radar technology for deriving hydrodynamics, it still requires more research to prove its reliability in coastal environments.

In October 2011, a large-scale nourishment along the Dutch coast was implemented as a *"Building with Nature"* solution, a concept pioneered by Stive et al. (2013). The nourishment

project, hereafter referred to as the Sand Motor, has been designed to redistribute sediment along the Dutch coast over the next 20 years (Stive et al., 2013). The extremely unique and large-scale project requires an intensive fieldwork campaign to monitor its dynamic progression. Given the longterm period of the project, a combination of *in situ* measurements and remote sensing techniques are currently in use (Wengrove et al., 2013). An X-band radar system configured with commercial SeaDarQ software is located on-site since it proved applicable from previous work on the Dutch Coast; see Swinkels et al. (2012).

The aim of this report is to *develop an X-band radar depth inversion model at the Sand Motor for further investigation into remote sensing as an accurate tool for estimating nearshore bathymetry and hydrodynamics.*

This report is outlined as follows. Chapter 2 presents the necessary wave and radar theory, including a short description of two commercial radar systems - SeaDarQ and WaMoS II. This is followed by the main research goal, which is posed in Chapter 3. All datasets used for the analysis are presented in Chapter 4. The development of the depth inversion algorithm, **XM**Fit, is fully detailed in Chapter 5, followed by a validation of the underlying theory (Chapter 6). A comparison between the newly developed **XM**Fit, *in situ* data and SeaDarQ is presented in Chapter 7. A sensitivity analysis is included in Chapter 8, which leads to final conclusions (Chapter 9) and further recommendations (Chapter 10).

Chapter 2

Literature Review

This literature review is focused on the derivation of X-band radar hydrodynamic estimates. It begins with the applicable linear wave theory, followed by an overview of marine X-band radar and its processing technique. A description of two commercial systems is also included - SeaDarQ and the **Wa**ve and Surface Current **Mo**nitoring **S**ystem (WaMoS II). This chapter concludes by examining the potential accuracy of X-band radar estimates from previous documented applications.

2.1 Nearshore Hydrodynamics

The dynamic interaction between shallow bathymetry, waves, and currents in the nearshore are of crucial importance to coastal engineers. The combination of these forcings result in sediment transport, which has the potential (depending on directionality) to reshape the coastline. This is an iterative process since changed bathymetry influences the waves and currents, which in turn influences further morphological changes, etc ... commonly referred to as *morphodynamics*.

First and foremost, knowledge of nearshore processes is important to protect the general public. Decisions can be made from coastal modeling simulations, which require specific inputs. Detailed bathymetry is a key input for accurate nearshore modeling. It is arguably the most influential input when modeling, designing or making any sort of coastal decision (i.e. flooding hazards, dredging channels, swimmer safety).

Good bathymetric data is a necessity for understanding and characterizing the nearshore environment. Unfortunately the collection of accurate bathymetric data is not a simple task. It requires a laborious setup of many instruments, is typically costly and limited in both spatial and temporal resolutions. Any possible alternatives to this method are highly desirable given the relative expense in obtaining bathymetric data. The same limitation is evident with current measuring devices, such as acoustic doppler current profilers (ADCPs). They measure temporal current information throughout the water column (assuming they are deployed vertically), but require multiple devices for spatial knowledge of flow structures.

An inherit technical limitation with *in situ* measuring techniques is the requirement to be, by definition, in the environment. This typically requires *ideal* hydrodynamic conditions for either deployment, operation and/or retrieval. It is also important to note that these instruments require regular maintenance since they are exposed to the elements. For these reasons, it is of great importance to further develop remote sensing techniques that can estimate nearshore hydrodynamics. *Remote sensing has the capability for high resolution spatial and temporal hydrodynamics - an extremely valuable input for coastal engineers.*

Remote sensing techniques have their own limitations. Indirect measurements require relationships to infer properties of the desired hydrodynamics. Remote sensing typically outputs too much data, given the high spatial and temporal resolution. Lastly, remote sensing data is quite noisy due to poor weather conditions (e.g. fog, rain, etc...). More details can be found in Holman and Haller (2013).

2.1.1 Linear Wave Theory

A short description of the necessary linear wave theory for analyzing surface waves is presented in this section. The linear wave theory follows the underlying random-phase/amplitude model, which describes the sea surface as a sum of a large number of statistically independent, harmonic wave components (Holthuijsen, 2007). The linear wave theory is derived by the combination of two fundamental equations - continuity equation and momentum balance. A solution is only possible with boundary conditions that describe the physical system. A *dynamic* boundary condition requires constant pressure at the water surface, while *kinematic* boundary conditions state that fluid particles may not leave the surface or penetrate the bottom (Holthuijsen, 2007). The solution to these equations results in freely propagating harmonic waves,

$$\eta(x,t) = a\sin(\omega t - kx) \tag{2.1}$$

where η describes the surface elevation as a function of time (t) and space (x), a describes the amplitude of the propagating wave, ω is the radian frequency ($= 2\pi/T$), and k is the wave number ($= 2\pi/L$), Note that T is the wave period and L is the wavelength. The *dynamic* boundary condition also gives more insight into the propagation speed of different wave frequencies. The radian frequency, ω, and the wave number, k, are related through the linear dispersion relation,

$$\omega = \sqrt{gk\tanh(kd)} \tag{2.2}$$

where g is the gravitational constant and d is the water depth. This highlights that the propagation speed ω/k depends on frequency, which means that low frequency waves travel faster than high frequency waves (Holthuijsen, 2007). The linear dispersion relation is the core physical concept behind the depth inversion method explained in Chapter 2.2.

2.1.2 Inherit Limitations

The linear dispersion relation (Equation 2.2) is limited in deep and very shallow water. This is extremely influential since it only provides knowledge of the underlying bottom topography

under specific conditions. Wave are insensitive to the bathymetry in deep water (i.e. orbital wave motion does not reach the bed), shown by the resulting dispersion relation in deep water ($\omega = \sqrt{gk_0}$). Shallow water depths result in the opposite effect, where wave motion fully interacts with the bed (Holthuijsen, 2007). This results in non-dispersive shallow water waves that are not dependent on wavelength or frequency ($\omega = k\sqrt{gd}$). The interaction with the bed introduces non-linearities such as shoaling, which poses significant issues with the applicability of linear wave theory in shallow water depth (Holthuijsen, 2007). The importance of relative water depth is visualized in Figure 2.1.

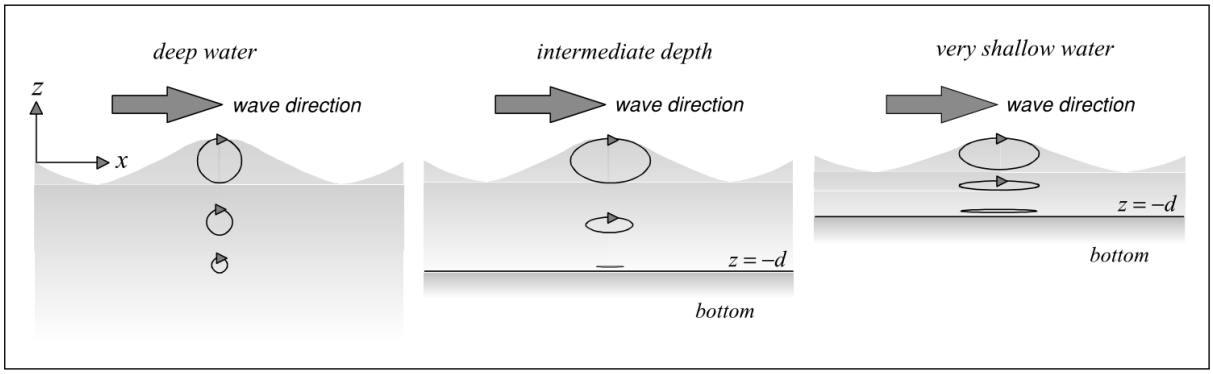

Figure 2.1: Orbital Motion in Various Water Depths (Holthuijsen, 2007)

Lastly, it is of importance to briefly highlight several important assumptions that are made when deriving the linear wave theory. The following idealizations should not be ignored.

- Ideal Fluid
  - Assumes an incompressible fluid with a constant density (i.e. no stratification)
- Continuous Water Body
  - Assumes fluid is void of any air bubbles, not valid during wave breaking
- Subjected to a Single External Force
  - Neglects other external forcing mechanisms
- Small-Amplitude Approximation
  - Assumes that wave heights are small relative to the water depth (i.e. not applicable in shallow water)

2.2 Marine X-band Radar

Radio **D**etection **a**nd **R**anging (RADAR), is a common remote sensing technique that uses the Doppler shift in space and time of returned microwaves to infer intensity characteristics. The reflected microwave pulses are a function of surface type, which increases for rough sea surfaces (Rutten, 2013). The X-band segment of the electromagnetic spectrum (8 to 12 GHz) is used for coastal sea state measurements since it returns high radial resolution over a relatively small area (Dankert et al., 2003b).

The typical setup of a marine X-band radar unit consists of a rotating antenna that sends (and later receives) pulses over a specific beam width and direction. This process is repeated until the entire area is covered (i.e. a full rotation). The temporal resolution of radar derived data is limited by the antenna rotation time, while its spatial resolution is dependent on the azimuth resolution and the pulse length (Nieto Borge et al., 2004). More background regarding radar specifics (i.e. ripple modulation) is presented in Young et al. (1985), Alpers et al. (1981), Dankert et al. (2003b), Nieto Borge et al. (2004), Flampouris (2010), etc...

2.2.1 Processing Technique

The following procedure is referred to as the Global Method, first documented by Young et al. (1985). It starts by using the continual rotation of the radar antenna to produce sea clutter images in polar coordinates in time. The raw sea clutter images are interpolated to a Cartesian grid. The continual rotation is discretized into timestacks (i.e. number of images), which is then broken into computational cubes of size N_i, N_i, and N_ω. This is shown in Figure 2.2. The N_i is typically several hundred pixels, while N_ω is the number of images analyzed (Nieto Borge et al., 2004).

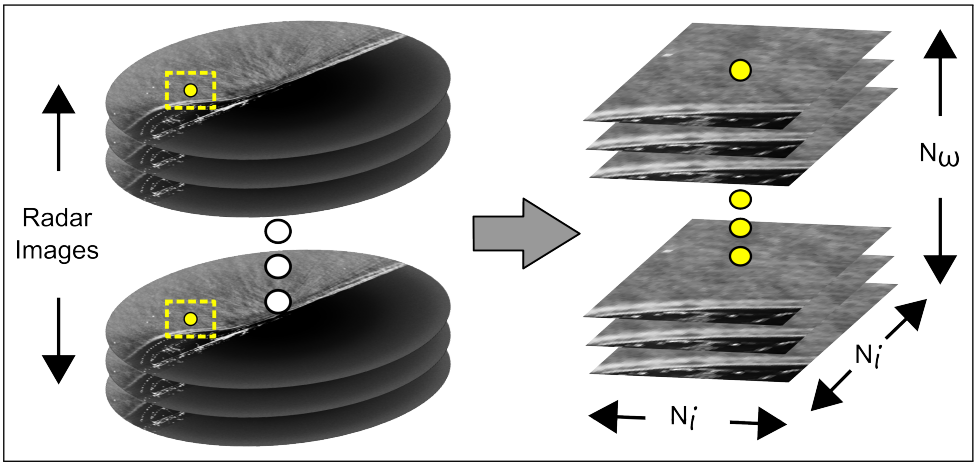

Figure 2.2: Explanation of a Computational Cube

3D Image Spectra

Each computational cube of varying backscatter intensity contains wavelength and frequency information (Nieto Borge et al., 2004). This information is extracted by means of a 3D Fast

Fourier Transform originally explained by Young et al. (1985). The output from the FFT analysis gives wavelength information (k_x and k_y) in space and their corresponding frequency (ω). Rutten (2013) describes the scatter of wave numbers and frequency as the unfiltered and uncorrected (i.e. for currents) 3D image spectrum $I(k_x, k_y, \omega)$.

Fitting the Linear Dispersion Relation

The processing technique of the computational cubes assumes the validity of the linear wave theory. It is assumed that the wave components visible in the radar image follow the random-phase/amplitude model for random waves. Thus, the 3D image spectrum should fit the 3D linear dispersion relation. A perfect fit is **not** expected since the hydrodynamics present (i.e. waves and currents) influence the image spectrum by altering the shell due to a Doppler shift (Dankert et al., 2003b). The doppler-shifted linear dispersion relation is defined as

$$\omega = \sqrt{gk \tanh(kd)} + \vec{U} \cdot \vec{k} \tag{2.3}$$

where $\vec{U}$ is the mean water velocity vector and $\vec{k}$ is the wave number vector. A visual of the theoretical and a Doppler-shifted (due to hydrodynamics) dispersion shell is in Figure 2.3. The current vector ($\vec{U}$) and depth (d) information are extracted by fitting the 3D image spectra with the theoretical dispersion relation, commonly referred to as depth inversion. This is completed by applying a spectral threshold to distinguish spectra noise.

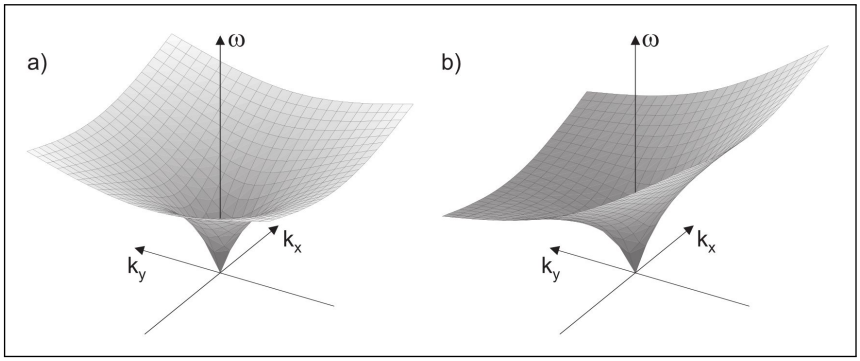

Figure 2.3: Intrinsic and Doppler-Shifted Linear Dispersion Relation (Dankert et al., 2003b)

Lastly, it should be made clear that it is not possible to identify a current vector influencing the intrinsic dispersion shell if it is exactly perpendicular to the wave direction since it is not evident in the image spectra as a doppler-shift in frequency. The following two sections investigate two depth inversion algorithms - DiSC and SeaDarQ.

DiSC Algorithm

The **Di**spersive **S**urface **C**lassificator (DiSC) algorithm is used within the WaMoS II system. It uses nautical X-band radar to measure directional ocean wave spectra in real time. It measures significant wave height (H_{m_0}), peak wave period (Tp) and peak wave direction (θ_p), and the surface current speed (U) and direction (θ_u) (OceanWaves GmbH, 2010). High

resolution current and bathymetry estimates are currently available through an extension. A validation study is available by OceanWaves GmbH (2010), which only investigates wave conditions at an offshore platform, a coastal station and a moving vessel.

Senet et al. (2008) explains the internal algorithm, which is introduced as an alternative to extracting wave parameters from the dispersion shell by "*allowing for inhomogeneous image sequences of dynamic and dispersive surfaces*". The DiSC algorithm differs from the Global Method since it incorporates the complex spectra, directional filtering, and spectra decomposition.

The non-linear fitting method iteratively solves the global minimum of the cost function (i.e. minimum of the sum of squares),

$$f(u_x, u_y, d) = \sum_{l=0}^{L-1} \left(\sqrt{g\vec{k_1} \tanh(\vec{k_1} d)} + k_{x,1} u_x + k_{y,1} u_y - \omega \right)^2 \tag{2.4}$$

where u_x and u_y are the components of the near-surface current and d is the unknown water depth. The index l represents the number of selected spectra coordinates (k_{x_1}, k_{y_1}) that are determined based on an energy threshold that identifies spectral signal from noise.

SeaDarQ Algorithm

The SeaDarQ X-band radar system is primarily used and first commercialized for oil spill detection, but can also extract hydrodynamic parameters (Nortek B.V., 2013). The fully automated oil spill detection relies on surface roughness to track oil clusters since oil reduces both roughness and backscatter intensity.

The SeaDarQ software follows the image spectra approach presented by Young et al. (1985) in the previous section. It fits the 3D image spectra to the linear dispersion relation in two dimensions by compensating for both the depth and current vector estimate iteratively. The algorithm finds the global minimum of the non-linear sum of squares based on the doppler-shifted linear dispersion relation (Equation 2.3). This information is unfortunately not published, but was made available through close collaboration with Nortek B.V.

Validation work has been completed for its derived currents, and is documented by Mosterdijk and Miller (2008). This work is limited to the Port of Rotterdam, in the Netherlands, where an X-band SeaDarQ radar system was installed at a height of 70 metres to estimate currents at the harbour entrance. The analysis is limited to two days of data, but shows a very good agreement with the horizontal tide. As of this time, the SeaDarQ software has not been validated for its bathymetry estimates.

2.2.2 X-band Radar Applications

This section highlights a few instances of X-band radar performance in a variety of coastal environments, to better understanding its *possible* accuracy. Only water depth estimates are investigated given the relationship between d and $\vec{U}$, shown in Equation 2.3. In theory, the current vector can be determined if the water depth is correctly estimated.

Bell (1999)

The work presented in Bell (1999) investigates Holderness, on the east coast of England, where X-band radar was deployed in 1995. The output range is approximately 1.2 kilometres with an unknown antenna elevation. The results of this study are included in Figure 2.4. The instantaneous depth (i.e. single output time) on the output grid is presented in Figure 2.4a. The timestack from an extracted longshore profile within the output grid helps validate the technique given the tidal signal (Figure 2.4b). Bell (1999) concludes by recommending the inclusion of higher order wave theories to resolve shallow water depths.

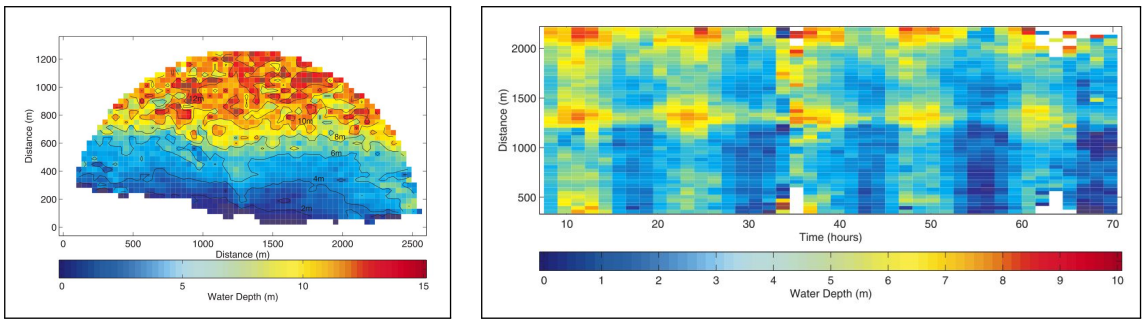

(a) Water Depth **(b)** Timestack of Extracted Longshore Profile

Figure 2.4: X-band Data at Holderness, U.K. (Bell, 1999)

Bell (2008)

Bell (2008) investigated the use of WaMoS II radar data in the Dee estuary in Liverpool Bay. The output range was 4.0 kilometres with an antenna height of 30 metres. The analysis used 3 output times during a single high tide (water level $\approx$ 10 m) to compare against recent LiDAR and multibeam measurements, see Figure 2.5. The radar output is shown in Figure 2.5a, with the combined measured surface in Figure 2.5b, and the differences in Figure 2.5c. Bell (2008) states that the radar bathymetry is accurate to $\pm$ 1 metre when waves are present, but shows poor agreement in the deep flood channel and at the extents of the radar output grid. This work proves the applicability of X-band radar in a stratified environment.

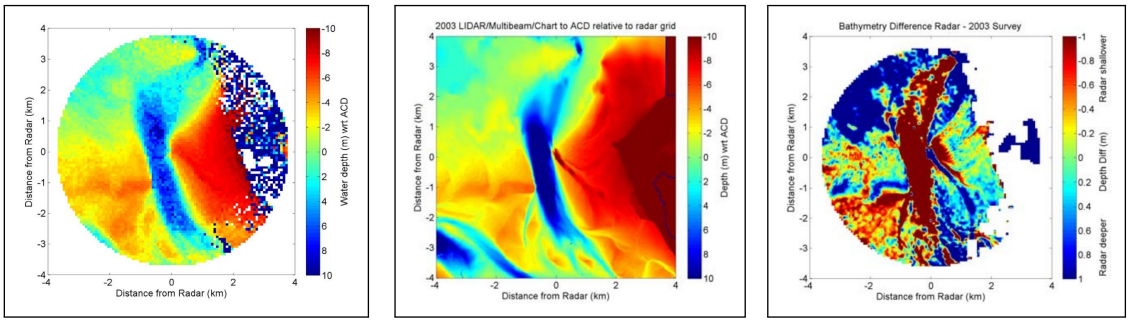

(a) Radar Depth **(b)** Measured Depth **(c)** Difference in Depth

Figure 2.5: X-band (WaMoS II) Data in Liverpool Bay, U.K. (Bell, 2008)

Senet et al. (2008)

Senet et al. (2008) use a WaMoS II unit deployed in the North Sea on the Island of Sylt, Germany to extract bathymetric features in the intertidal area. The usable output range is 1.2 kilometres with an antenna height of 40 metres. The analysis period is one tidal cycle during September 2001. The relevant results are included in Figure 2.6. It includes the absolute error of the depth estimates (Figure 2.6a), the difference between *in situ* measurements (Figure 2.6b) and the direct comparison between the two datasets (Figure 2.6c).

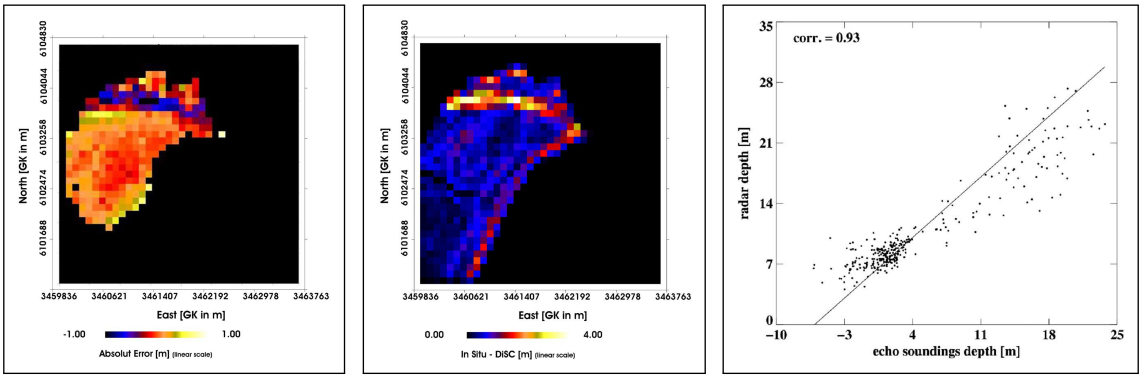

(a) Absolute Error **(b)** Difference in Depth **(c)** Direct Comparison

Figure 2.6: X-band (WaMoS II) Data at the Island of Sylt, Germany (Senet et al., 2008)

Hessner and Bell (2009)

Hessner and Bell (2009) use the same radar setup described in Senet et al. (2008). The analysis and its results (see Figure 2.7) are based on a single storm in March 2004, which lasted less than 24 hours. Note that the complex bathymetry in Figure 2.7b is generally represented quite well by the radar data (Figure 2.7a) but still results in errors of up to $\pm$ 2 metres (see Figure 2.7c). Lastly, this work proves the applicability of X-band radar in an intertidal environment.

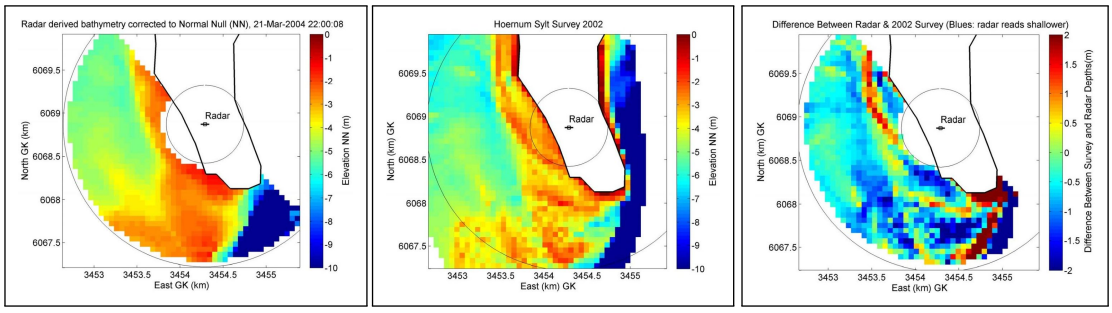

(a) Radar Depth **(b)** Measured Depth **(c)** Difference in Depth

Figure 2.7: X-band (WaMoS II) Data at the Island of Sylt, Germany (Hessner and Bell, 2009)

Flampouris et al. (2011)

This work investigates the implementation of three non-linear depth inversion algorithms (Hedges, Kirby and a modified Cnoidal) and compares their performance to linear theory with *in situ* bathymetric data (Flampouris et al., 2011). The radar was deployed on the Island of Sylt, as explained by Senet et al. (2008). The comparison was limited to a single storm of 12 hours, which was then averaged. The Kirby non-linear theory shows the best agreement over steep bathymetric features (reduced error in Figure 2.8a), but still includes as much variability as the linear theory (Figure 2.8b). Flampouris et al. (2011) concludes by stating the "*the signal processing algorithm* [...] *is more important than that of the inverted physical wave model*".

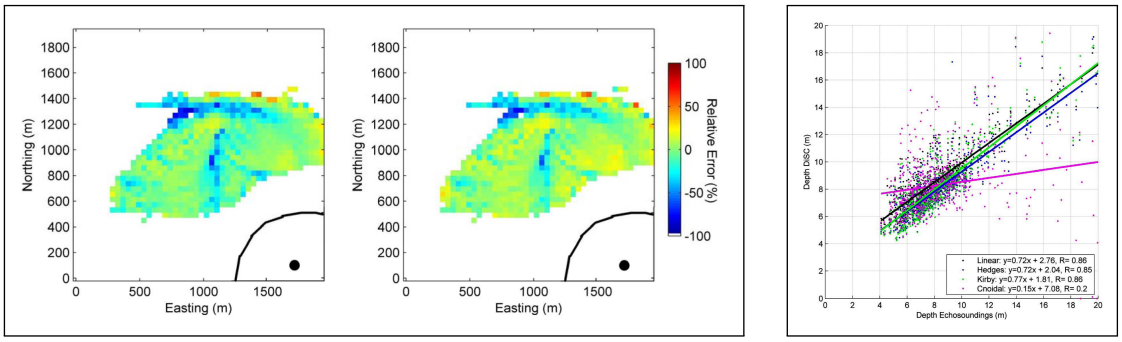

(a) Relative Error for Linear (left) and Kirby (right) Wave Theories **(b)** Direct Comparison

Figure 2.8: X-band (WaMoS II) Data at the Island of Sylt, Germany (Flampouris et al., 2011)

Deltares (2011)

The aim of Deltares (2011) was to gain more insight using SeaDarQ X-band radar in coastal engineering applications and as a validation source. The work was undertaken in the Ameland inlet, the Netherlands. The radar range was 7.5 kilometres and an antenna height of 55 metres. The mean bed level from a single storm lasting less than 24 hours is included in Figure 2.9. This research produced highly variable estimated bathymetry, with standard deviations ranging from 0.5 to 6 metres. Deltares (2011) concludes that this approach requires further research into optimizing the SeaDarQ output with potential filtering.

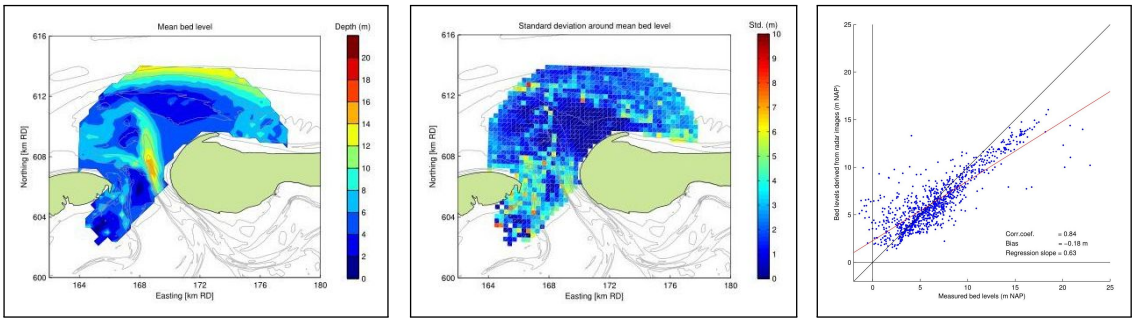

(a) Mean Bed Level **(b)** Standard Deviation **(c)** Direct Comparison

Figure 2.9: X-band (SeaDarQ) Data at the Ameland Inlet, the Netherlands (Deltares, 2011)

Chapter 3

Objective

The X-band radar results published by Bell (1999), Senet et al. (2008), etc... all show a good agreement with *in situ* measurements, but are limited to a short (even instantaneous) time period and use *ideal* hydrodynamic conditions. There is a great deal of uncertainty regarding the overall methodology and fully understanding the depth inversion procedure. The non-linear fitting of the linear dispersion equation (Equation 2.2) is rather straightforward, but its accuracy is a function of the selected *real* spectra data (i.e. minimum cutoff distinguishing signal from noise).

The previous algorithms explained in Chapter 2.2 are essentially closed since they are commercial products. Ideally, it is most suitable for research if a depth inversion model was fully open for testing. This allows for a much deeper investigation into all parameters and sensitivities influencing radar-derived estimates.

The objective of this research is to develop an X-band radar depth inversion model at the Sand Motor for further investigation into remote sensing as an accurate tool for estimating nearshore bathymetry and hydrodynamics.

The main goal of this thesis work is to investigate the applicability of radar-derived bathymetric and hydrodynamic estimates by further developing the Global Method (presented in Chapter 2.2) within the MATLAB® environment. The intended model should be able to accurately estimate hydrodynamic parameters from raw X-band radar images with high temporal and spatial resolution. It is of great use to better understand the inherit limitations of radar-derived estimates, in terms of how accuracy varies as a function of the coastal conditions. More knowledge regarding ideal conditions would help reduce the use of remote sensing when it will not produce accurate information.

The developed model should also be used as a research tool to better understand both the overall methodology and its potential viability for reliable remote sensing. The depth inversion algorithm is developed in the MATLAB® environment for the following reasons:

- Platform for Future Research and Development
  - Open tool designed for academic use, expandable through new subfunctions
- Simple to Comprehend, Modify and Debug
  - Fully commented, simple architecture, easy to understand
- Built-in Visualization
  - MATLAB® graphics engine, OpenEarth integration (Van Koningsveld et al., 2010)

Accurate results are determined based on *in situ* measurements. *In situ* water depth is constructed from a combination of data sources. Further insight into *ideal* X-band radar conditions are studied in Chapter 8 by incorporating nearby metocean data. The following sources are used in this analysis, and further elaborated in Chapter 4.

- Bathymetric Surveys
- Scheveningen Measured Water Level
- Hoek van Holland Measured Wind
- Wave Buoy near the Sand Motor
- ADCP near the Sand Motor

Lastly, all work presented in this thesis is **temporally limited** to a single storm event from October 21^{st} to November 1^{st}, 2013. This time period was selected given the availability of the necessary raw radar data.

Chapter 4

Datasets

This work requires two distinct datasets for comparison - the X-band radar data and the *in situ* measurements. The *in situ* data is necessary for judging the performance of the radar-derived estimates and to establish a relationship with radar quality. The *in situ* water depth is created by combining quasi-monthly bathymetric surveys with measured water levels, while currents are directly measured using a deployed **A**coustic **D**oppler **C**urrent **P**rofiler (ADCP).

To better visualize the location of each dataset used in this work, an overview map of the Sand Motor project site for the temporal period in question (October 21^{st} to November 1^{st}, 2013) is included below in Figure 4.1.

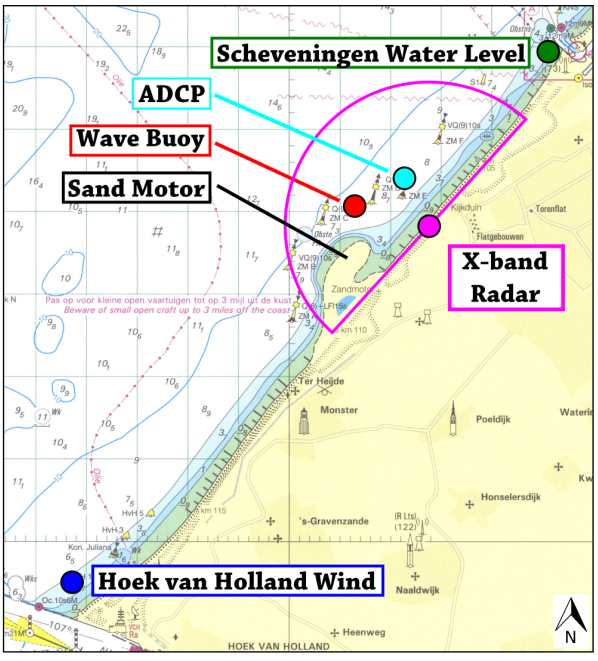

Figure 4.1: Overview Map

4.1 X-band Radar

The X-band radar unit deployed at the Sand Motor has been operational since June 2012. It is equipped with the SeaDarQ software; refer back to Chapter 2.2. The physical radar setup at the Sand Motor is depicted in Figure 4.2a, which shows the relatively low antenna height of 15 m. The output range of the radar is constant at approximately 4 kilometres. Additional information about the radar deployment at the Sand Motor is contained within Deltares and Imares (2012).

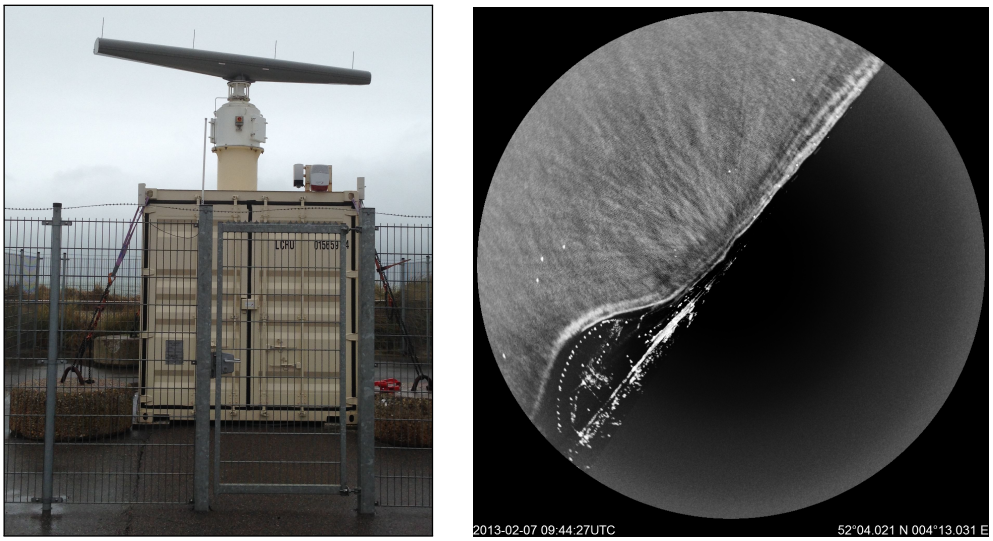

(a) Radar Installation **(b)** Raw Radar Image

Figure 4.2: Deployed X-Band Radar at the Sand Motor

The single input for the SeaDarQ algorithm are raw radar images; see Figure 4.2b. These files are saved in a proprietary SeaDarQ format (*.drq), but are typically not stored given their large size (e.g. 2 hours ≈ 16 GB). SeaDarQ processes the raw data after each timestack into much smaller text files containing the resulting hydrodynamic parameters. Thus, there are two types of data *formats* available for the *same* storm event - raw radar images and processed SeaDarQ results. Although this data is in fact from the same source, it allows the flexibility to analyze the radar images in a completely different manner than that found within the SeaDarQ algorithm. The processed SeaDarQ radar estimates are only used as a benchmark for the newly developed X-band radar depth inversion model.

4.2 *In situ* Data

The *in situ* data must align spatially and temporally to compare against the X-band radar dataset. For this reason, all spatial data is *adaptively* interpolated to the chosen radar grid using a natural neighbour approach. This method allows for variable spatial settings, which may or may not be identical to the SeaDarQ output grid. Temporal data is also *adaptively* interpolated in time to the analyzed radar timestep, since it can vary based on the analyzed

timestacks. This allows for full freedom in picking non-uniform spatial and temporal settings. The following *in situ* datasets at the Sand Motor are used throughout this thesis work.

4.2.1 Bathymetry

Monthly jet ski bathymetric surveys are being completed at the Sand Motor to capture the evolution of the nourishment since its inception in August 2011. Background information regarding the monitoring campaign can be found in Deltares and Imares (2012). Additional survey data from Vaklodingen, Jarkus and NeMo are used to fill the entire radar domain.

The raw data is converted to the radar grid by interpolating a created bathymetric *surface* in MATLAB®. The initial data from various sources is presented in Figure 4.3a, with the interpolated bathymetry in Figure 4.3b. All work in this thesis is spatially limited to the 4 kilometre range of the radar at the Sand Motor.

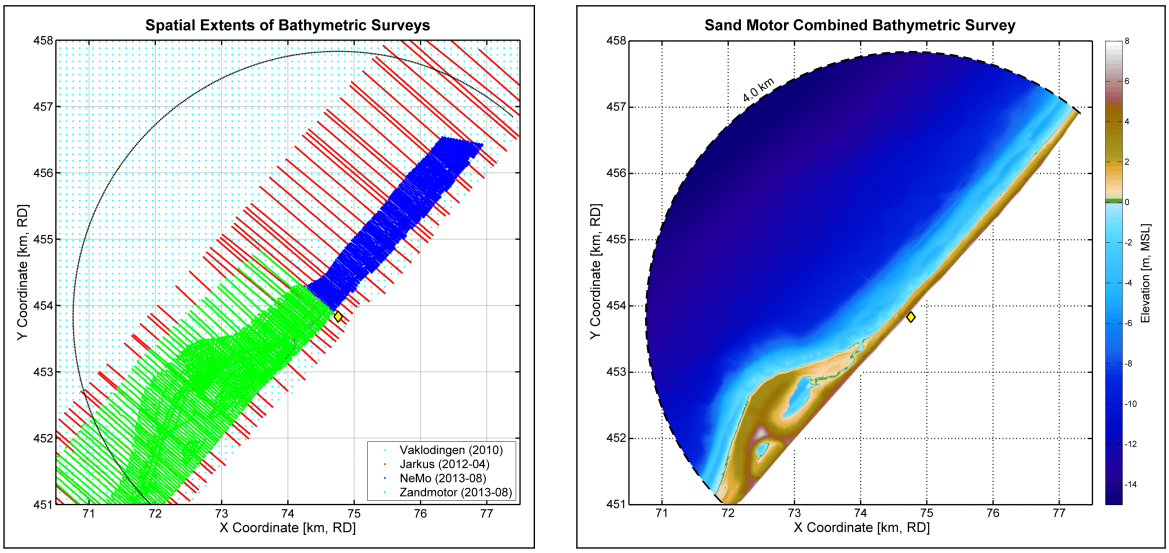

(a) Bathymetry Sources **(b)** Interpolated Bathymetry

Figure 4.3: Combining Bathymetric Surveys at the Sand Motor

4.2.2 Water Levels and Currents

The previous section provides an instantaneous bathymetric surface at the Sand Motor relative to the local datum (*Normal Amsterdams Peil*, NAP), but without the temporally varying water level. The interpolated bathymetric surveys require the addition of continuous water levels in order to create a spatial time series of water depth. This is completed by including the nearby Scheveningen water level gauge data; see the top panel in Figure 4.4. The water level data was downloaded from the MATROOS tool (Rijkwaterstraat, 2014).

The deployed ADCP provides measured currents at fixed bins from the bed, but only the near-surface bin is used for comparison in this work. There is little knowledge regarding where radar-derived currents are located, but are assumed to be near-surface given their interaction

with surface waves (Young et al., 1985). See Deltares and Imares (2012) for more information regarding the fieldwork, while the measurements are summarized in Figure 4.4.

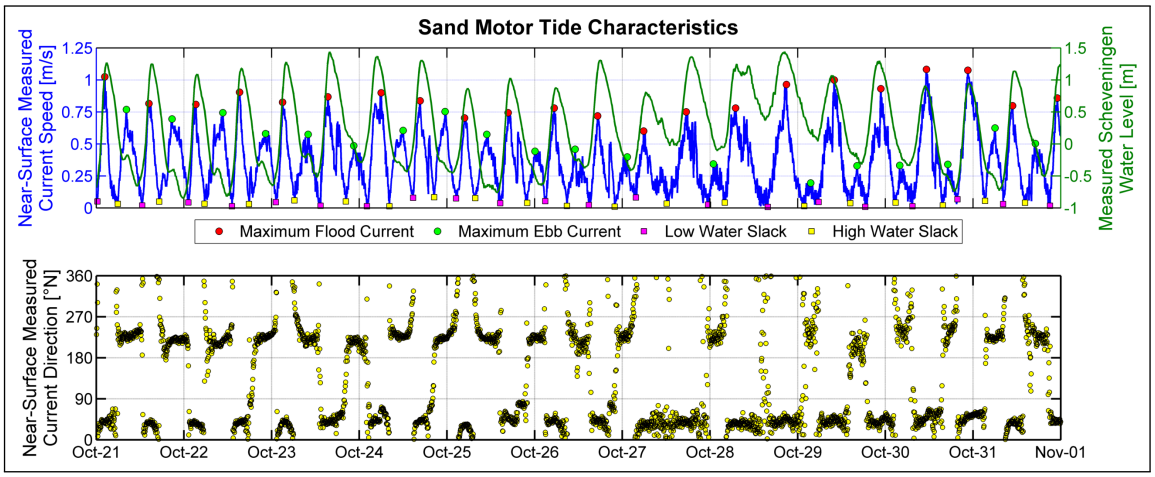

Figure 4.4: Tide Characteristics at the Sand Motor

4.2.3 Wind and Wave Data

Metocean conditions are necessary when relating radar quality and the surrounding hydrodynamic conditions (later in Chapter 8). Wind data was downloaded from the nearby Hoek van Holland anemometer, with a temporal resolution of 10 minutes (Rijkwaterstraat, 2014). Wave information was extracted from the active wave buoy at the Sand Motor. More details regarding the fieldwork campaign is detailed in Deltares and Imares (2012).

Figure 4.5 contains the entire metocean climate used in this work. The top panel contains the wind speed, the middle panel shows the significant wave height and the peak period, while the bottom panel shows the peak wave direction and the recorded wind direction.

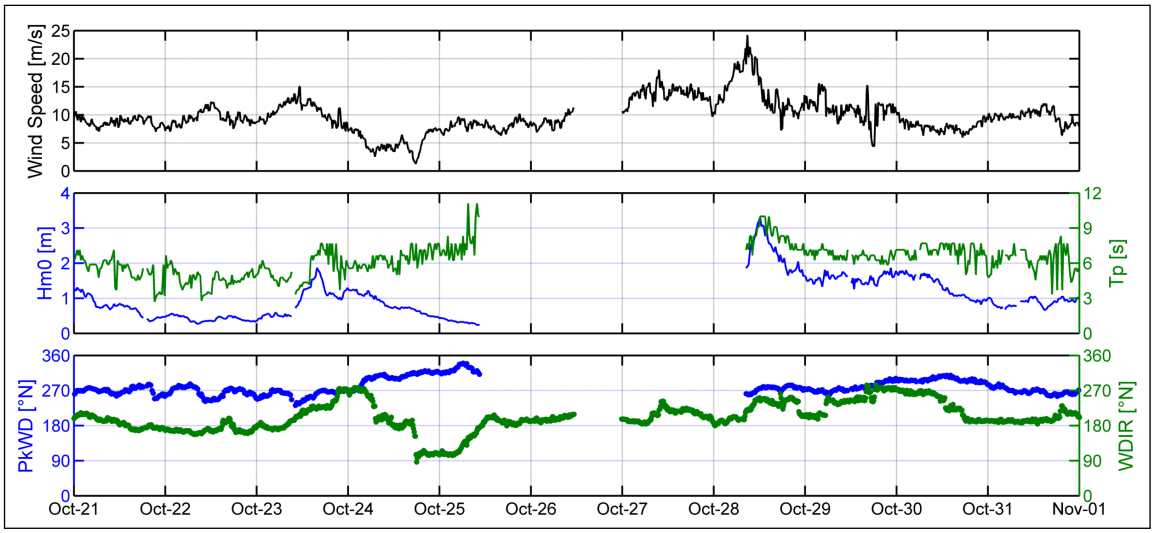

Figure 4.5: Metocean Data Near the Sand Motor

Chapter 5

XMFit Development

This section explains in detail the overview, usage and the internal algorithm developed during this thesis work. As explained in Chapter 3, it is of value to build an open tool to properly research X-band radar depth inversion capabilities. The Global Method presented in Chapter 2.2 was improved upon through development of the **X**-band **M**ATLAB® **Fit**ting Method (herein referred to as **XM**Fit). A conceptual work flow diagram is presented in Figure 5.1.

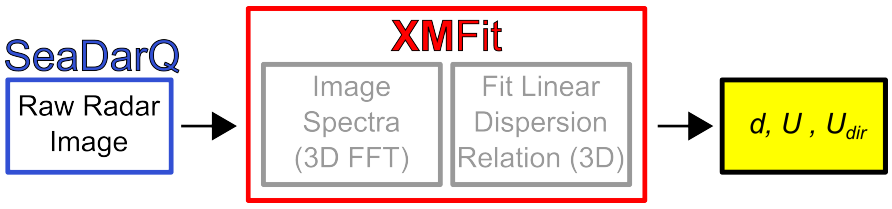

Figure 5.1: XM Fit Concept

The overall concept is to take raw radar images from the SeaDarQ interface, freely select spatial settings, manually extract the image spectra and have full control when fitting the linear dispersion shell. The conceptual approach within **XM**Fit is founded on two main components.

- **Image Spectra**
  - Transform image stack into image spectra
- **Fit Linear Dispersion Relation**
  - Distinguish spectra data from noise and fit to linear wave theory

In short, this method allows the estimation of hydrodynamics at any location within the radar range with any spatial settings. Note that the SeaDarQ software is used since the raw radar data is stored in their proprietary file format (*.drq).

Lastly, it should be mentioned that the entire procedure is essentially transparent. The entire code, its architecture and its layout were developed in full for this thesis. There are no unknowns within the analysis since its results are not based on a closed commercial product. Thus, the **XM**Fit algorithm provides full confidence in the input data, the internal algorithm and its output estimates.

5.1 XMFit Global Procedure

This section explains the major components of the **XM**Fit algorithm from a global perspective. It explains the entire procedure within **XM**Fit from input to output. A more detailed work flow that best represents **XM**Fit is visualized in Figure 5.2.

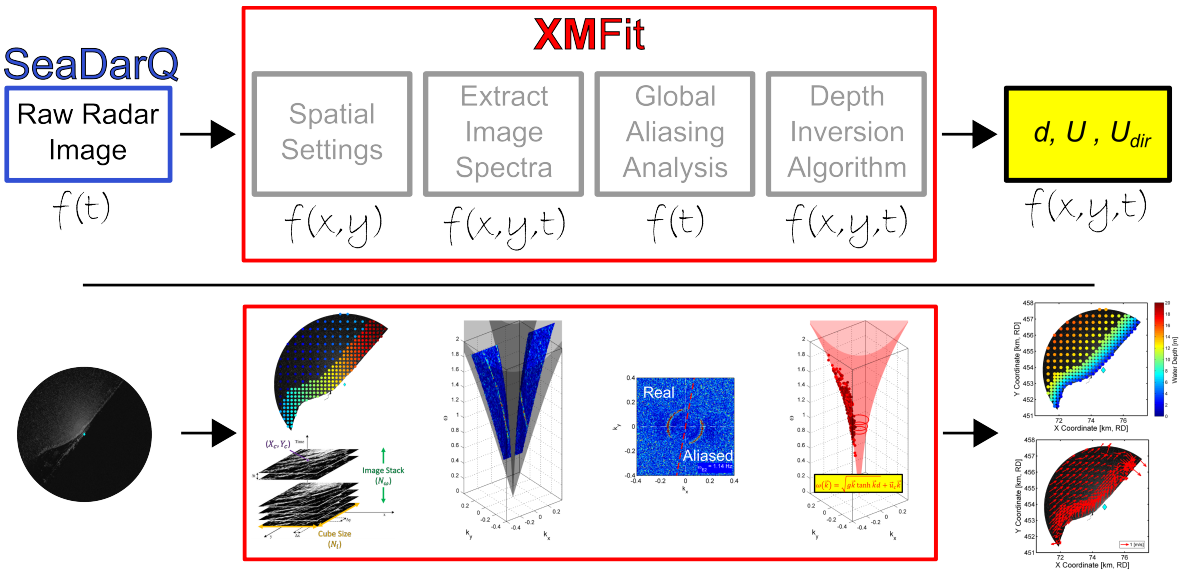

Figure 5.2: **XM**Fit Visual Work Flow

A basic visual depiction of the **XM**Fit work flow is presented in the bottom panel of Figure 5.2, which is included to help reinforce the depth inversion procedure. Each component within **XM**Fit is explained in its own section in this chapter. The necessary inputs and potential outputs of the **XM**Fit model are first presented in order to appreciate its capabilities.

5.1.1 Usage

XMFit is an extremely simple model to use. It is run in MATLAB® since it was built, tested, validated and calibrated within this environment. The model was developed using a large number of subfunctions, which help to debug potential issues and better understand how the various pieces of code work together. **XM**Fit is heavily commented with clear instructions regarding inputs. **XM**Fit also provides parallel support (if necessary) by using the Parallel Computing Toolbox. Note that this feature is not always suitable given the overhead with respect to virtual memory since it requires copying data to each *additional* instance of MATLAB®.

XMFit is run with very few inputs with the possibility of many outputs. The desired outputs can drastically reduce performance and increase run time. It should be mentioned the large storage requirement if the user opts to save spectra information by gridpoint. A list of the **XM**Fit inputs and outputs are included below. The blue text indicates optional settings and their respective outputs.

Inputs

- **Environment Settings**
  - Radar Settings
  - Land Mask
- **Analysis Settings**
  - Input Timestacks
  - Δ_{grid}, N_i and N_ω
- **Solver Settings**
  - Non-Linear Fitting Method
  - Bounds for Fitting d and $\vec{U}$
- **Output Settings**
  - Standard **XM**Fit Figures
  - Non-Linear Fitting Method
  - Depth Inversion Procedure

Outputs

- **Data** (by timestep)
  - $d, \vec{U}$
  - $T_{pk}, PkWD, L_{pk}$
  - $d_{95\%}, R^2, RMSE$
- **Figures** (by timestep)
  - **XM**Fit Results
  - *In situ* Comparison
  - Extracted Profile
  - Aliasing Procedure
  - Depth Inversion Procedure
  - Non-Linear Fitting Method
- **Animation** (by day)
  - Google Earth (OpenEarth)

5.2 XMFit Internal Algorithm

This section of the report explains the four core *building blocks* represented within the **XM**Fit algorithm in Figure 5.2. Prior to explaining the spatial settings, it is important to realize its main input is a radar timestack. This is by definition a certain number, N_ω, of raw radar images.

5.2.1 Spatial Settings

The spatial settings are necessary to transform the raw radar timestack into an individual *computational cube*. This is done by first discretizing the radar spatial grid into a set of user-defined gridpoints. The nearshore-refined grid in Figure 5.3 was constructed to strike a balance between detail and computational efficiency. All **XM**Fit model output was completed using this refined grid. Note that grid settings do not influence accuracy. The grid only defines the spatial resolution for the resulting estimates.

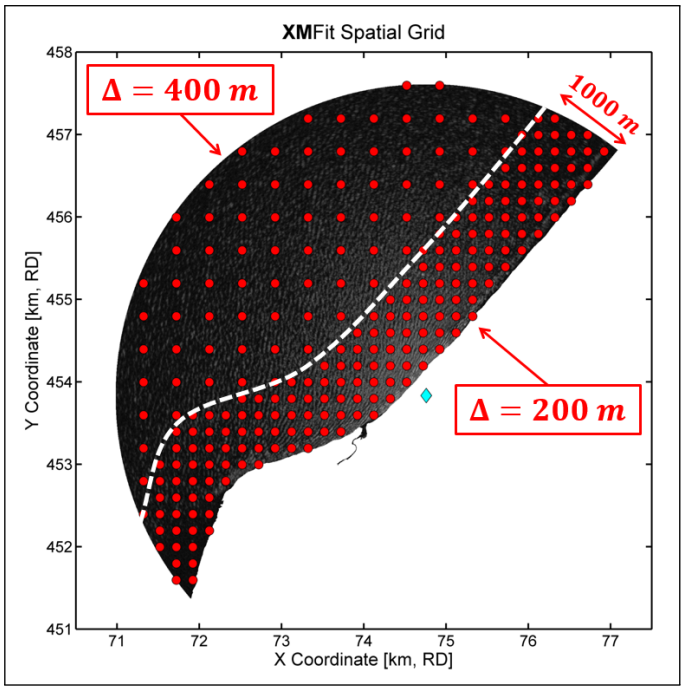

Figure 5.3: Refined **XM**Fit Spatial Grid

A computational cube is specific to each gridpoint. Its planar footprint is defined as a certain number of pixels, which this work refers to as N_i. The cube is also confined by the maximum number of images in the timestack (N_ω). Each computational cube has the dimensions N_i x N_i x N_ω. A visualization was previously presented in Figure 2.2.

Table 5.1 provides typical spatial settings (and their respective physical values) applicable at the Sand Motor. Various different settings were tested, but only those listed below exhibited any agreement with ground truth measurements. Smaller cube sizes give inaccurate results since they do not provide enough data for the processing algorithm. Larger cube sizes result in the highest resolution data, but their physical extents is much too large for any realistic application.

Table 5.1: Selected Spatial Settings for **XM**Fit at the Sand Motor

N_i		N_ω	
Pixels [-]	Length [m]	Images [-]	Time [s]
64	240	32	90
128	480	64	180
256	960	128	360

Lastly, a separate analysis was completed to identify any relation between computational cube size and its location within the radar domain. The final results from the spatial calibration are presented in Figure 5.4. A full explanation of the calibration is contained in Appendix A.

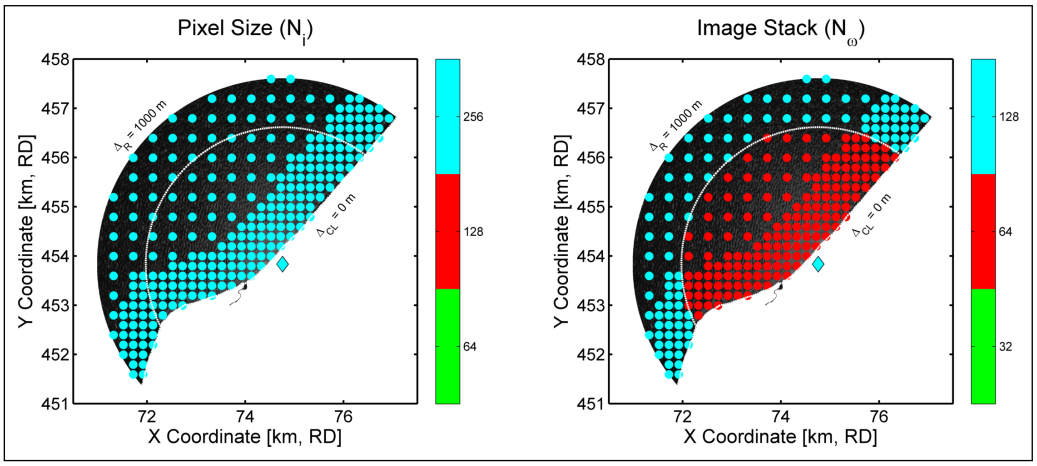

Figure 5.4: Spatially-Varying Computational Cube Sizes

5.2.2 Extracting Image Spectra

The computational cube is then transformed through use of a 3D Fast Fourier Transform (FFT) to the frequency domain. This is completed to resolve the visible propagating wave components. The main goal is to extract the image spectra by

$$[Spectra_{x,y,t}] = \psi(I_{stack}, XY_c, N_i, N_\omega) \tag{5.1}$$

where I_{stack} is the raw radar input timestack, XY_c is the user-defined spatial grid, and N_i and N_ω are from the spatial calibration in Appendix A. The image spectra extraction is best represented by Figure 5.5, which shows the combination of various images in time for a specific computational cube and its resulting spectra information in k_x, k_y, ω space.

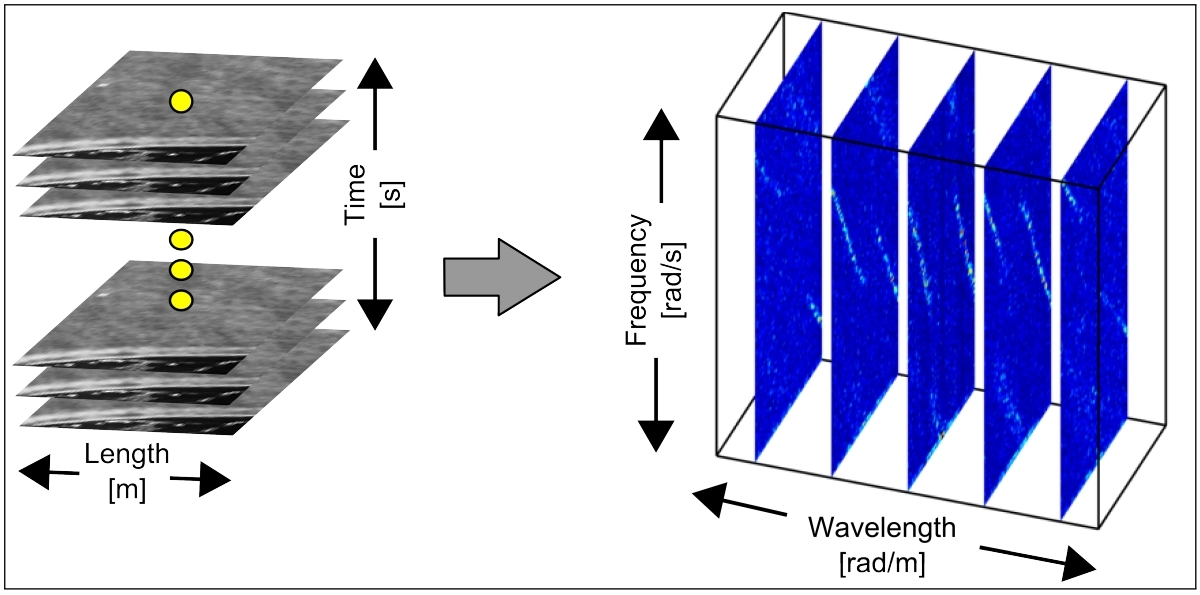

Figure 5.5: Image Spectra Extraction from Computational Cube

There are two distinct signals in the frequency domain after extracting the image spectra due to aliasing effects. This phenomenon is further elaborated in the next section.

5.2.3 Global Aliasing Analysis

The two distinct signals represent the same information but one is *aliased* to a different frequency level. This is caused by the slow turning antenna ($\Delta t \approx 2.85$ s). The images are discretized in time based on this rotation speed. The FFT analysis is not able to distinguish between harmonic waves that match the sampling interval. This results in a shifting of spectra information based on the Nyquist frequency, $f_N = 1/2\Delta t$ (Holthuijsen, 2007). The Nyquist frequency is quite close to the wave climate (see Figure 4.5), which consistently introduces aliased energy. This signal must be removed in order to fit the linear dispersion shell since it has no physical meaning. It is simply an artifact from the instrument sampling interval. Further work into identifying the aliased signal is explained by Serafino et al. (2011).

The aliasing analysis detailed in this section is performed once per timestep. It is solely a function of time and not of space. This assumes that the wave climate is relatively stationary with respect to spreading within the radar domain for a single timestep. Spectra energy (both real and aliased) is most evident and most defined when the computational cube is increased. Therefore, this analysis uses a large cube ($N_i = 512$) in the middle of the radar domain where it is not influenced by land or edge effects. Figure 5.6 visually represents the analysis and the end result - a *directional cutoff filter* to distinguish between real and aliased spectra energy.

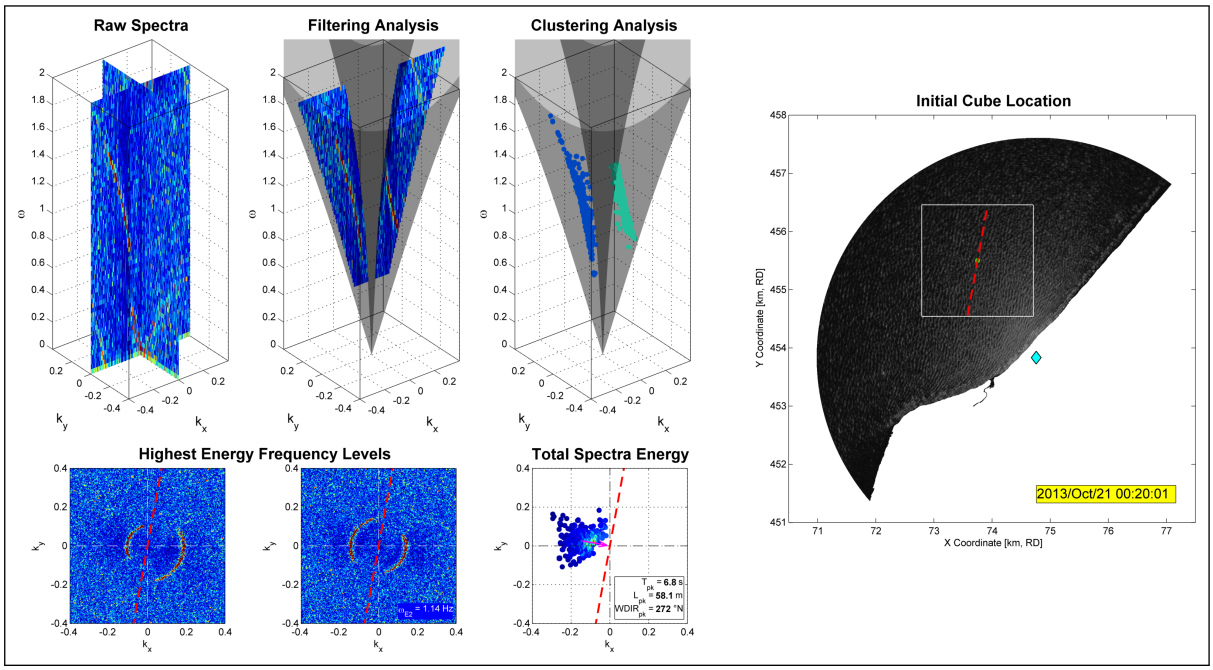

Figure 5.6: **XM**Fit Global Aliasing Analysis

The analysis begins with the raw image spectra extracted from Chapter 5.2.2. This data is visualized in the **Raw Spectra** plot. The **Filtering Analysis** is explained in Section 5.2.4 since the same approach is used. The most important aspect of this analysis is dividing

between the two signals, while only keeping the real data. The **Clustering Analysis** determines the real signal by implementing a k-means clustering algorithm. More information is provided in the next section. The real data in Figure 5.6 is represented by the blue series of points in the **Clustering Analysis**. This scatter data is then integrated with respect to frequency to identify the wave properties (i.e. wave direction, wavelength). Lastly, an *orthogonal directional cutoff* is defined based on the mean wave direction, which is saved for the analyzed timestack and applied at each gridpoint.

Clustering Analysis

This section investigates in more detail the **Clustering Analysis** referenced during the Global Aliasing Analysis. Clustering involves the use of a k-means algorithm, which segregates the data using various metrics (i.e. Euclidean distance, correlation, cosine, etc...) (MATLAB, 2013). This process requires the filtered spectra data as input but requires the removal of the noisy signal. A minimum energy cutoff is defined based on the normalized spectra energy values. Thus, the k-means algorithm is completed iteratively with various amounts of data based on the cutoff value, see Figure 5.7. Note that the optimum energy cutoff is addressed in Chapter 5.2.4.

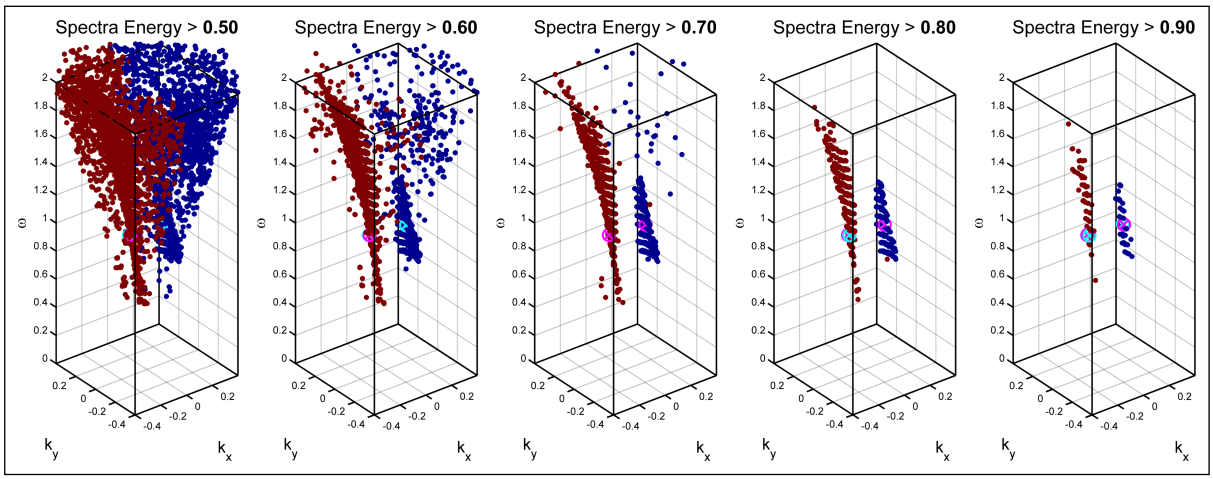

Figure 5.7: XM Fit Clustering Analysis

Various cutoff values are used to better represent the two subsets within the data. A high minimum energy cutoff provides more confidence in clustering but removes far too much spectra data. On the other hand, a low minimum cutoff keeps most of the information but is typically too scattered and causes clustering issues. A balance is found by using all cutoffs to determine real spectra energy. For the example presented in Figure 5.7, the real data is the red series and the aliased data is the blue series. This is concluded through many steps but essentially looks at the relationship between fitting the intrinsic dispersion shell at each frequency level and its correlation with frequency. Figure 2.3 visualizes this relation, indicating how the intrinsic shell *widens* as a function of k_x, k_y as ω increases. Basically, the real spectra data will exhibit a positive correlation between frequency and the resulting intrinsic shell. The aliased energy will show the opposite trend.

5.2.4 Depth Inversion

XMFit has thus far described the selection of computational cubes, the extraction of wave components via the 3D FFT, and the issues with aliasing evident in the resulting signal due to the Nyquist frequency. This gives the necessary background to perform the most important step - the depth inversion. This section explains the depth inversion procedure at a single computational cube for a given timestack. The main goal is to extract the radar-derived hydrodynamics by

$$[d, \vec{U}] = \psi(Spectra_{x,y,t}) \tag{5.2}$$

where $Spectra_{x,y,t}$ is the extracted image stack, while d and $\vec{U}$ are the desired depth and current estimates that correspond to the best fitting linear dispersion shell. Figure 5.8 visually describes the steps in the depth inversion procedure. The goal is to use the wave information in the **Raw Spectra** plot to fit the linear dispersion shell in the **Depth Inversion** plot. The resulting hydrodynamic estimates from the best fitting shell are shown in the yellow textbox (bottom right hand corner). An explanation of each step (based on the label of each subplot) is presented below given the complicated figure describing the non-trivial algorithm.

- **Raw Spectra**
  - Raw output from the extracting the raw image spectra (Chapter 5.2.2)
- **Filtering Analysis**
  - Remove unnecessary data not suitable for depth inversion based on physical limits. Frequency filtering limits the spectra data based on the metocean climate (i.e. T_{low} and T_{upper}), while wide dispersion filtering limits the k_x, k_y data by defining a $\omega_{low}(d_{low}, \vec{U}_{low})$ and a $\omega_{upper}(d_{upper}, \vec{U}_{upper})$
- **Aliasing Analysis**
  - Define real energy based on the *orthogonal directional cutoff* (Chapter 5.2.3)
- **Depth Inversion**
  - Non-linear fitting of the 3D doppler-shifted linear dispersion relation (see next section)
- **Highest Energy Frequency Levels**
  - Visual of the fitted shell based on the top energy levels based on frequency, ω. The top frequency level provides the estimate for the peak period, T_p.
- **Total Spectra Energy**
  - The wave direction and the wavelength are solved by integrating the selected real spectra data (from the non-linear fitting) with respect to frequency and finding the maximum energy. The peak in the kx, ky domain gives the resulting wavelength and peak wave direction.
- **Cube Location**
  - Spatial representation of the extracted computational cube, its corresponding current vector estimate, with fitting information provided in the adjacent textbox.

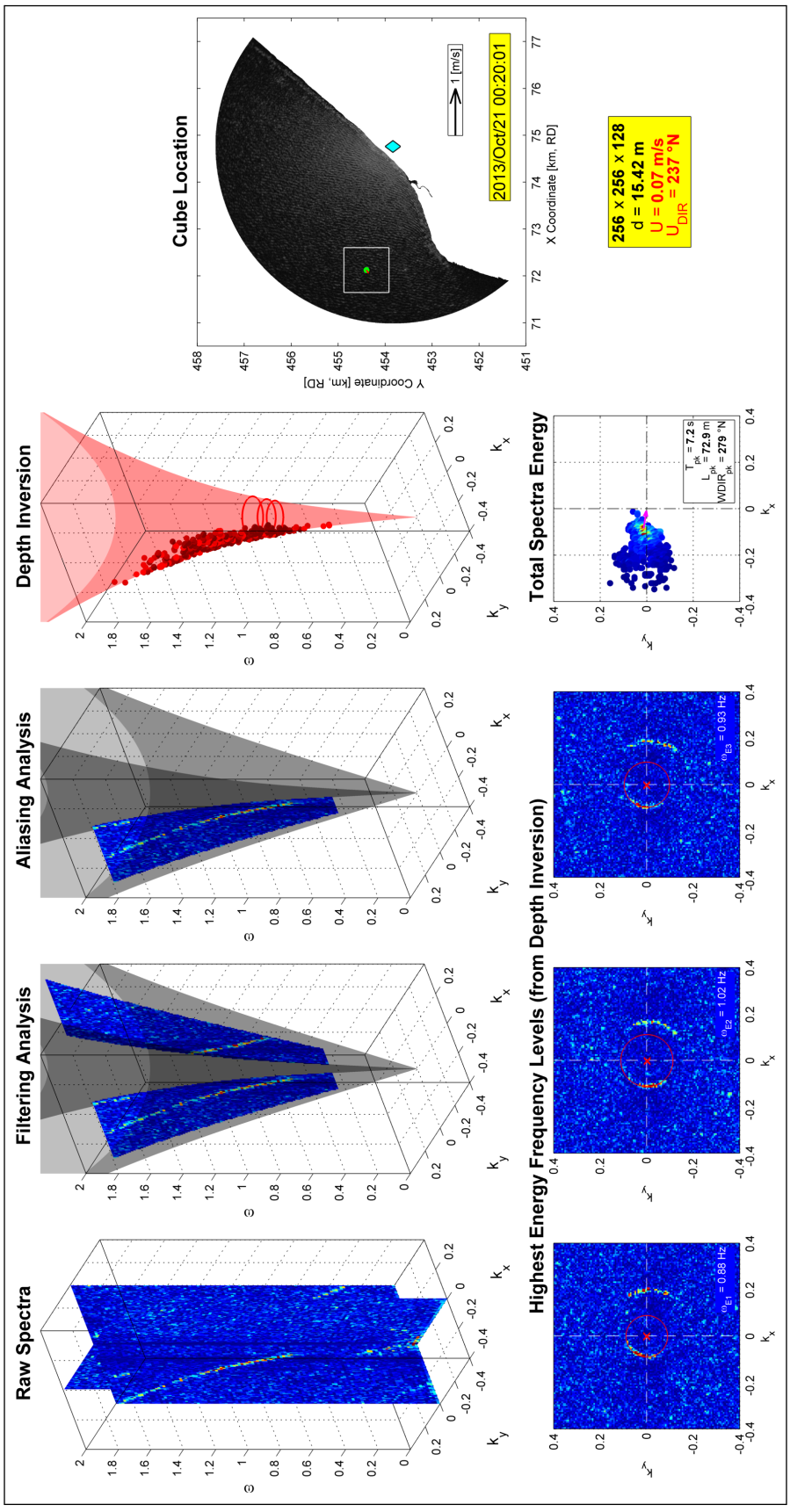

Figure 5.8: XM Fit Depth Inversion

Non-Linear Fitting

XMFit estimates d and $\vec{U}$ from the doppler-shifted linear dispersion relation (Equation 2.3) with the option of two solvers. The Levenberg-Marquardt non-linear regression (`nlinfit.m`) and the Trust-Region-Reflective optimization (`lsqnonlin.m`) are included in the model (MATLAB, 2013). Note that the `lsqnonlin.m` function allows the input of a Jacobian function, which is implemented in **XM**Fit to accurately find the global minimum of the doppler-shifted linear dispersion relation. The difference between the two solvers is practically negligible (see the validation in Chapter 6). The non-linear fitting is bounded by user-defined maximum and minimum depth and current estimates. The Sand Motor work herein estimates depth between 1.5 and 30 m and current speeds up to 1.5 m/s.

The actual non-linear fitting is quite basic, but its accuracy is dictated by the selection of input data. This directly corresponds to the minimum energy cutoff, which defines the indices where $E(k_x, k_y, \omega) > E_{min}$. All minimum energy cutoffs are analyzed given the uncertainty as to which cutoff is most suitable. Each iteration involves fitting the newly defined indices (function of minimum energy cutoff) to the doppler-shifted dispersion shell. This results in multiple estimates of d and $\vec{U}$ based on the shape of the best-fitting 3D dispersion shell. Table 5.2 shows the various solutions based on the minimum energy cutoff for the same computational cube presented in Figure 5.8. The selected hydrodynamic estimate is highlighted in red.

Table 5.2: Multiple Estimates from the Depth Inversion Algorithm

Min. Energy [-]	d [m]	U [m/s]	U_{dir} [°N]
0.50	14.29	0.24	318
0.60	14.71	0.11	311
0.70	15.42	0.07	237
0.80	15.54	0.17	203
0.90	17.23	0.25	255

The non-linear fitting is extremely sensitive to the amount of data used for fitting the shell, as made clear by Table 5.2. There is a fine balance between too much and too little data, but it is nearly impossible to quantify the perfect balance. For this reason, **XM**Fit currently selects the most ideal hydrodynamic estimates based on the lowest root mean squared error (RMSE) between the fitted dispersion shell and the selected k_x, k_y, ω spectra data. Thus, it adaptively selects the minimum energy cutoff.

Further work into testing higher-order non-linear wave physics in the depth inversion procedure is contained in Appendix B. This work is not contained in the main report since its results did not improve the accuracy of **XM**Fit.

Chapter 6

Theory Validation

It is crucial to ensure the procedure developed in **XM**Fit (which stems from literature) is able to extract realistic hydrodynamic results. The work presented in this section validates the depth inversion of X-band radar images at the Sand Motor.

6.1 Procedure

The validation procedure looks at comparing **XM**Fit estimates against *in situ* data. Luckily the ADCP measurements coincide with the bathymetric surveys - thus giving both known depth and currents at a single location. This gives information regarding the known *in situ* linear dispersion shell at the ADCP location.

The near-surface current was extracted at various times to ensure **XM**Fit could simulate the propagation of the tide along the Dutch coast. The maximum flood current, the maximum ebb currents, high water slack and low water slack times were extracted from the horizontal tide (refer back to Figure 4.4).

XMFit was run at the ADCP location for different tide times for the entire storm period with various fitting methods. Five different fitting methods were incorporated into **XM**Fit.

- **Non-Linear Regression**
  - Levenberg-Marquardt non-linear regression (`nlinfit.m`)
- **Global Optimization**
  - Trust-Region-Reflective optimization (`lsqnonlin.m`)
- **Intrinsic**
  - without the influence of the doppler-shifted currents (`nlinfit.m`)

- **Assimilated-Current**
  - with the known *in situ* current vector (`nlinfit.m`)
- **Assimilated-Depth**
  - with the known *in situ* water depth (`nlinfit.m`)

The five different fitting methods provided the possibility to test various sensitivities. Firstly, the non-linear solver (i.e. `nlinfit.m` vs. `lsqnonlin.m`) would indicate its influence on accuracy. Note that the Global Optimization method also includes the Jacobian of the doppler-shifted linear dispersion relation, which should improve the likelihood of finding the global optimum. The Intrinsic method is included to verify the fitting method during slack tide. The lack of currents results in a relatively *easy* solution since it consists of a single unknown. The last two methods highlight the validation of X-band depth inversion since it includes either the known depth or the known current. The ideal result is a perfect match between the Assimilated-Current and Assimilated-Depth methods. This would prove that known depth gives accurate currents and known currents gives accurate depth.

6.2 Single Tide Output

A single tide is included in this section in order to visualize its influence on fitting at various stages during a tidal cycle. The slack tide consists of both high water slack and low water slack, while the maximum horizontal tide includes the maximum flood and ebb current.

Slack Tide

Figure 6.1 and Figure 6.2 present the validation output for two slack water times. All figures in this section are quite busy, requiring the following explanation.

This work focuses on accurately fitting the peak spectra energy from the image spectra. Therefore, the top four frequency levels that coincide with the maximum spectra energy are visualized from left to right. Each row represents the fitting results by method (Non-Linear Regression, Global Optimization and Assimilated). This is visualized by superimposing the extracted frequency levels from the best fitting shell (by method) over the raw image spectra. This aids in determining how well each method is fitting the real spectra data and indicates the sensitivity of the non-linear fitting method.

The Intrinsic fitting method is included in the top two panels, while both Assimilated-Depth and Assimilated-Currents are combined in the bottom panel. The right hand side of the figure includes the computational cube with the estimates current vectors by method (indicated by colour of the fitting shell). Lastly, the measured tide is included for reference.

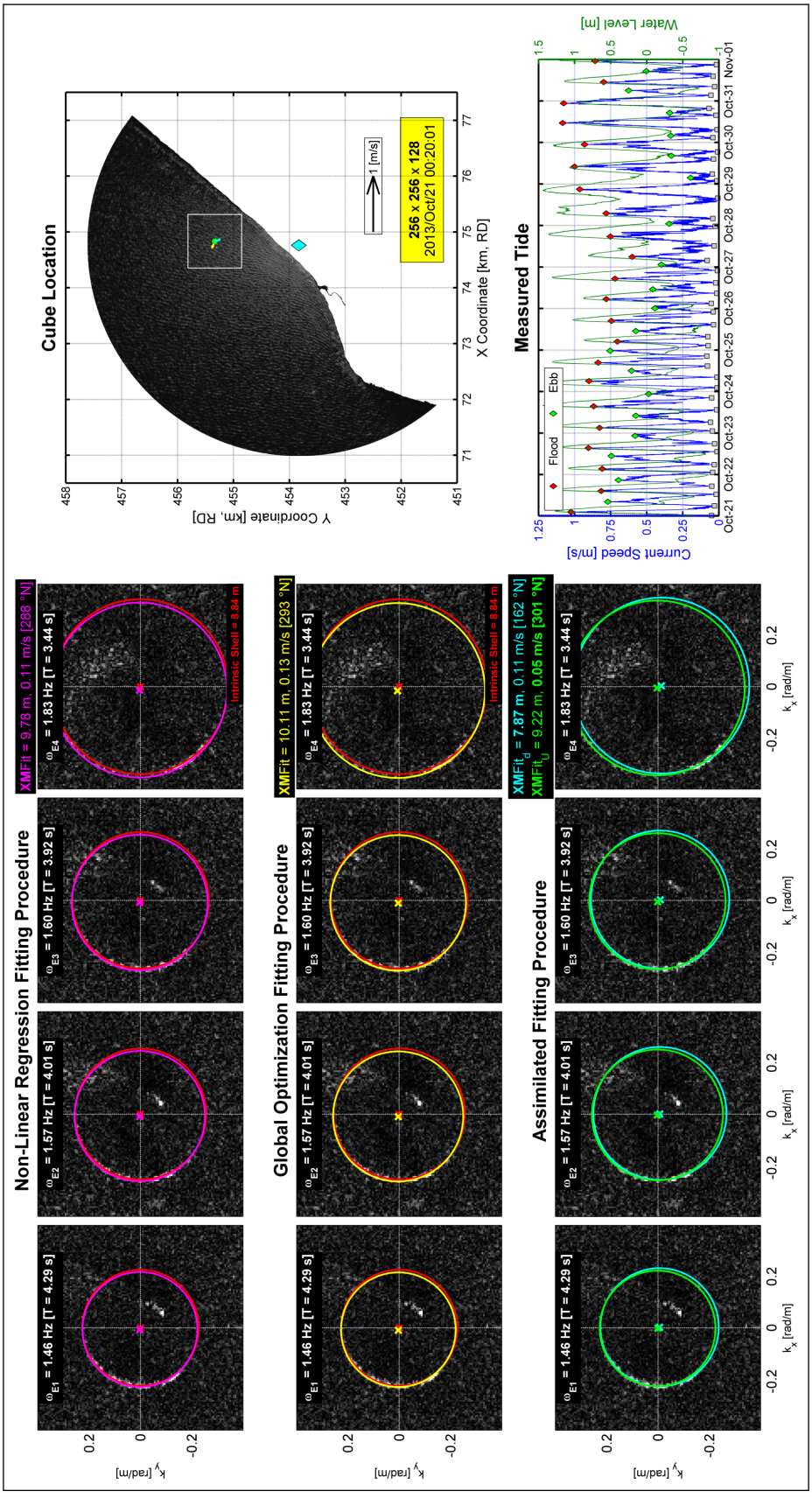

Figure 6.1: XMFit Validation at Low Water Slack

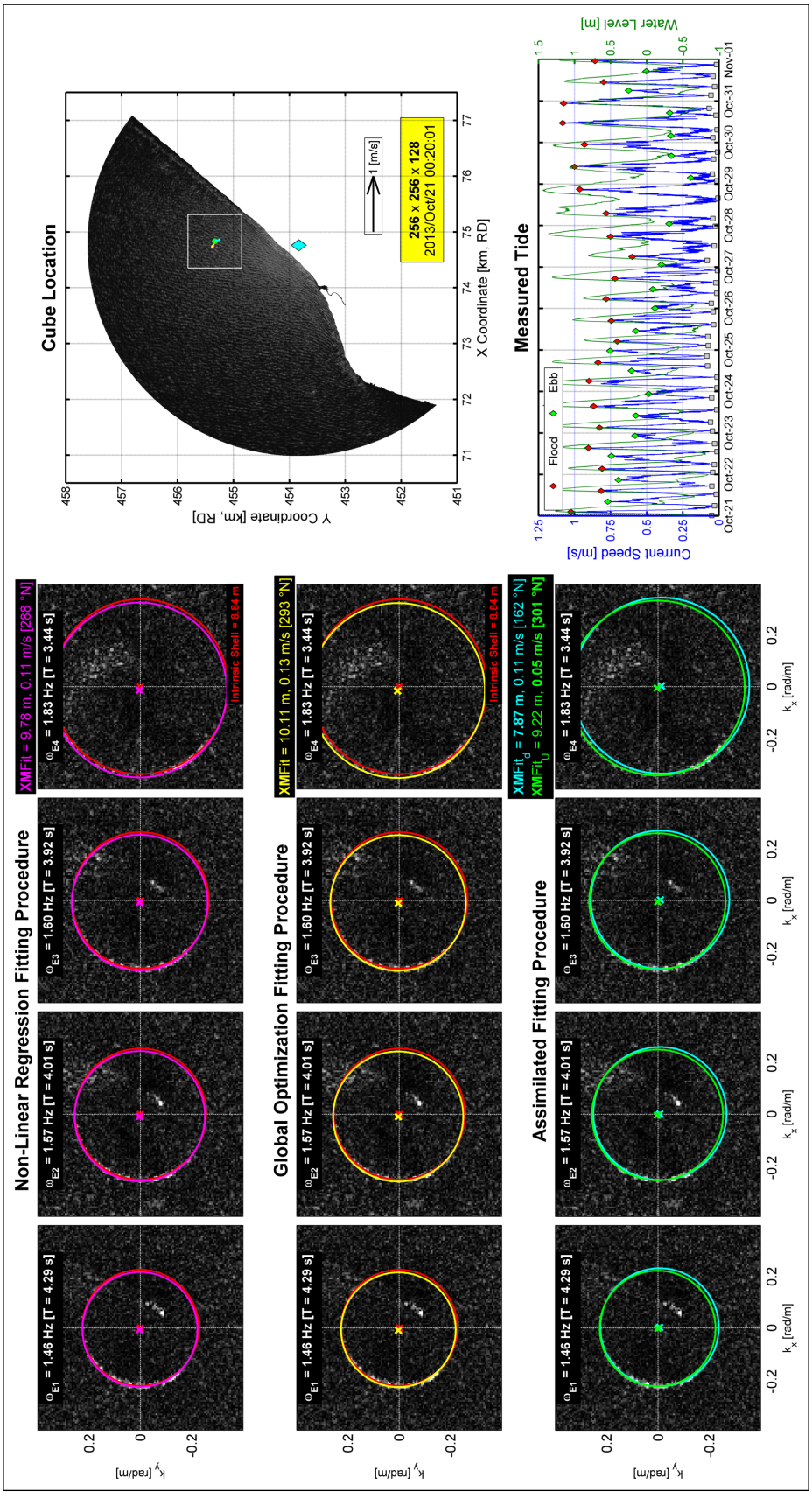

Figure 6.2: XMFit Validation at High Water Slack

Both of the slack tide validations show the same finding - **XM**Fit is visually fitting the spectra energy extremely well. Note that the other higher energy spectra not being fit is the aliased energy (refer back to Chapter 5.2.3). Several aspects of the validation require further attention.

The assimilated depth and current fitting methods align quite closely together but are not perfect. This indicates the potential uncertainty in X-band radar derived hydrodynamics since the simultaneous fitting of depth and currents is quite difficult.

As expected, the intrinsic shell matches the *in situ* water depth measurements much closer than the Non-Linear Regression and Global Optimation fitting methods. The comparison between the intrinsic and doppler-shifted depth estimates prove the influence of a negligible current vector. This is best explained in Figure 6.1, where the difference between the top panel depth estimates (i.e. Non-Linear Regression vs. Intrinsic) is approximately 1 m. The difference between the dispersion shells at the highest energy is virtually indistinguishable. This clearly shows how X-band radar depth inversion is extremely sensitive.

Maximum Horizontal Tide

The same plots presented for the slack tide times are also used for both the maximum flood current (Figure 6.3) and for the maximum ebb current (Figure 6.4).

The validation with a maximum current gives the same finding - **XM**Fit is visually fitting the spectra energy extremely well. The magnitude and directionality of the estimated current vectors shows a good agreement with the *in situ* ADCP data, meaning **XM**Fit is doing a good job of recognizing the tide along the Dutch coast. As expected, the intrinsic dispersion shell is wildly inaccurate at estimating the depth in the presence of a current. This is shown in Figure 6.3 and Figure 6.4 since the resulting Intrinsic Fitting method gives incorrect depth estimates.

The maximum flood and ebb current validation figures illustrate the sensitivity of the depth inversion. Both the Assimilated-Current and Assimilated-Depth methods tend to agree visually but their depth estimates are different by nearly 2 m. The difference between the fitting methods is on the order of pixels. The validation shows how an influencing current reduces the accuracy of the depth estimate since the non-linear fitting must balance between the two estimates.

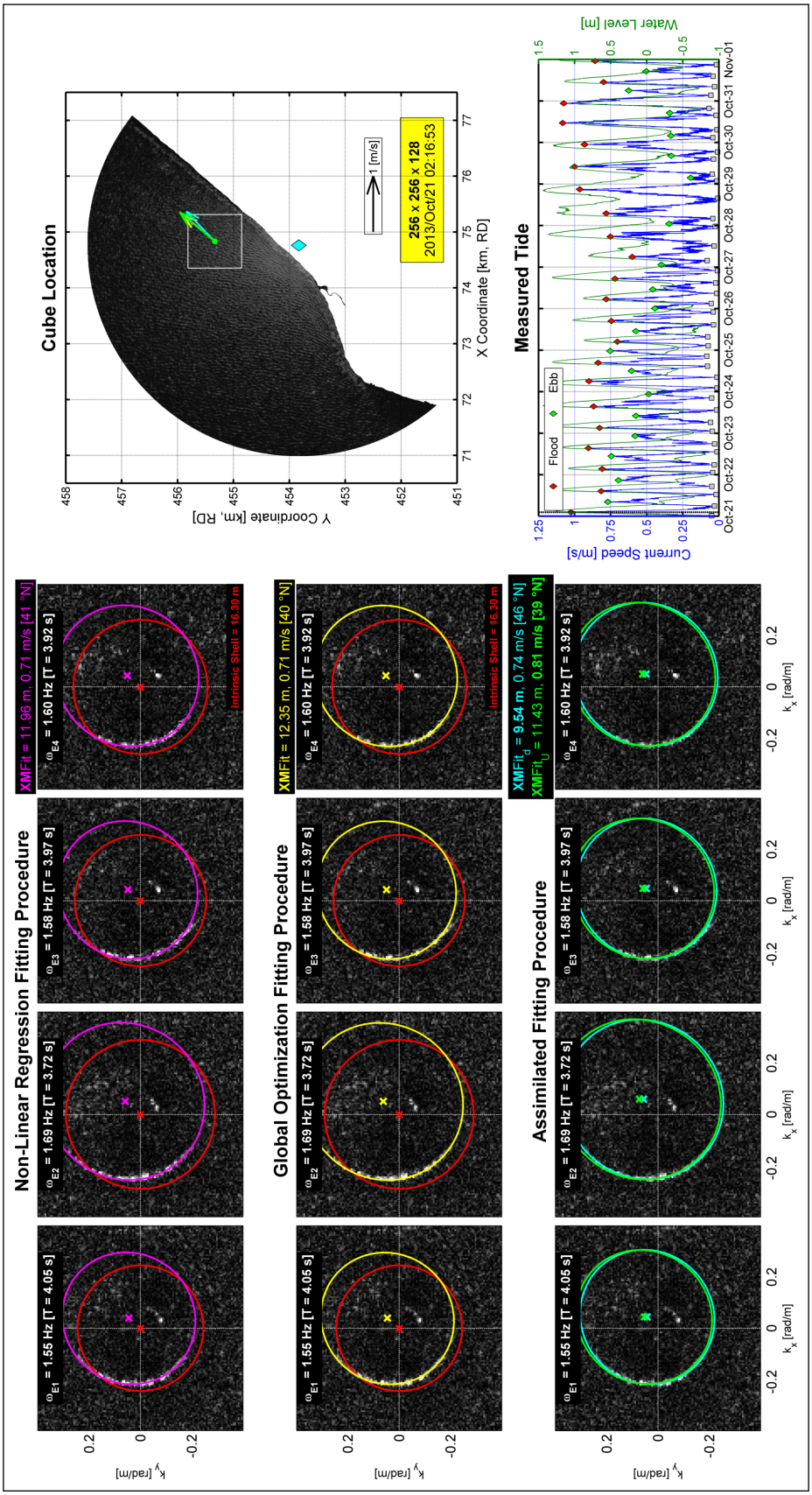

Figure 6.3: XMFit Validation at Maximum Flood Current

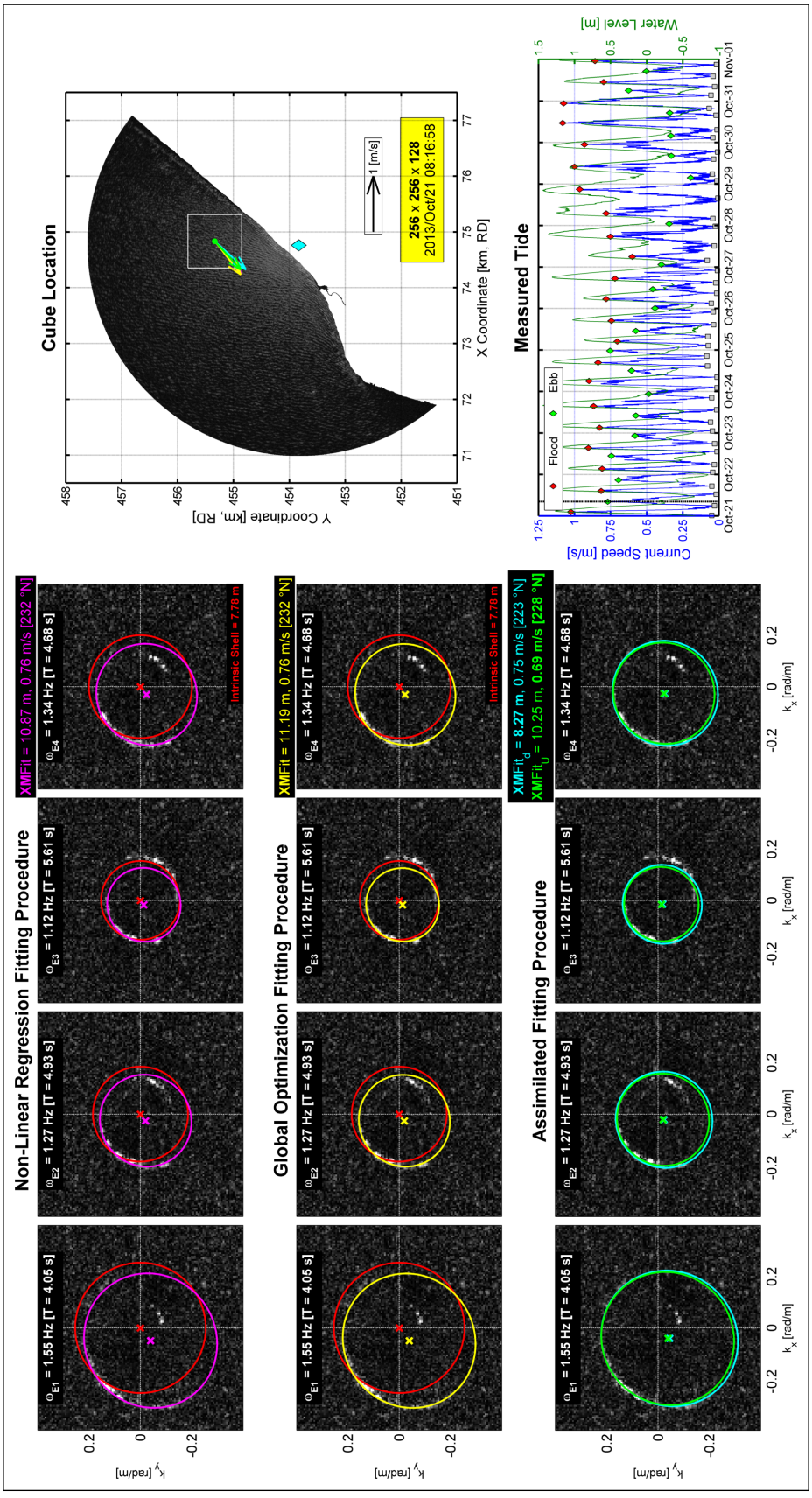

Figure 6.4: XM Fit Validation at Maximum Ebb Current

6.3 Temporal Validation

The validation work concludes by determining if the single tide is applicable for the rest of the storm period (approximately 10 days). This section presents direct scatter comparison plots for depth, current speed and direction for the five different fitting methods.

Figure 6.5 shows a very good agreement between the current speed and direction but consistently overestimates the water depth. There appears to be much more scatter in the data during flood tide opposed to slack or ebb. This is potentially caused by the freshwater plume from the mouth of the river Rhine. This is later investigated in Chapter 8.2. The directionality of the tide using the Levenberg-Marquardt fitting method agrees very well with reality. Note the scatter evident during slack water current directions is not important since the current speeds are minimal.

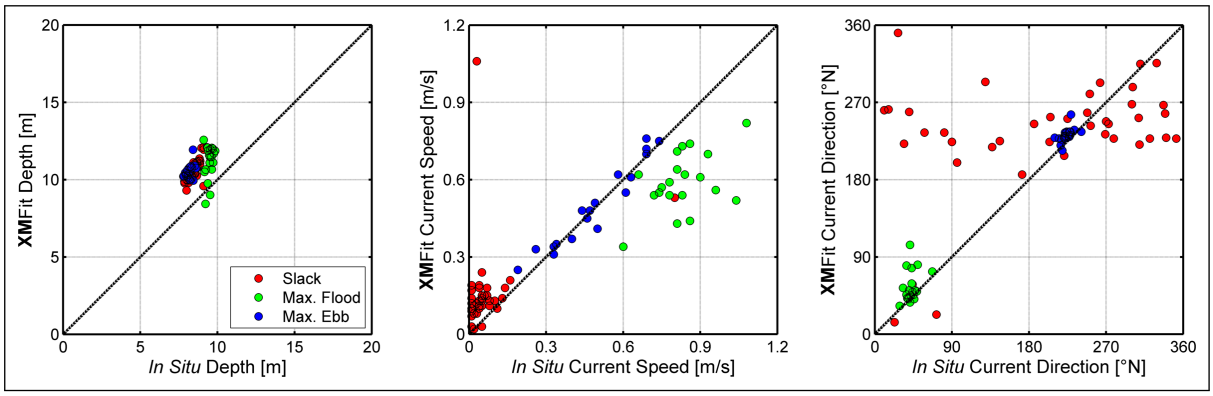

Figure 6.5: Temporal Validation with `nlinfit.m`

Figure 6.6 shows near-identical results to Figure 6.5. This shows that the depth inversion procedure is **insensitive** to the non-linear fitting method. This is an unexpected result since the Global Optimization method using `lsqnonlin.m` includes the Jacobian, which should result in more accurate hydrodynamic estimates.

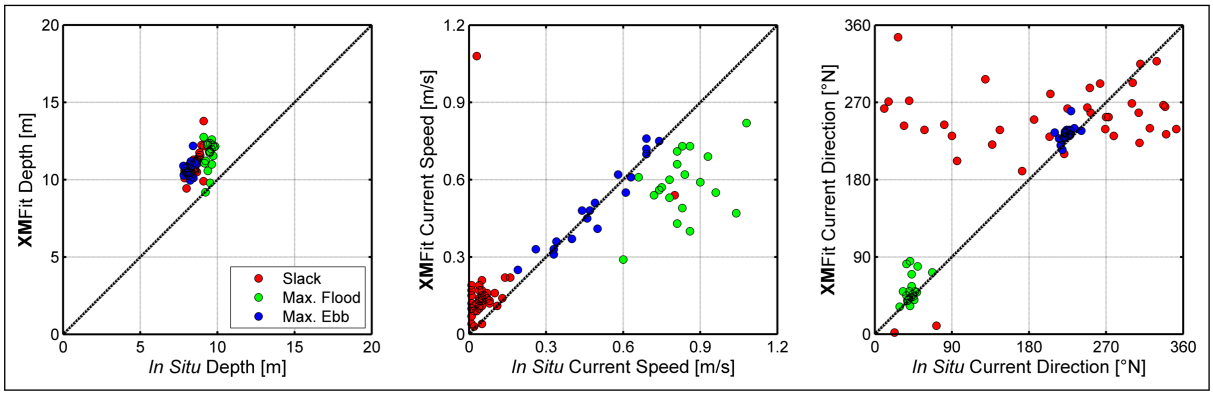

Figure 6.6: Temporal Validation with `lsqnonlin.m`

The intrinsic validation results shown in Figure 6.7 agree with the underlying theory. The intrinsic linear dispersion shell is only able to accurately estimate the water depth during

slack tide. The estimates during maximum flood and ebb are wildly inaccurate with errors upwards of 8 m. The intrinsic fitting method at slack tide still shows the same result - **XM**Fit overestimates water depths.

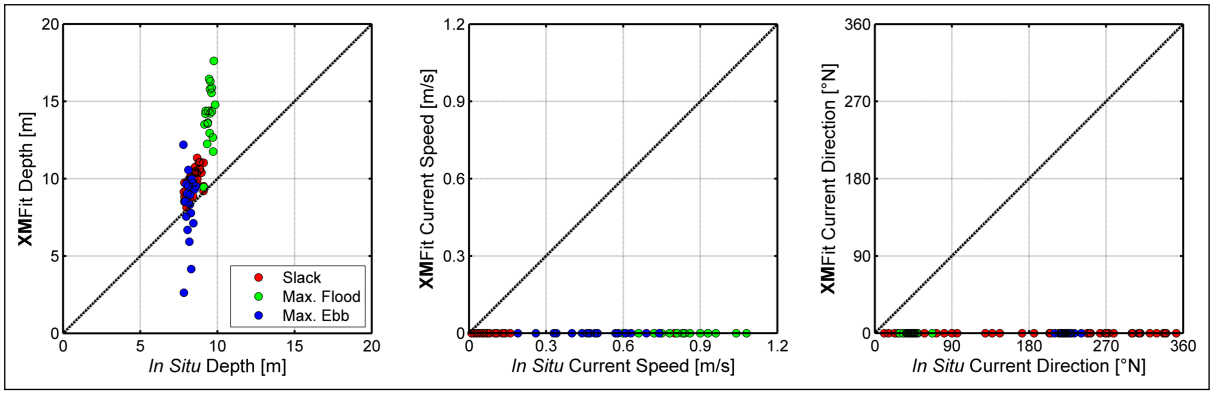

Figure 6.7: Intrinsic Temporal Validation

Figure 6.8 indicates the results for depth when the *in situ* current vector is known. The same finding is present - the depth inversion method overestimates water depth. This fact is expected after visualizing a single tidal cycle, which demonstrated the sensitivity of depth inversion physics. Thus, there appears to be **a positive bias in the estimates depths at all times throughout the tidal cycle**.

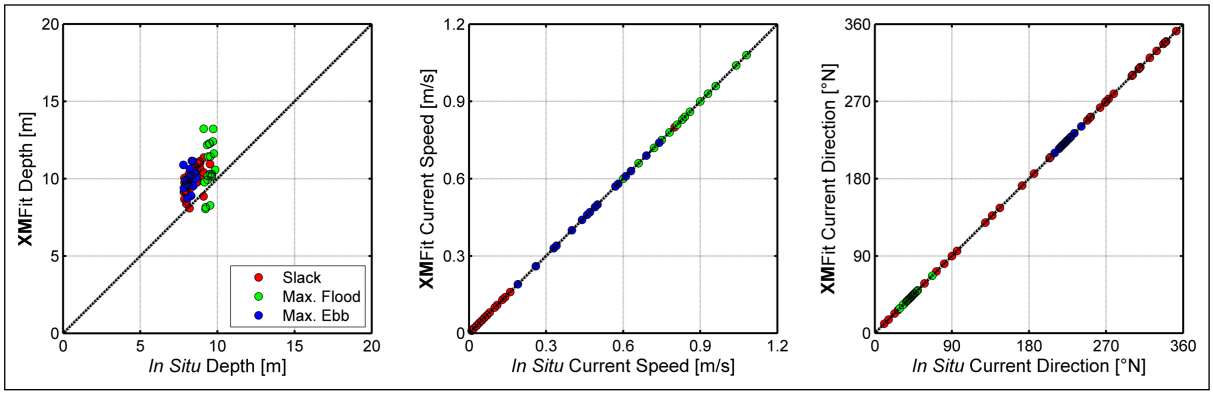

Figure 6.8: Assimilated-Current Temporal Validation

Figure 6.9 indicates the resulting current vector when the *in situ* water depth is known. The results looks similar to both the Non-Linear Regression and Global Optimization estimates. The ebb currents align quite well with the ADCP but the flood currents are underestimated. It is also interesting that the current directions are slightly skewed from the ground truth with the known *in situ* depth.

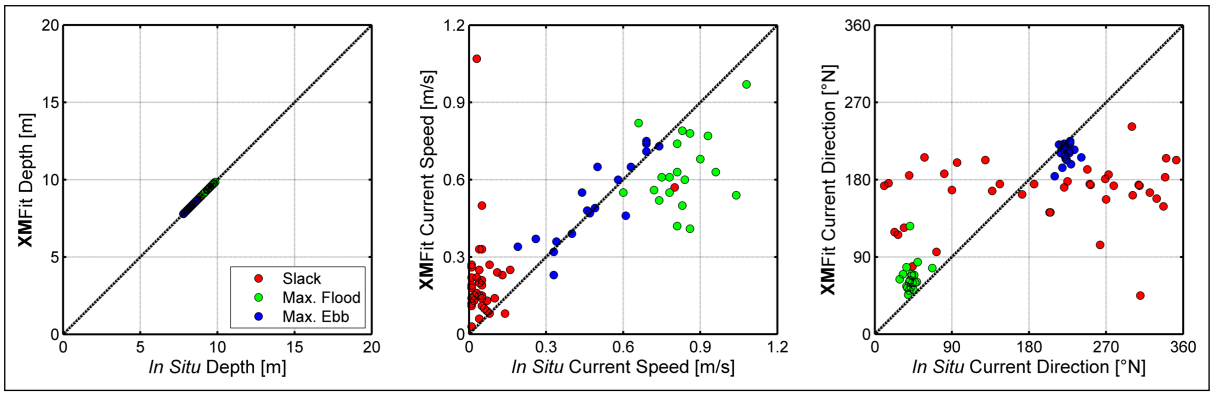

Figure 6.9: Assimilated-Depth Temporal Validation

The validation work proved how the **XM**Fit is insensitive to the non-linear fitting method and the inherit difficulty of solving a single equation with two unknowns. The result is a solution that must balance between the correct depth and the correct current estimate. This validation work presented the complexity of this relationship, which is on the order of pixels.

The most important finding is that known currents overestimate depth and known depth produces scattered current estimates. This is assumed to be attributed to wave shadowing caused by the relatively low antenna height, Λ; see Figure 6.10. This phenomenon technically *misses* wave information, which has the potential to influence the depth inversion procedure. Refer to Flampouris (2010) for more information.

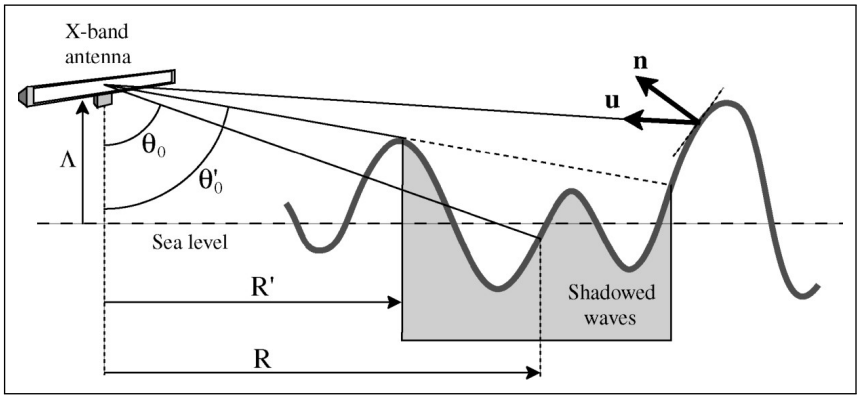

Figure 6.10: Depiction of Wave Shadowing (Nieto Borge et al., 2004)

Although depth inversion is not perfect, it can properly model the physics along the Dutch coast (i.e. precise depth estimate, decent current magnitude estimates, correct tide motion, etc. . .). In conclusion, X-band radar depth inversion implemented in **XM**Fit is an **extremely sensitive method** for retrieving hydrodynamic estimates.

Chapter 7

Storm Results

The results from the **XM**Fit algorithm for the analyzed storm are presented in this chapter. All results are temporally limited from October 21^{st} to November 1^{st}, 2013. This chapter compares **XM**Fit against the *in situ* measurements (refer back to Chapter 4.2) to ensure the algorithm is capable of accurately estimating the measured nearshore hydrodynamics at the Sand Motor. This chapter also presents the same comparison for the SeaDarQ software, in order to provide a benchmark for the current commercial product.

7.1 Direct Water Depth Comparison

A direct water depth comparison is completed by comparing the **XM**Fit estimates with the ground truth, which is a combination of the bathymetric surveys and the measured water level at Scheveningen. The comparison uses all gridpoints from either dataset during the storm in an attempt to quantify the overall accuracy of **XM**Fit, see Figure 7.1.

The **XM**Fit results are shown in Figure 7.1a. The empirical cumulative density function (CDF) agrees nicely in shape but there is a noticeable difference in behaviour in deeper water. The comparison of both CDF curves is a great representation of the goodness of fit. It is able to show the range of values, its mean and quartiles in a single plot. The direct scatter plot is far too noisy given the quantity of data, but indicates that **XM**Fit is consistently overestimating depth. A 2D histogram plot is included with bin sizes of 0.25 m to better visualize the underlying relationship. This shows a clear positive bias in the model of 1.66 m, but it is not entirely uniform with depth.

XMFit results in a non-linear bias for the depth estimate when too deep and too shallow. This is linked back to the linear dispersion relation, which is insensitive to depth in deeper water while being non-dispersive and non-linear in shallow water. The 2D histogram shows that **XM**Fit is capable of estimating water depths up to 3 m with a consistent linear bias.

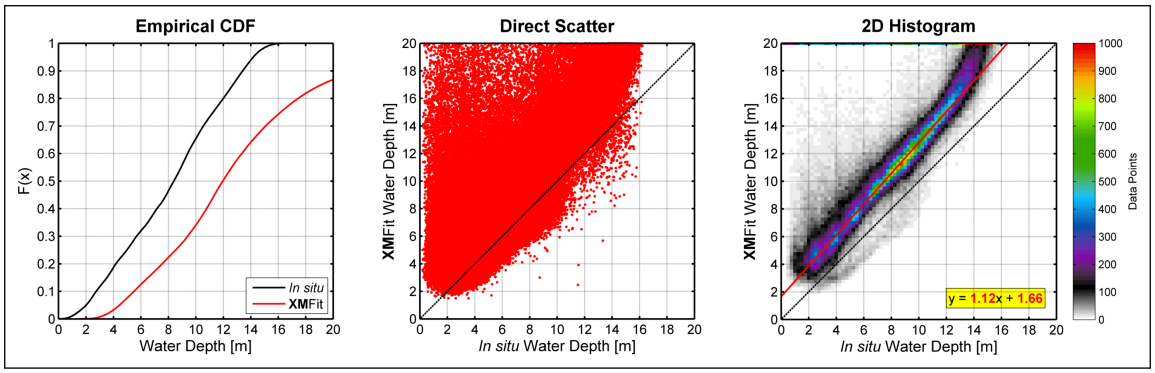

(a) XMFit

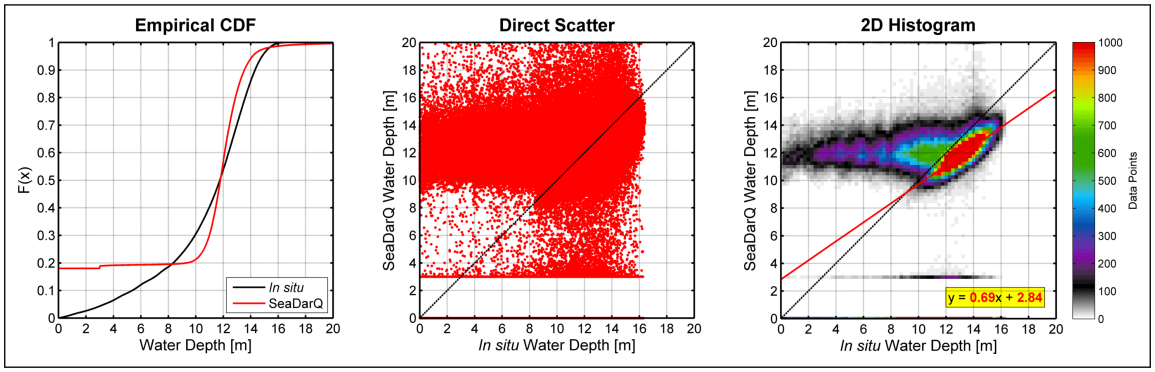

(b) SeaDarQ

Figure 7.1: Direct Water Depth Comparison

The benchmark SeaDarQ results are shown in Figure 7.1b. The empirical CDF plot shows a poor match with the *in situ* data, since it appears to only predict a certain range of water depths. There is approximately 20% missing data due to the internal SeaDarQ quality control, while the rest are limited to a specific range from 10 to 14 m. Although it may appear to visually match the *in situ* data - this does not mean it predicts the correct depths. This is better represented in the direct scatter and 2D histogram plots. The direct scatter is once again misleading since there is too much data but it is clear that SeaDarQ is not deriving the appropriate shape of the Sand Motor bathymetry. The 2D histogram indicates that SeaDarQ is not able to distinguish any bathymetric features, and is limited to a specific range of water depths between 10 and 14 m. It appears SeaDarQ predicts the same water depth range regardless of the actual water depth, in the form of a *drifting cloud pattern*.

7.2 Spatial Statistics

The depth comparison presented two facts: **XM**Fit exhibits a near-constant linear bias at all water depths and SeaDarQ can only predict a specific range of depths. The previous section investigated all gridpoints, but it is of use to identify any spatial pattern within the radar domain. The spatial statistics are completed by analyzing each gridpoint from either **XM**Fit and SeaDarQ against the *in situ* ground truth. The linear rank correlation coefficient, the

root mean squared error (RMSE) and the linear bias are determined for each gridpoint, see Figure 7.2.

The **XM**Fit spatial statistics are presented in Figure 7.2a. The highest correlation is directly in front of the radar unit at approximately half the total range. This finding is reinforced with the RMSE statistic, which indicates minimum error close to the radar unit with large errors around the perimeter of the domain. The spatial RMSE pattern shows a clear link between edge effects and accuracy. The linear bias shows a clear relation with depth since it increases offshore. The high RMSE at the edges of the domain is assumed to be a product of the reduced resolution and higher noise in the radar signal at larger ranges. This finding follows Bell (2008), who also found poor results at the extents of the radar range.

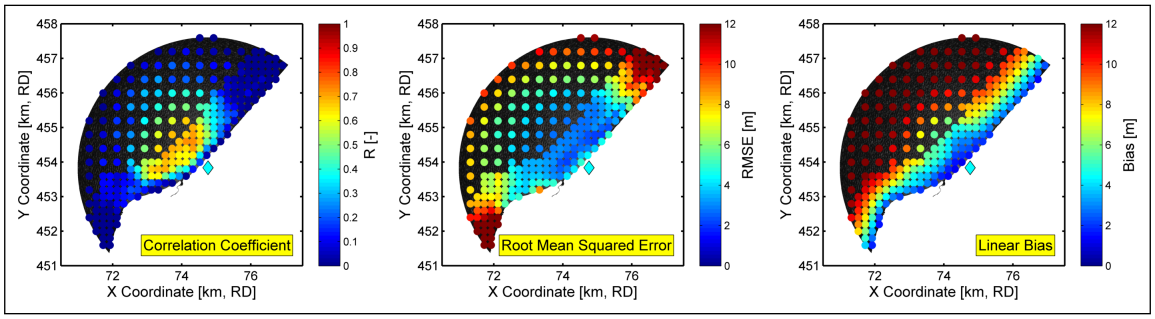

(a) XM Fit

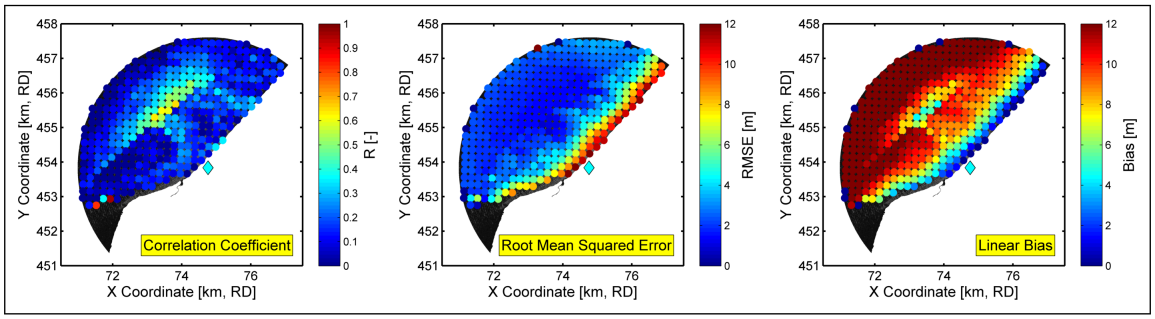

(b) SeaDarQ

Figure 7.2: Spatial Statistics

The SeaDarQ results in Figure 7.2b show a very poor correlation throughout the entire domain. The exception is a small offshore area where the *in situ* depth is in fact closest to the range SeaDarQ can predict (i.e. 10 to 14 m). SeaDarQ shows minimal error in deeper water since the true depth aligns with its inherit depth limitation. The highest error is clearly in the nearshore since SeaDarQ is not able to predict any depths shallower than 10 m. Lastly, the linear bias is assuming an unrealistic horizontal line between the SeaDarQ and *in situ* data given the presence of the *drifting cloud pattern*.

A single instantaneous result for both **XM**Fit and SeaDarQ is included in Appendix C. This random timestep helps illustrate that SeaDarQ is not able to distinguish a bathymetric gradient, whereas **XM**Fit is able to predict realistic results.

7.3 Timestack Visualization

A cross-shore timestack plot is included to visualize the tidal motion throughout the radar domain. The goal is to determine how well both models derive the actual bathymetric gradient in time. Five shore normal profiles were extracted from both the **XM**Fit and SeaDarQ results and compared against the *in situ* water depths. Each extracted profile is plotted in a separate subplot and labeled from A to E. The x-axis represents time and the y-axis indicates the distance offshore along the profile. The **XM**Fit results are in Figure 7.3 and the SeaDarQ results are in Figure 7.4. The colour scale is constant for all plots, ranging from 0 to 20 m.

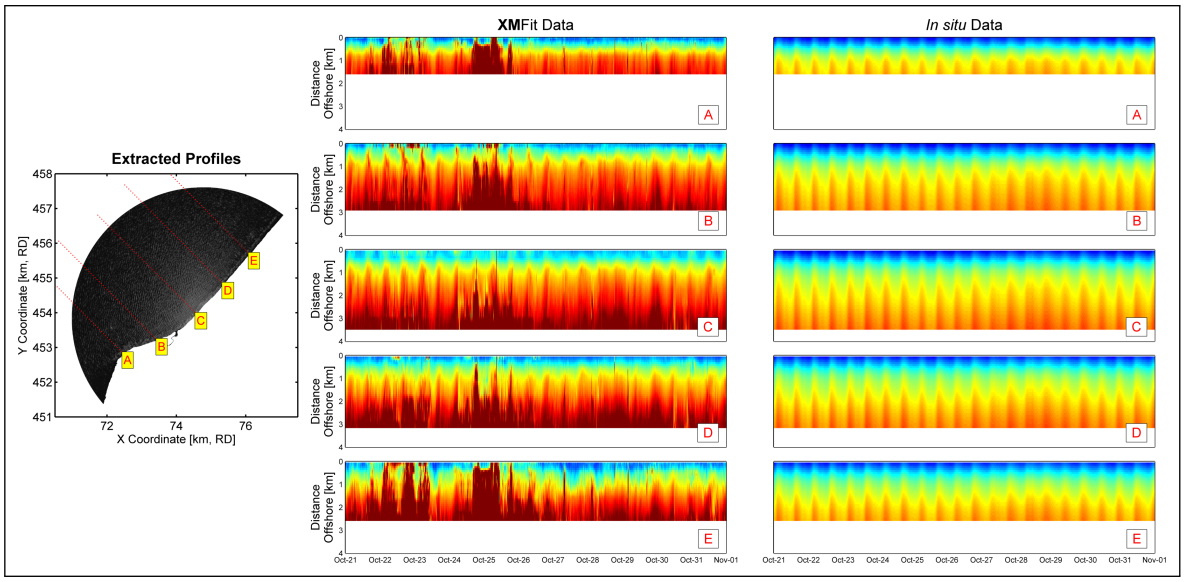

Figure 7.3: **XM**Fit Cross-shore Timestack

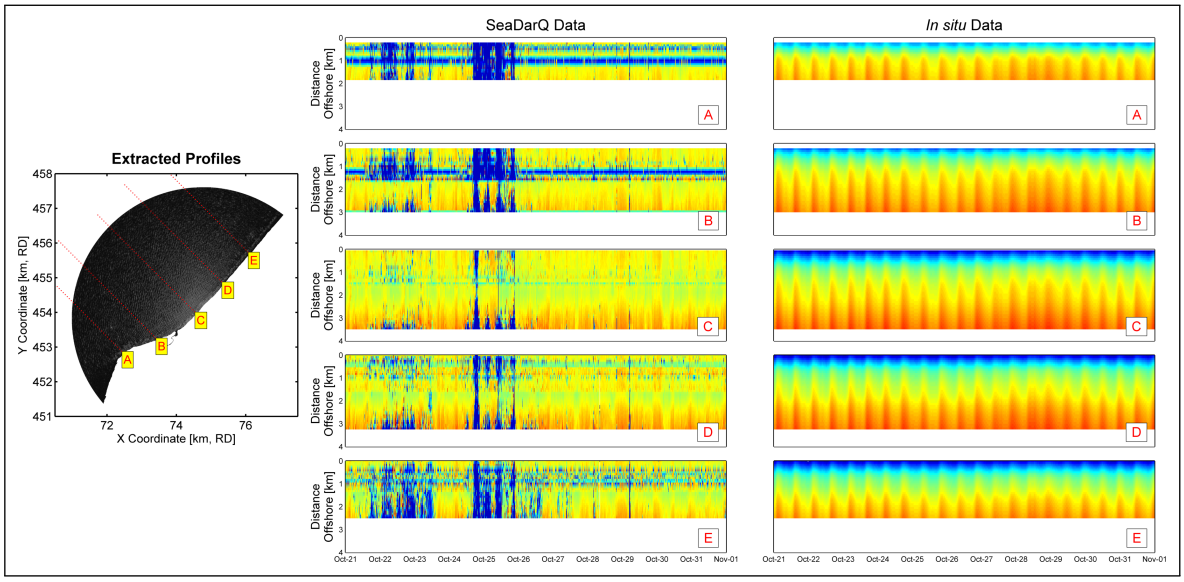

Figure 7.4: SeaDarQ Cross-shore Timestack

The timestack visualization helps reinforce the same findings. **XM**Fit is able to extract the full range of depths at the Sand Motor but has issues at the edges and consistently overestimates the water depth. SeaDarQ does not suffer from any edge issues but is not able to replicate any sort of bathymetric gradient at the Sand Motor.

Lastly, the timestack plots help identify temporal periods of poor data quality such as October 25^{th}, 2013. This is evident based on extremely deep **XM**Fit estimates and missing data in SeaDarQ. This is further investigated in Chapter 7.5.

7.4 *In situ* Comparison

An *in situ* comparison with the deployed ADCP and wave buoy is presented in this section. Background information regarding both instruments is found in Chapter 4.2. The closest point for both the **XM**Fit and SeaDarQ grids is extracted to spatially represent each *in situ* device. The SeaDarQ and **XM**Fit grids are not the same, thus giving different nearest gridpoints. The time comparison between the ADCP and the two depth inversion models is shown in Figure 7.5. All comparisons made with the ADCP use the near-surface current vector given the uncertainty regarding where the radar-derived current acts in the water column.

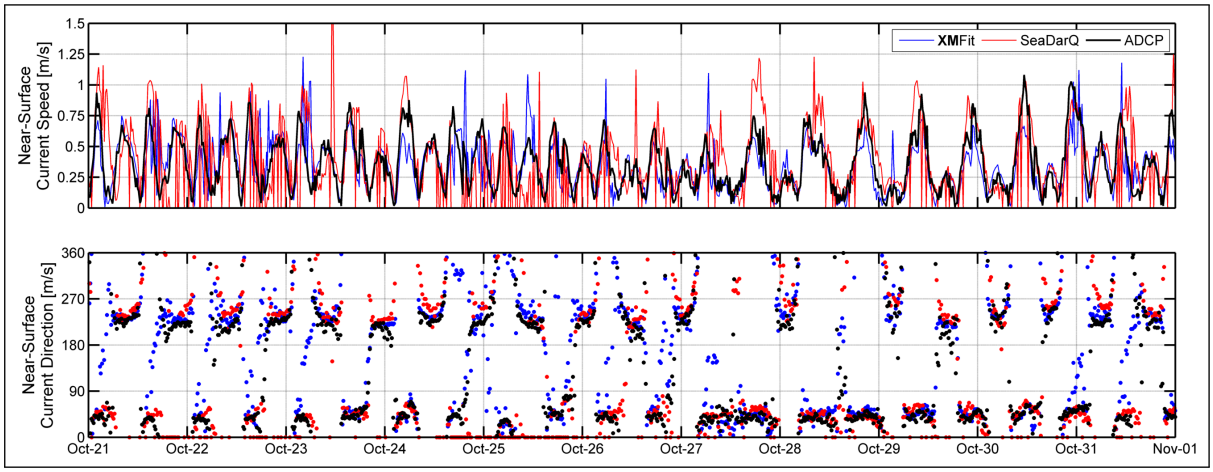

Figure 7.5: ADCP Timeseries Comparison

Both **XM**Fit and SeaDarQ perform very well when identifying the horizontal tide at the Sand Motor. The raw results are plotted to compare the precision of either model against the measured data. Surprisingly, the asymmetry of the tide is represented by both **XM**Fit and SeaDarQ. The directionality of the tide propagating along the Dutch coast aligns nicely with the ADCP. Differences are shown during the flood tide in the **XM**Fit results, which are later discussed in Chapter 8. The current directions estimated by SeaDarQ align quite well with the ADCP but its current speeds are much noisier than **XM**Fit. It is much easier to identify trends between the two depth inversion models and the *in situ* data using direct scatter comparisons for both current speed and direction (Figure 7.6).

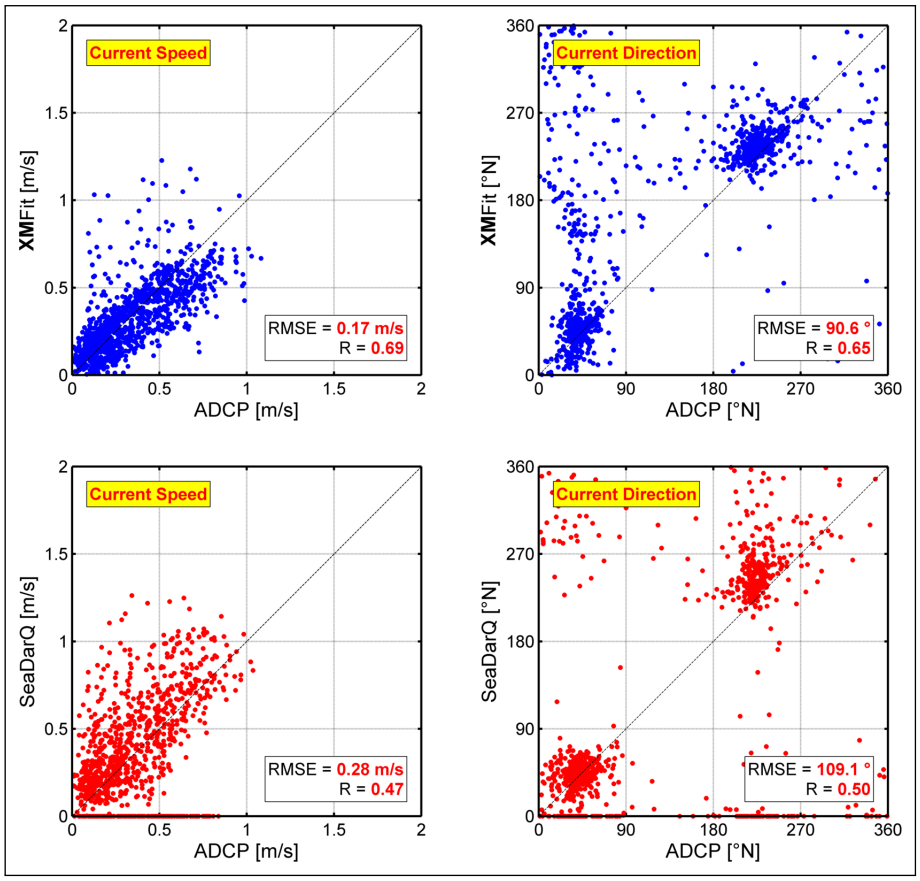

Figure 7.6: ADCP Direct Scatter Comparison

The current speed estimates from **XM**Fit are less scattered than SeaDarQ. This is indicated through the statistical parameters for both models. The **XM**Fit data shows a good correlation of 0.69 and a low RMSE of 0.17 m/s for current speed. SeaDarQ has a lower correlation of 0.47 and a higher RMSE of 0.28 m/s. The current directions are more interesting since **XM**Fit has issues with resolving the flood currents, while SeaDarQ tends to show more scatter during ebb tide. In conclusion, both **XM**Fit and SeaDarQ perform really well with respect to the deployed ADCP. **XM**Fit is preferred given its improved statistics and its more realistic inability to accurately model complex flow patterns during flood currents.

Lastly, the deployed wave buoy is a useful qualitative metric for confidence in the methodology. The peak period indicates that the correct spectra energy was selected during the non-linear fitting procedure, while the peak wave direction is directly linked to selecting a suitable minimum energy cutoff. Refer back to Chapter 5 for more information regarding the depth inversion procedure. Figure 7.7 compares the timeseries data of the wave buoy against both **XM**Fit and SeaDarQ. It is evident that both **XM**Fit and SeaDarQ routinely select a different peak energy level, but the peak wave direction shows good agreement with the *in situ* data. The wave buoy comparison also shows a much poorer relation during October 25^{th}, similar to the finding in Chapter 7.3. This raises the question - *what is influencing the quality of radar derived hydrodynamics?*

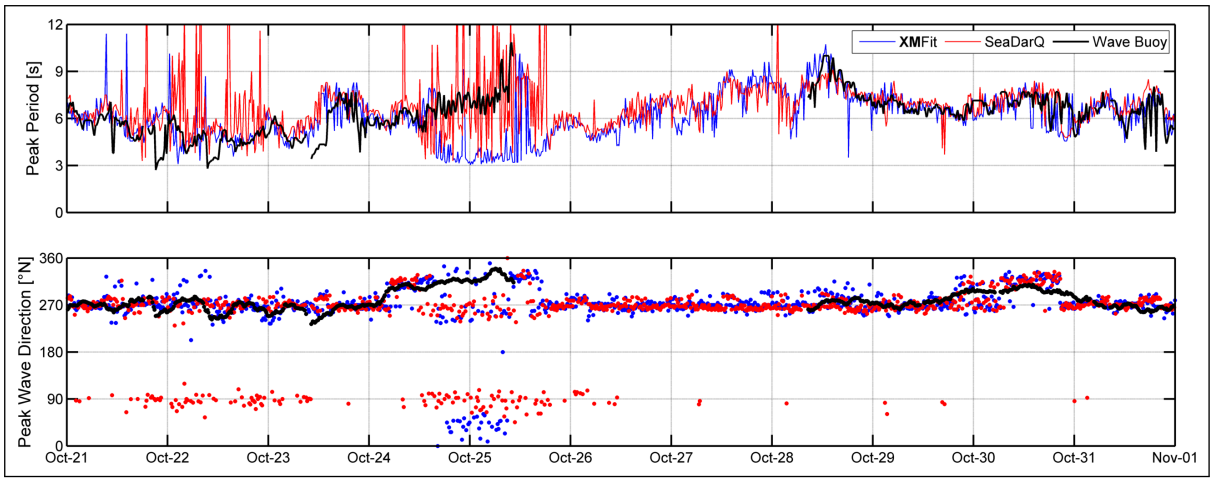

Figure 7.7: Wave Buoy Comparison

7.5 Temporal Statistics

The temporal statistics of both **XM**Fit and SeaDarQ are investigated to better understand how X-band radar accuracy varies as a function of time. The temporal statistics are determined based on comparing the surfaces in time between the model (**XM**Fit or SeaDarQ) and the *in situ* data. The linear rank correlation, the root mean squared error (RMSE) and the linear bias are shown for both models in Figure 7.8.

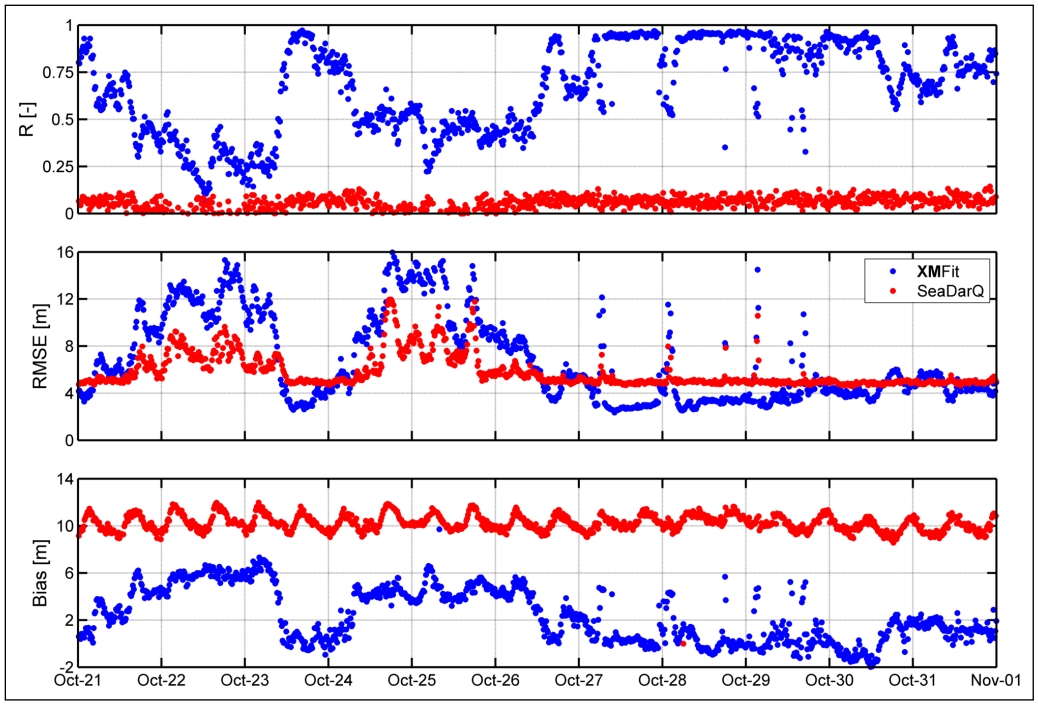

Figure 7.8: Temporal Statistics

The **XM**Fit data shows the expected trend where the linear correlation is inversely related with RMSE. This is shown by October 23^{rd}, where the correlation is maximized and the root mean squared error is minimized. The linear bias in **XM**Fit aligns with the RMSE, indicating that high error worsens the line of best of fit between the surfaces. The temporal statistics between SeaDarQ and the *in situ* data do not present any interesting findings except that the RMSE aligns with the same inaccurate periods evident in the **XM**Fit data.

Therefore, there are inherit sensitivities in the radar data that should be further investigated. A more in-depth analysis linking the radar accuracy with the coastal climate is presented in Chapter 8.

Chapter 8

Discussion

The storm results provided convincing evidence that the **XM**Fit algorithm is more accurate than SeaDarQ. This conclusion is limited to the duration of the storm and for the Sand Motor. This chapter investigates what factors influence the quality of **XM**Fit estimates. Only the **XM**Fit results are used for this analysis since it better reflects the physical processes at the Sand Motor (i.e. real bathymetric gradient, tide propagation along the coast, potential stratification issues, etc. . .).

8.1 Ideal Conditions

This section attempts to explain the consistent overestimation of depth in **XM**Fit and to develop a relationship between radar quality and the metocean climate. This is achieved by finding *ideal* conditions that align with periods of high accuracy from the **XM**Fit temporal statistics in Figure 7.8. The hope is that ideal conditions will help reduce the linear bias and edge effects by analyzing a smaller spatial and temporal subset of the **XM**Fit estimates.

8.1.1 Spatial Limits

The spatial statistical analysis from Chapter 7 provided insight into locations around the edge of the radar domain plagued with inaccurate estimates. As mentioned, this is likely due to lower resolution at larger ranges, which results in a lower signal to noise ratio. The most accurate zones are separated from edge effects by adding a radius cutoff from the radar unit. The result is a reduced radar footprint. An iterative analysis was completed to identify the most suitable radius cutoff to improve the quality of **XM**Fit, see Figure 8.1.

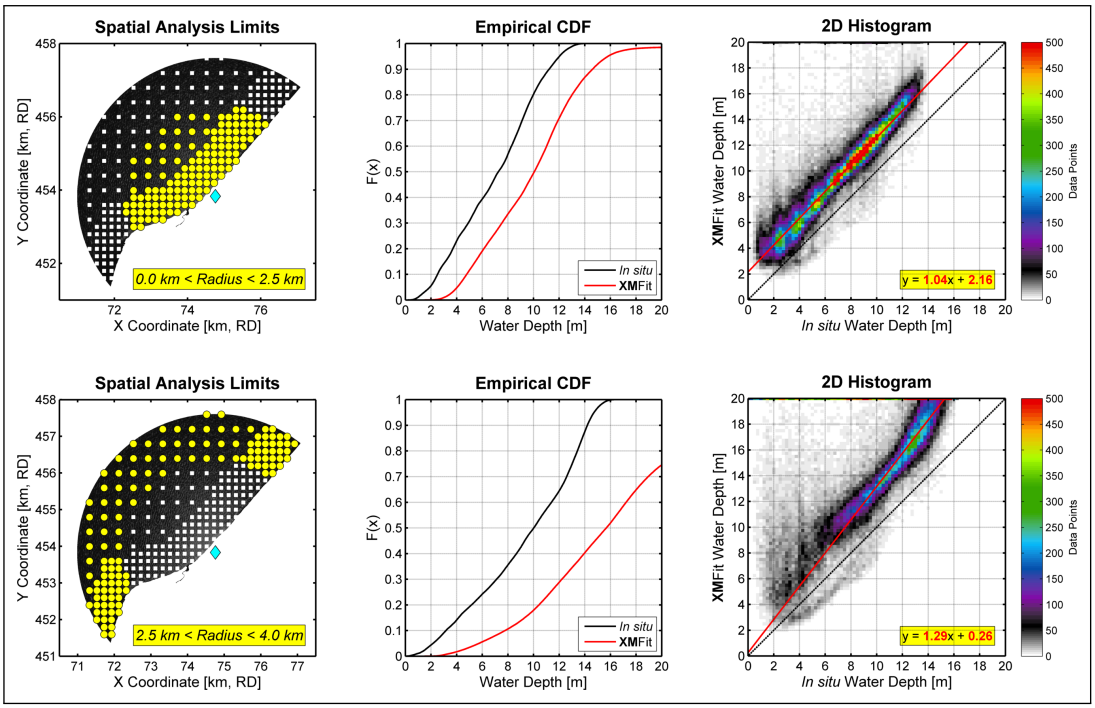

Figure 8.1: Relationship between **XM**Fit Accuracy and Radius

A spatial cutoff is found at a distance of 2.5 km from the radar unit. The empirical cumulative density function (CDF) in the top panel (i.e. only data within 2.5 km) shows great agreement with the *in situ* data. The bias evident throughout the entire storm period in **XM**Fit is still present, but its shape reflects the natural bathymetric gradient at the Sand Motor. The edge data in the bottom panel (i.e. data outside of 2.5 km) shows a poor relation with the ground truth. The edge data does not align whatsoever with reality and consistently predicts extremely deep depths. The spatial quality limit is also apparent in the 2D histogram plots since an improved relation is clearly visible for the reduced radar footprint.

Therefore, **XM**Fit is in fact precise at extracting radar-derived hydrodynamics within a reduced footprint of 2.5 km, but still exhibits a consistent positive linear bias.

8.1.2 Metocean Limits

The metocean climate presented in Figure 4.5 is used to interpret the trends in the temporal accuracy (Figure 7.8). It is believed that a physical parameter is influencing radar quality since its main input (i.e. Bragg scatter) requires surface waves. A qualitative sensitivity analysis found that wave height, peak period, wind speed and the direction between waves and wind are most important for accuracy. Figure 8.2 shows their influence with the temporal linear bias in **XM**Fit. This statistical parameter was selected for analysis since it corresponds with the overestimation of depth. Note that data gaps exist since the wave buoy was not functioning throughout the entire duration of the storm.

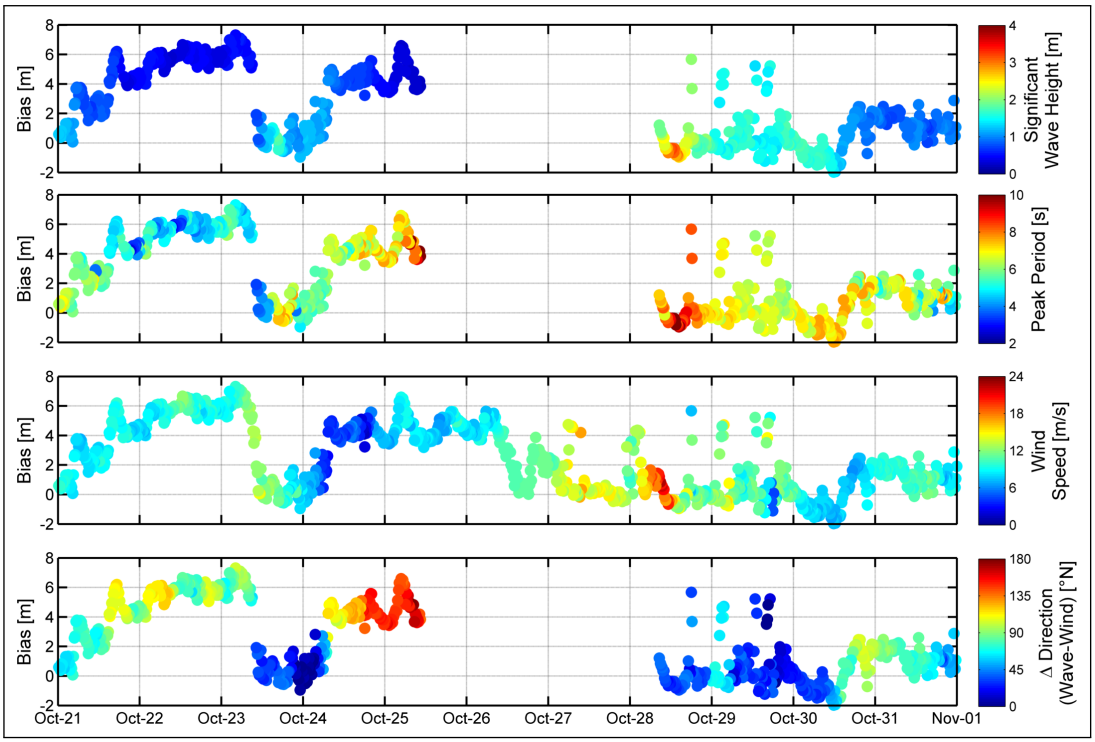

Figure 8.2: Temporal Linear Bias with the Metocean Climate

High bias values indicate inaccurate radar estimates, while low biases represent high confidence in the accuracy of **XM**Fit. A clear distinction is evident during October 23^{rd} and from October 27^{th} to 30^{th}, where the linear bias is close to zero. This temporal pattern is readily visible in the significant wave height data, where the lowest waves align with high biases. This makes sense according to the underlying theory, since the depth inversion algorithm within **XM**Fit requires wave celerity information, which is not possible without any waves.

The peak period is included to show the lack of a relation with radar quality. This could be influenced by the limited nature of the analyzed waves, or that peak period solely dictates the main frequency level of the spectra data. The wind speed is quite scattered with respect to the linear bias. The peak wind speed aligns with a period of good quality but low winds do not necessarily mean poor quality. The forcing direction is best represented as the difference between the waves and wind, since their alignment increases the likelihood of wave generation. The directional forcing clearly shows low biases during periods where the waves and wind align, with a significant drop in quality at other times. This helps indicates the importance of waves on radar accuracy. Note that this finding also aligns with Bell (2008), who commented on the requirement of waves for accurate results. Thus, higher wind speeds that generate onshore directed waves increase accuracy in **XM**Fit. The next question remains - *is it possible to define quantitative cutoffs associated with the metocean climate?*

The sensitivity analysis presented the logical dependence of **XM**Fit on the presence of waves. The actual *ideal* cutoff is uncertain, but is somewhat evident in Figure 8.3. The correlation, root mean squared error (RMSE) and the linear bias are plotted against the significant wave height, peak period, wind speed and forcing direction. This plotting technique allows for the possibility of identifying distinct thresholds that align with accurate **XM**Fit results.

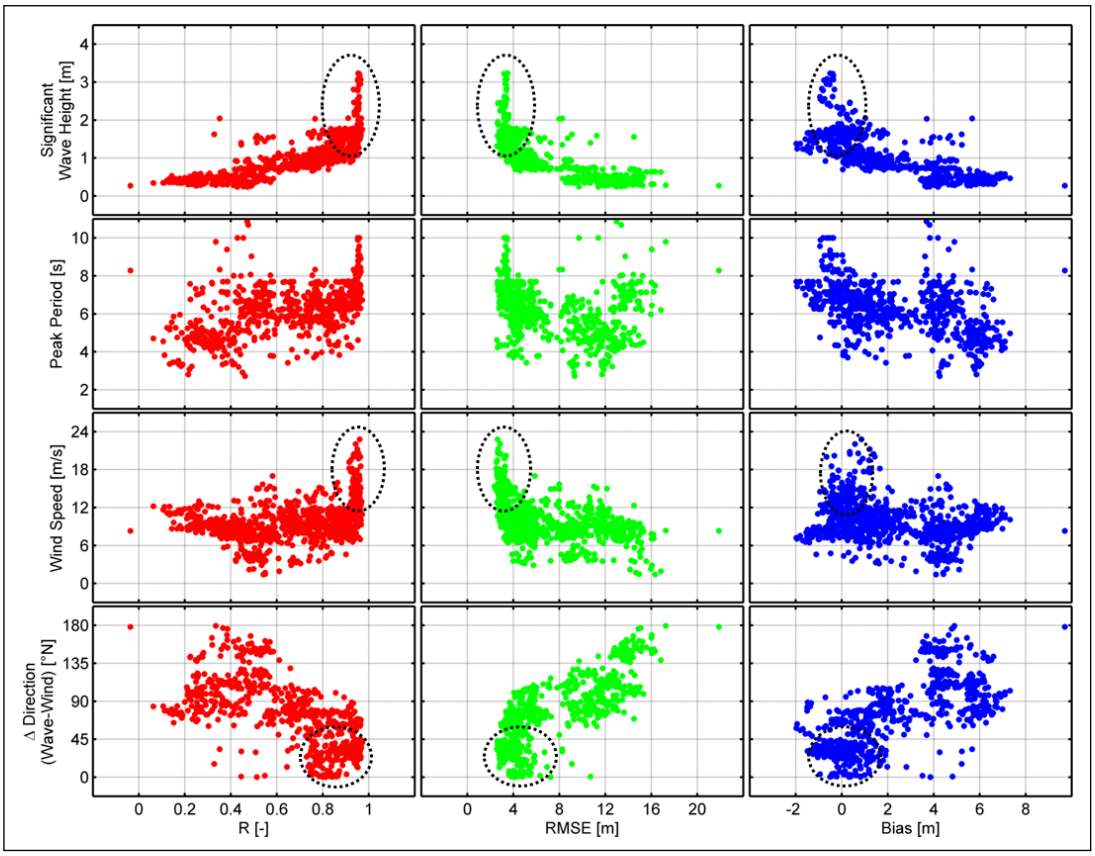

Figure 8.3: Relationship between **XM**Fit and Metocean Data

The following metocean limits are associated with periods of high accuracy in **XM**Fit.

- Significant wave heights greater than **1 m**
- Wind speeds greater than **12 m/s**
- Wind and waves are aligned within **45°**

8.1.3 Ideal Accuracy

It is now of interest to quantify how well **XM**Fit compares against the *in situ* data under ideal conditions. This is completed in Figure 8.4, which presents the statistical fit of **XM**Fit with the three metocean limits. It is visualized in this manner since the relative sensitivities of the parameters are unknown. The aim is to determine which parameter (i.e. waves, wind, forcing direction) is most influential in reducing the linear bias in **XM**Fit. The benchmark linear bias is found in Figure 8.1, with a value of 2.16 m. The original linear bias for the entire radar domain was 1.66 m (see Figure 7.1a) but that is not applicable for comparison since it included the known edge issues. Its inclusion resulted in a non-constant linear bias in both shallow and deep water.

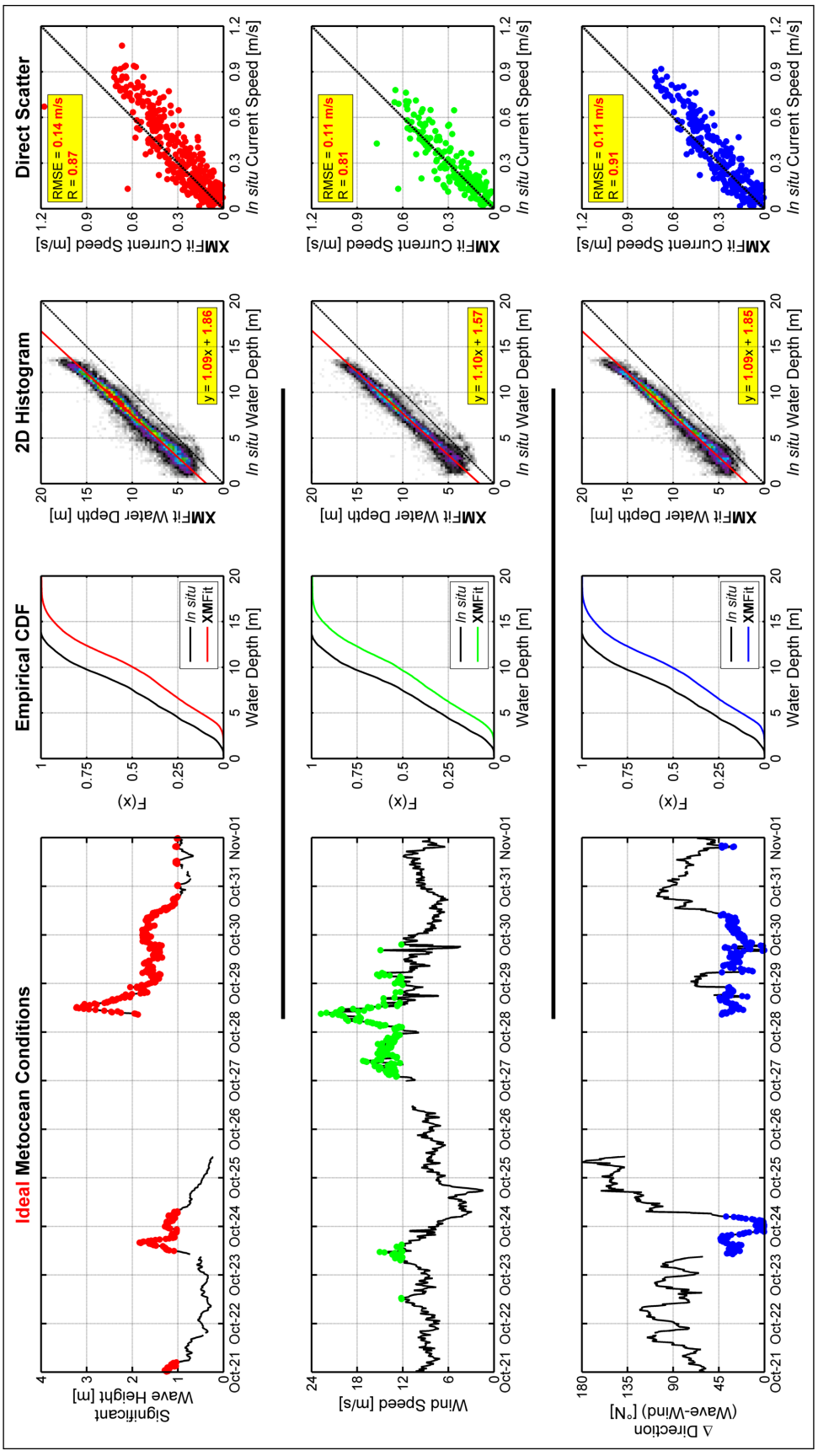

Figure 8.4: Ideal **XM**Fit Accuracy

The above plot is identical for each metocean limit. The wave height limit of 1 m is shown in the top panel (in red), the wind speed threshold of 12 m/s is in the middle panel (in green) followed by the alignment of the waves and wind (in blue). The selection of ideal times for each metocean limit is not constant, requiring different temporal *in situ* data to judge the quality of **XM**Fit. Each metocean limit consists of four plots to best present the accuracy of **XM**Fit. The ideal metocean conditions indicate which times are used for the *in situ* comparison, followed by the empirical CDF and 2D histogram to identify the water depth estimates. Lastly, a direct scatter of the estimated **XM**Fit current speed against the ADCP is included. Note that this analysis includes the reduced radar footprint of 2.5 km.

All ideal settings indicate improved accuracy at the Sand Motor. The general shape of the CDF better matches the *in situ* data, the linear bias is further reduced, and less scatter is evident since edge effects are removed. The current speed estimates have improved when comparing against the previous benchmark (R = 0.69, RMSE = 0.17; see Figure 7.6).

A premature conclusion is that waves of 1 m are most important for **XM**Fit accuracy. This is logical since wind speed and forcing direction are the main mechanisms driving wave generation. It also makes sense given how wave celerity is the foundation of the depth inversion procedure. Unfortunately, the single cutoff value is an oversimplification that does not adequately reflect what **XM**Fit *requires* for accurate fitting of the dispersion relation.

XMFit requires spectra spreading in $k-\omega$ space to help *constrain* the dispersion shell. More spreading around the shell drastically increases the accuracy of d and $\vec{U}$. This spreading corresponds with wind sea since locally generated wind waves have a certain degree of randomness with respect to wavelength and frequency. Note that swell would exhibit a narrower spectrum and is not necessarily influenced by strong or aligned winds.

Therefore, it is possible to make a better conclusion that wind and waves are the most important proxies for **XM**Fit quality. Wind speed generates waves, which are necessary for depth inversion, and their alignment gives information regarding their generation mechanism. In conclusion, **XM**Fit is most accurate within a reduced radar footprint of 2.5 km and with *wind sea* of at least 1 m.

8.2 Complex Flow Structures

This section presents a preliminary investigation into the complex flow structures evident at the Sand Motor. It is primarily focused on understanding the inaccuracy of **XM**Fit currents during specific periods. Two processes at the Sand Motor are further researched - stratification and the consistent large-scale eddy that forms during each tidal cycle.

Influence of Stratification

The outflow of the river Rhine is approximately 10 km southwest of the Sand Motor, which results in a freshwater plume passing the radar footprint. This phenomenon only occurs during flood tide due to the propagation of the tide along the Dutch coast. The influence of stratification on the accuracy of **XM**Fit is currently unknown but its potential influence is evident in Chapter 7.4. Swinkels et al. (2012) recommended further research into its influence on radar-derived hydrodynamics, but it is difficult to further pursue without knowledge of the *in situ* density profiles around the Sand Motor. Figure 8.5 shows the direct scatter comparison for the current speed during flood and ebb.

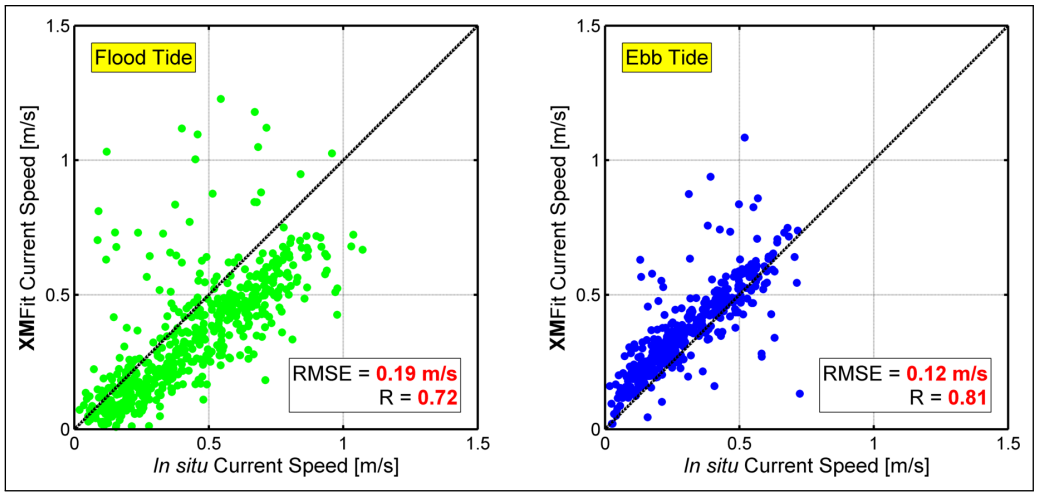

Figure 8.5: Influence of Tide on **XM**Fit Current Estimates

There is an obvious difference between the two current magnitudes. The ebb tide matches quite well with a very high correlation coefficient and minimal scatter. The flood results are more scattered and typically underestimate the *in situ* measurement. This inaccuracy during the flood tide raises the same issue of not understanding exactly what radar-derived currents represent in the water column.

Figure 8.6 shows the effect of stratification by extracting two timestack-averaged radar images, which are approximately 6 minutes in duration. They were selected to coincide with the passing density front during the flood tide (Figure 8.6a) and then its return along the coast during the beginning of the ebb tide (Figure 8.6b).

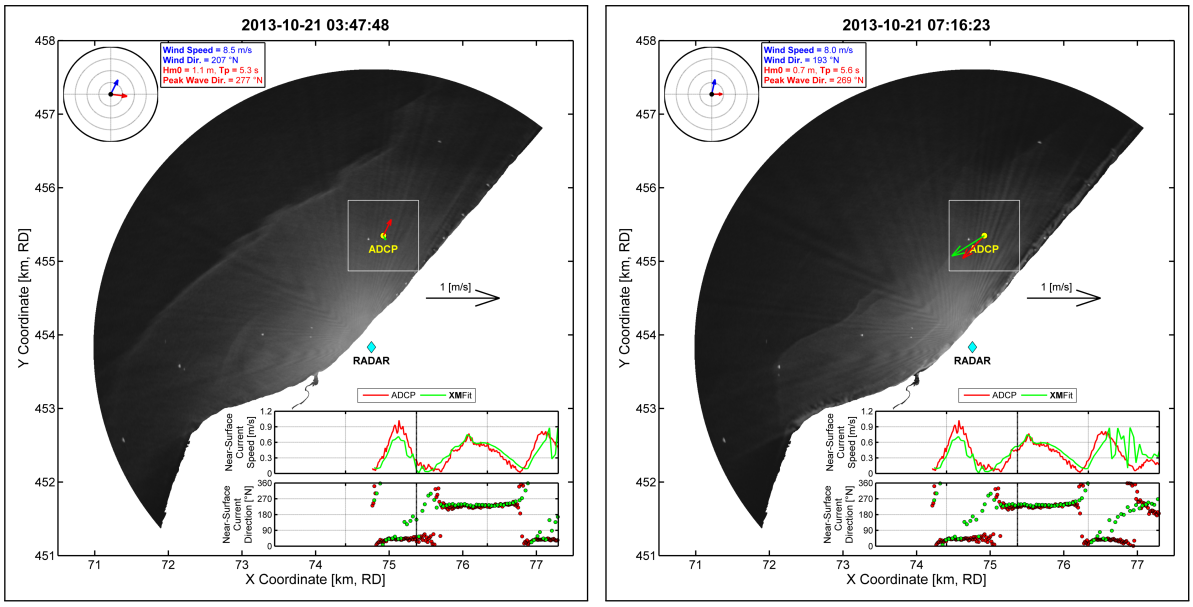

(a) Flood Tide **(b)** Ebb Tide

Figure 8.6: Timestack-Averaged Radar Images

The two images give a great deal of insight into the processes affecting the hydrodynamics at the Sand Motor. The images are obviously two-dimensional, but the stratification effects are in fact three-dimensional due to vertical shear in the water column. The ebb tide results align extremely well with the ADCP, but the flood tide estimates disagree with the measurements. This mimics Figure 8.6, which clearly shows the passing freshwater plume during flood tide. Although it is not possible to make any hard conclusions, **XM**Fit shows a relation with the density front but it is being simplified by the large computational cube.

Influence of the Large-Scale Eddy

The presence of the large-scale Sand Motor nourishment influences the propagation of the tide due to partially blocking the propagation of the tide. This is evident during both flood and ebb tide by the formation of a large-scale eddy. This section is limited to the flood tide since the ebb tide circulation patterns are outside of the radar domain.

Delft-3D model results from an operational model previously setup along the Dutch coast in 2010 by Deltares and Imares (2012), within the scope of the pilot swimmer safety are shown in Figure 8.7a. The instantaneous current field during a typical flood tide indicates the formation of a large-scale eddy on the lee side of the Sand Motor. The large computational cube used in **XM**Fit is superimposed atop the simulation results to highlight its spatial extents. **XM**Fit estimates a single *average* current vector influencing the propagating waves, which is assumed to act at the ADCP location. The yellow current vectors that are within the computational cube show the large simplification of the resulting hydrodynamics. They show a distinct gradient in flow velocity, due to the influence of the nearby large-scale eddy. In essence, the resolved current vector in **XM**Fit is the average behaviour of the hydrodynamics within the large computational cube, which is not representative of the typical large eddy formed on the

lee of the Sand Motor during flood tide. This is best presented by the timestack-averaged results in Figure 8.7b, which clearly show a very noisy current estimate in **XM**Fit.

In conclusion, the complexity of the three-dimensional nearshore processes at the Sand Motor are not being accurately modeled by **XM**Fit since they are being averaged over a relatively large computational cube.

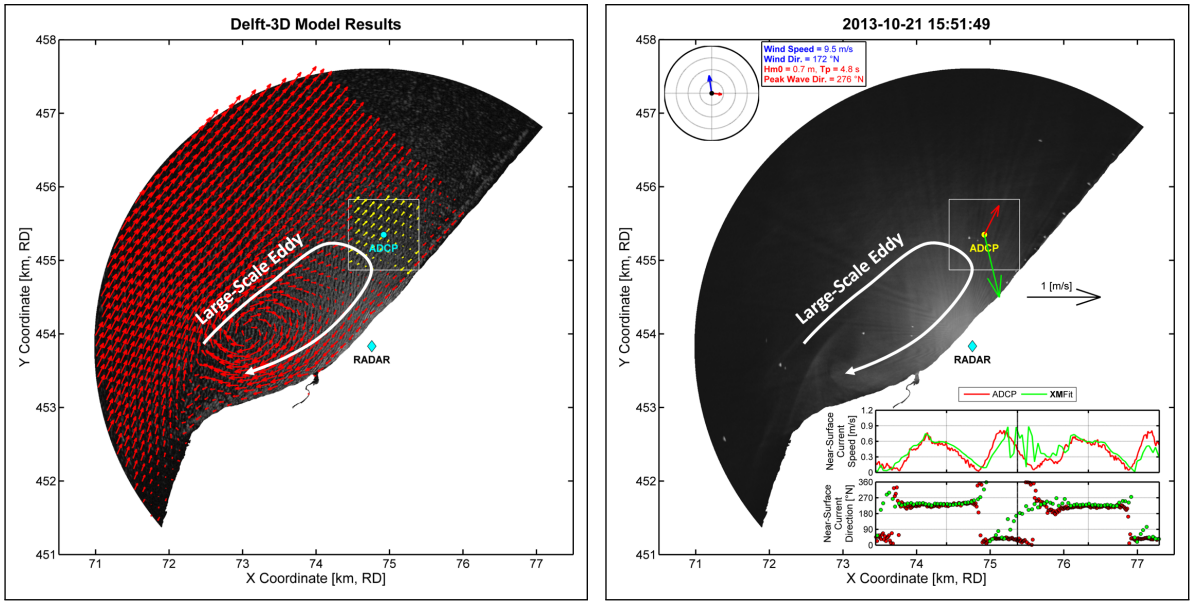

(a) Delft-3D Simulation **(b)** **XM**Fit Results

Figure 8.7: Large-Scale Eddy on the Lee of the Sand Motor

8.3 Potential for Future Research

This discussion identified a spatial cutoff and metocean limits that led to the ideal conditions for **XM**Fit. All the work in this report is focused on the Sand Motor, but it is not clear whether **XM**Fit is applicable at another coastal location.

This section of the discussion highlights the potential for future X-band radar depth inversion work with **XM**Fit. A single timestack from the Ameland inlet shows that an uncalibrated **XM**Fit model is capable of extracting coherent bathymetry and current fields. More information about the Ameland inlet can be found in previous work by Deltares (2011), Swinkels et al. (2012), Deltares (2013) and Rutten (2013). As a proof of concept, **XM**Fit was compared against SeaDarQ at the Ameland inlet, see Figure 8.8.

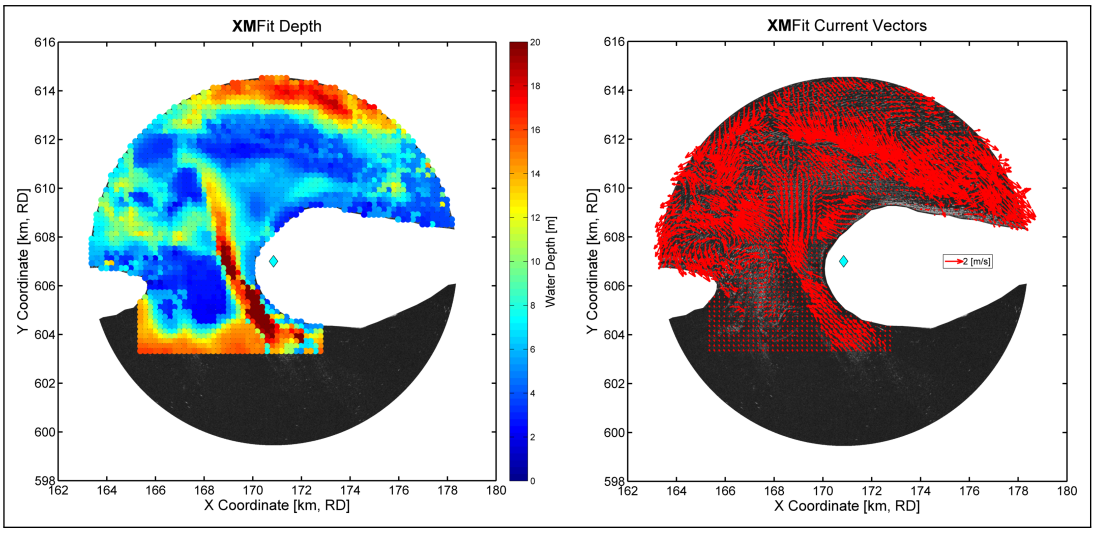

(a) XM Fit

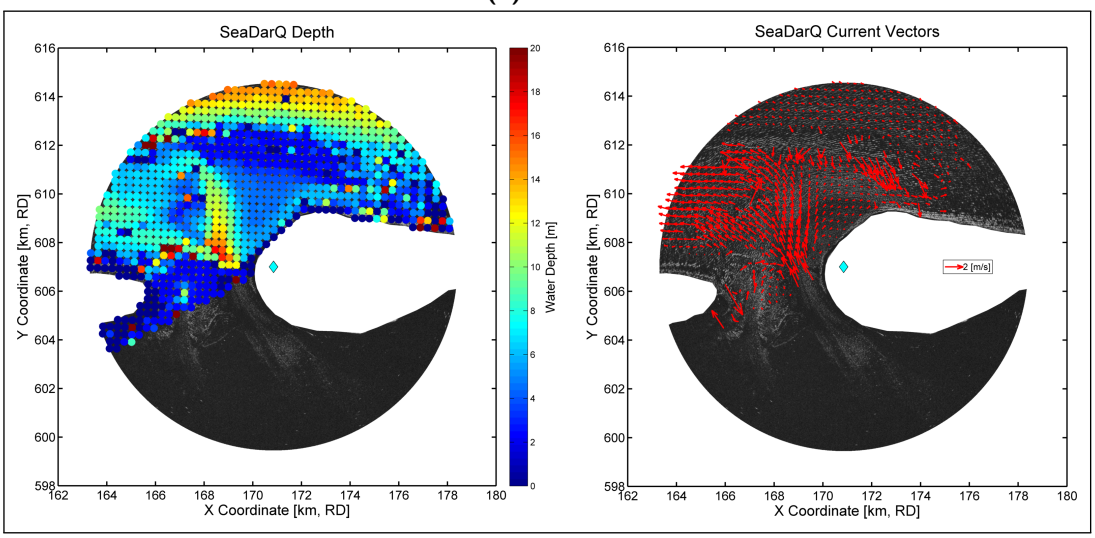

(b) SeaDarQ

Figure 8.8: Proof of Concept at the Ameland Inlet

This exercise is only meant to prove that **XM**Fit is not site-specific and can accurately measure detailed hydrodynamics at the Ameland inlet. This brief investigation at the Ameland inlet does not consider any *in situ* comparisons since previous work concluded that SeaDarQ output adequately represents the inlet after various post-processing techniques. The goal is to visually compare the capabilities of **XM**Fit against SeaDarQ.

Two aspects of Figure 8.8a provide increased confidence in the ability of **XM**Fit. Firstly, the model is able to extract the complex bathymetry such as the westward directed main channel and the ebb-tidal delta shoal. Secondly, **XM**Fit provides current estimates when SeaDarQ produces data gaps or outliers. Swinkels et al. (2012) summarized that poor quality SeaDarQ estimates at Ameland are either due to steep bathymetric gradients, wave breaking and due to range effects. The uncalibrated **XM**Fit at the Ameland inlet does not show any of these effects, which truly confirms its robustness as a model.

Chapter 9

Conclusions

Firstly, it should be made clear that all conclusions are based on a single temporal period from October 21^{st} to November 1^{st}, 2013 and limited to the Sand Motor site. The intended goal of this thesis work is to accurately estimate hydrodynamic parameters from raw X-band radar images with high temporal and spatial resolution. The following conclusions prove the successful completion of this goal.

The **XM**Fit model was developed, calibrated and validated for the storm duration at the Sand Motor. It is an easy to use model with the ability for further research via additional subfunctions. Details of the developed algorithm are explained in Chapter 5. A validation of the depth inversion theory at the deployed ADCP location highlighted the extremely sensitive fitting procedure. Accurate fitting of both depth and currents requires a fine balance between the two parameters, which is on the scale of individual pixels. The validation concluded by showing that the theory in **XM**Fit overestimates depth even with the known *in situ* current vector. The consistent linear bias can be potentially linked to the radar installation.

XMFit proved to be a valuable remote sensing tool for extracting nearshore hydrodynamics based on *in situ* comparisons (detailed in Chapter 7). The radar-derived hydrodynamics from **XM**Fit are typically overestimating depth throughout the entire radar domain, as witnessed by the validation work in Chapter 6. The positive bias associated with the water depth does not influence the current estimates. An inaccurate comparison is recognized between the **XM**Fit currents and the ADCP during flood tide. The storm results in Chapter 7 show that **XM**Fit is more robust than SeaDarQ. This improvement is attributed to the Global Aliasing Analysis and the 3D Non-Linear Depth Inversion explained in Chapter 5. The SeaDarQ software produced inaccurate results during this storm since it is not able to distinguish any sort of bathymetric gradient at the Sand Motor.

A sensitivity analysis was completed in Chapter 8 to further analyze the spatial and temporal patterns associated with **XM**Fit accuracy. The spatial statistics indicated high error around the edges of the radar domain, which led to a reduced radar footprint by implementing a spatial cutoff of 2.5 km. The reduced area results in much less scatter with a near-constant linear bias of 2 m. Temporal statistics indicated trends in the statistical fit between **XM**Fit

and the *in situ* data. The following metocean limits are found to be associated with periods of high accuracy in **XM**Fit.

- Significant wave height greater than **1 m**
- Wind speed should be greater than **12 m/s**
- Wind and waves should align within **45**°

The metocean limits help conclude that **XM**Fit requires spectra spreading in $k - \omega$ space to help *constrain* the dispersion shell. This finding directly links with locally generated wind waves, more commonly referred to as *wind sea*. *Ideal* results based on the spatial and temporal limits further reduced the linear bias to approximately 1.6 m. The ideal conditions show a much better agreement between radar-derived and *in situ* bathymetry and hydrodynamics.

A brief investigation into the inaccuracy of **XM**Fit during flood tide was also completed in Chapter 8. The main finding is that **XM**Fit is essentially averaging the complex 3D flow structures evident during flood tide into a single large computational cube, which drastically simplifies the underlying flow patterns. More work into understanding the physical meaning of the **XM**Fit current estimate is required, along with more knowledge of the 3D flow structures around the Sand Motor.

Finally, this work concludes by analyzing a single timestack at a different coastal site along the Dutch coast to prove the applicability of the **XM**Fit model. The instantaneous results are able to extract the complex ebb-tidal delta, the proper orientation of the main flood channel and wave-induced currents on the outer ebb-tidal delta shoal. This work proves the value of **XM**Fit as a remote sensing model in a very complex environment.

Chapter 10

Recommendations

The work presented herein detailed the development, validation, calibration and resulting output of **XM**Fit during the storm of October 21^{st} to November 1^{st}, 2013. The newly developed **XM**Fit model was compared against SeaDarQ, a commercial product sold by Nortek, and proved to be superior for both depth and current estimation. **XM**Fit was also adapted for use at the Ameland inlet, which showed promising results. The following recommendations are suggested to improve the **XM**Fit model in hopes of building an even more robust depth inversion model.

- Apply **XM**Fit at another coastal site
  - Identify if the accuracy issues that influence **XM**Fit accuracy at the Sand Motor are present at a different coastal location (i.e. the Ameland inlet).
- Identify how radar setup affects **XM**Fit accuracy
  - Compare the accuracy at the Sand Motor to the Ameland site since their antenna heights differ (i.e. 15 m vs. 55 m).
- Resolve the complex flow patterns around the Sand Motor
  - Test how to accurately use smaller cube sizes.
- Understand why **XM**Fit overestimates depth at the Sand Motor
  - Investigate the constant positive linear bias evident in all **XM**Fit results by looking at higher resolution radar images. The goal is to have more information in a smaller computational cube, which is possible by interpolating the polar radar images to a more refined cartesian grid.
- Study the role of stratification in **XM**Fit at the Sand Motor
  - Further analyze the influence of stratification using either a 3D numerical model or a deployed CTD (conductivity, temperature and depth) instrument.

- Implement radar-derived wave height estimates in **XM**Fit
  - Determine the appropriate empirical transfer function using the deployed wave buoy at the Sand Motor. The approach detailed by Nieto Borge et al. (2004) explains how to transform image spectra to wave spectra.
- Fix the edge and land boundary effects in **XM**Fit
  - Improve the *blanking* of land through the 3D FFT of the timestack. This can potentially be done by transforming the raw radar images to a horizontal coastline.
- Adaptively select the non-linear fitting method
  - Allow **XM**Fit to select which form of the linear dispersion relation is most suitable for the analyzed timestack (i.e. slack tide). Use the intrinsic dispersion relation if the estimated $\vec{U} \approx 0$, which improves depth accuracy and computational time.
- Build an assimilated model using **XM**Fit
  - Include measured *in situ* data that can potentially select the most appropriate minimum energy cutoff for fitting the linear dispersion shell (see Chapter 5.2.4).
- Further research non-linear wave physics in **XM**Fit
  - Test the results by Flampouris et al. (2011) by implementing the non-linear wave theories of Hedges and Cnoidal.
- Build an empirical linear dispersion relation in **XM**Fit
  - Try "reverse engineering" the non-linear fitting procedure with known $d, \vec{U}$ to find a suitable empirical relation. This could potentially add a new term or factor to the doppler-shifted linear dispersion relation.
- Develop a Graphical User Interface (GUI) for **XM**Fit
  - A GUI is beneficial to (potential) end users since it will require less skill to use while making it easier to understand the necessary input parameters.

Appendix A

XMFit Spatial Calibration

This appendix explains the methodology followed for spatially calibrating the **XM**Fit model at the Sand Motor. It consists of the global procedure, followed by the approach for each gridpoint in order to generate *ideal* spatial settings. The final product of this appendix is using the *ideal* settings to find a more coherent general spatial settings.

A.1 Global Procedure

Table 5.1 presented in Chapter 5.2.1 indicated various computational cube sizes. It is unfortunately unclear what cube should be used at what location within the radar grid. This led to the idea of spatially calibrating **XM**Fit in hopes of achieving the most accurate results.

Each of the computational cube settings are all tested with one another, forming all combinations of N_i and N_ω. This resulted in 9 different settings for **XM**Fit, which were run at various times throughout a single tide to ensure the calibration was not only valid for a specific point in time. The low water slack, maximum flood current, high water slack and maximum ebb current were analyzed for each run. Figure A.1 shows all of the analyzed spatial calibration runs.

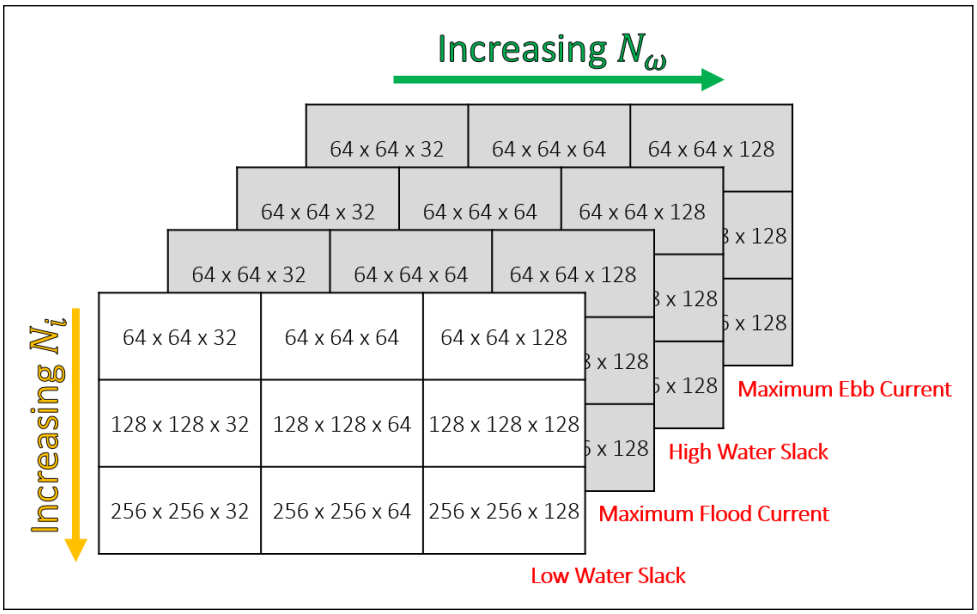

Figure A.1: **XM**Fit Calibration Runs

A.2 Gridpoint Procedure

The end goal of the calibration is to find the most suitable spatial setting for each gridpoint. Note that the N_i and N_ω settings by gridpoint are independent, allowing for a spatially independent analysis. The gridpoint procedure involved finding the minimum error between the **XM**Fit estimated water depth and the *in situ* water depth. A conceptual diagram is presented in Figure A.2.

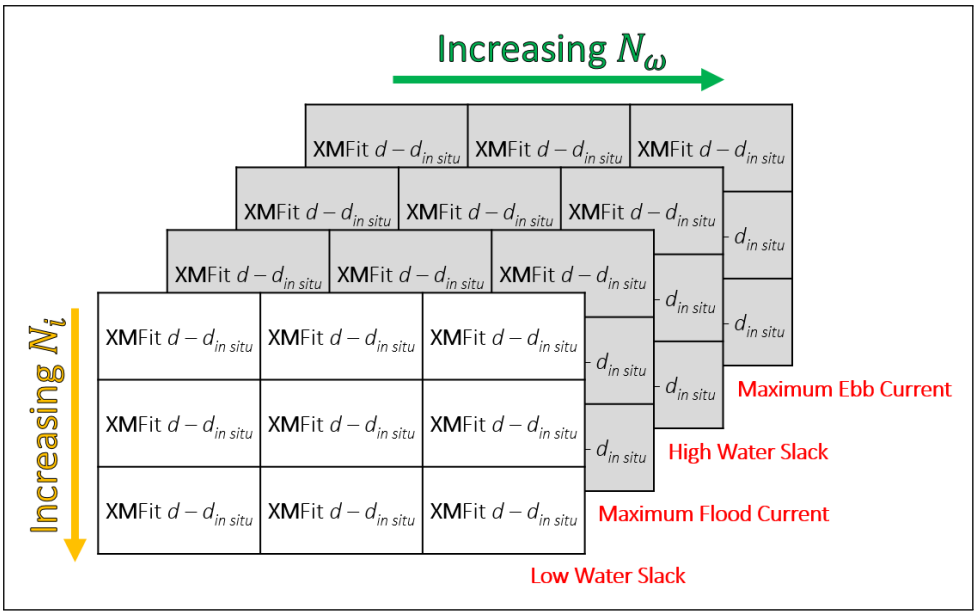

Figure A.2: Global Spatial Calibration Procedure

An example of the gridpoint procedure is shown for a single gridpoint in Figure A.3. The four times analyzed during a single tide are shown on the left in 3 x 3 squares. The square represents the combination of the settings presented in Figure A.1. The colour represents the difference between the **XM**Fit model and the *in situ* data. Most boxes are coloured red since **XM**Fit is consistently overestimating depth. The average difference between **XM**Fit and *in situ* data for the different analyzed times are shown in the temporal period 3 x 3 square. The *ideal* setting (yellow box) is found from the minimum average temporal difference.

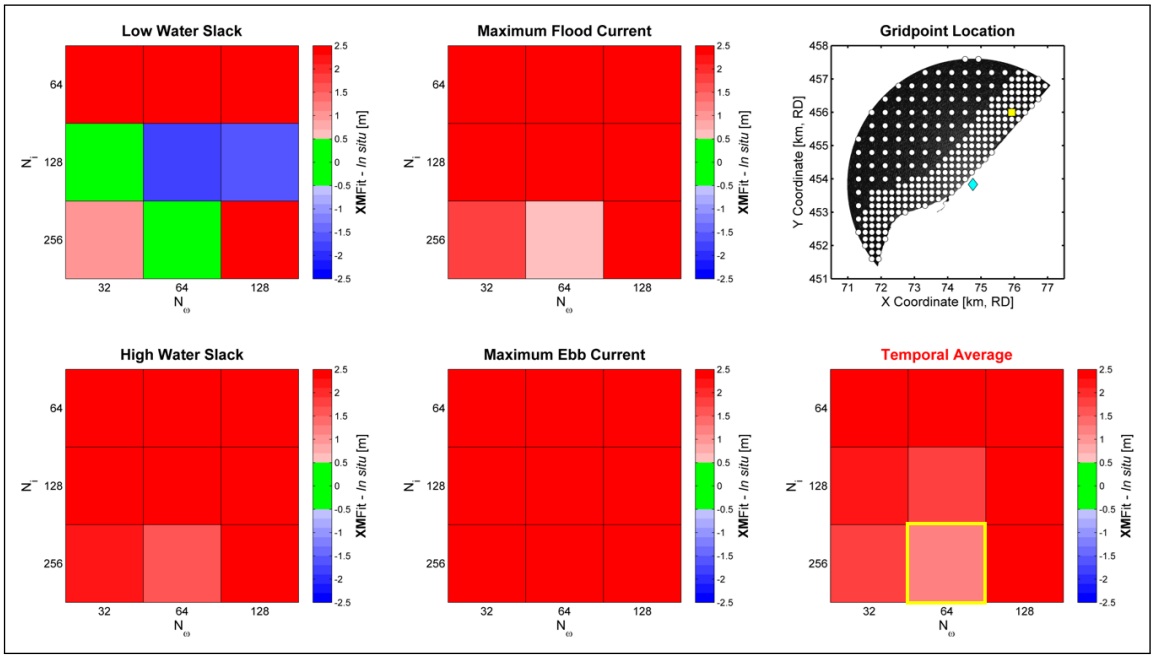

Figure A.3: Shallow Gridpoint Result

The most accurate settings were determined for each gridpoint and compiled as *ideal* settings for the **XM**Fit model at the Sand Motor. The most *ideal* spatial settings of N_i and N_ω at each gridpoint are shown in Figure A.4.

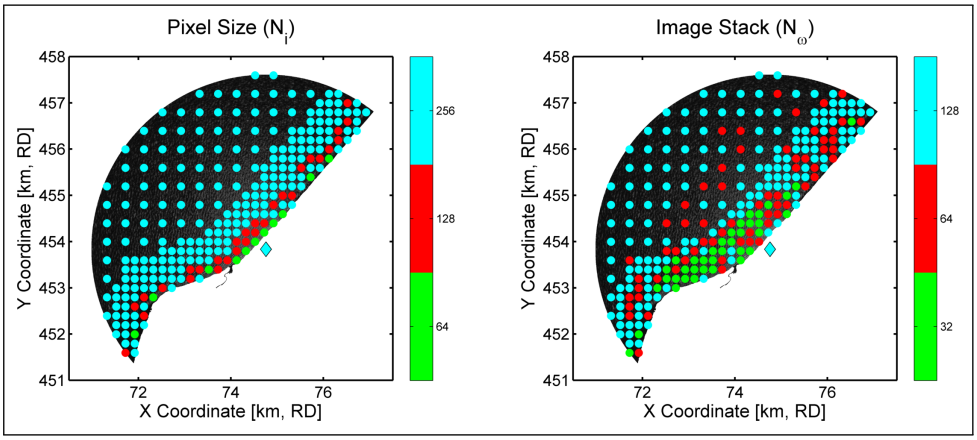

Figure A.4: *Ideal* Spatial Settings

Several trends are noticed in the resulting spatial settings. The cube settings (N_i) show that the majority of the grid works best with a pixel size of 256 (i.e. approximately 960 m). The *ideal* settings also show that smaller cubes work best in the nearshore. The image stack parameter (N_ω) is spatially scattered with the majority of the gridpoints using 128 images (i.e. approximately 6 minutes). The results shown here are simply the best settings with respect to minimizing the temporal average, but are not robust or defensible since they are too scattered. Therefore, the 2^{nd}, 3^{rd}, ..., n^{th} best *ideal* spatial calibration settings could help define a more coherent spatial pattern.

A.3 Building General Spatial Settings

As shown and mentioned, the spatial calibration resulted in a scattered set of ideal settings which show a very weak spatial trend. This led to the concept of building a general spatial pattern to identify spatial patterns in the computational cube settings. A visual inspection of the top spatial settings were sensitive to nearshore and edge effects. Thus, spatial zones were discretized within the radar footprint as shown by Figure A.5.

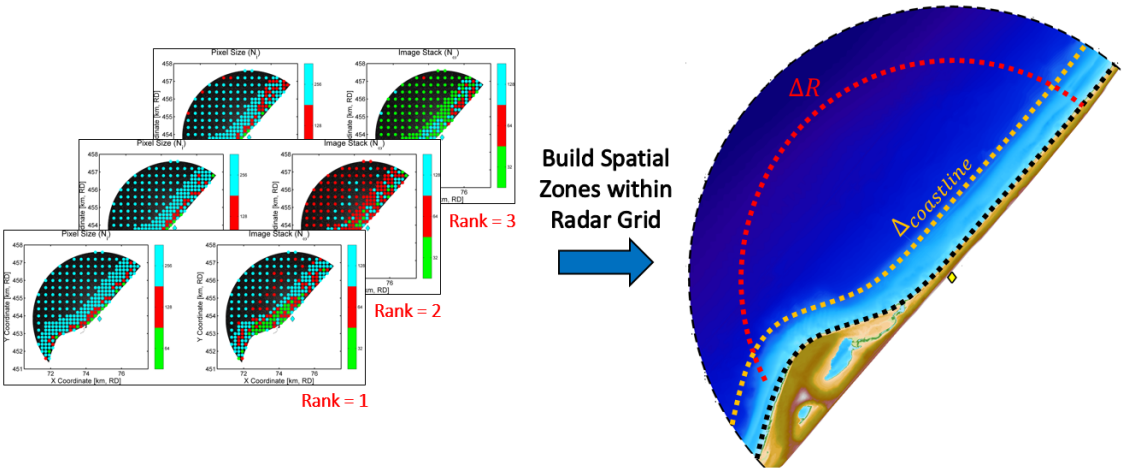

Figure A.5: *Generalized* Spatial Pattern Idea

An algorithm was developed to analyze all possible combinations of settings in each discretized zone. Each zone was also varied in size in order to find the optimal spatially varying settings. This resulted in thousands of combinations, which were ranked based on the lowest RMSE between **XM**Fit and the *in situ* data. The end result of this analysis is shown in Figure A.6. Note that all work presented in this thesis at the Sand Motor uses the generalized spatial settings.

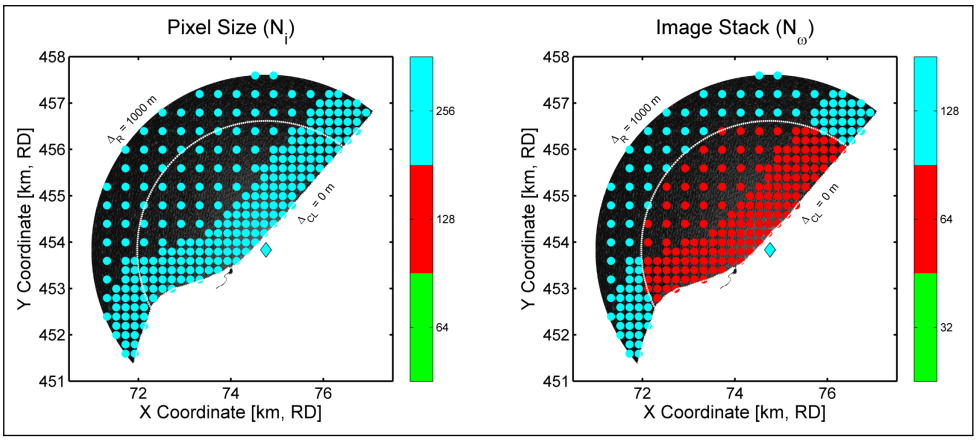

Figure A.6: *Generalized* Spatial Settings

Appendix B

Testing Non-Linear Wave Theory

Research by Grilli (1998), Catálan and Haller (2008), Flampouris (2010) and Flampouris et al. (2011) all suggest including non-linear wave theory in the depth inversion algorithm to improve accuracy. The main reason for its inclusion is to better resolve non-linear wave effects that govern wave propagation in relatively shallow water. The linear wave theory is technically not valid in such shallow water, thus non-linear wave theory should better represent shallow water depth processes. The work in this Appendix presents a brief investigation into the inclusion of non-linear wave theory in **XM**Fit in hopes of better resolving shallow water depth estimates.

B.1 Third-order Stokes Correction

The third-order Stokes correction for amplitude dispersion presented in Chawla and Kirby (2002) is used in this analysis. An additional fitting method was included in **XM**Fit to test the third-order Stokes correction. Prior to visualizing results, its influence on the linear dispersion relation is studied. The presence of waves results in an additional amplitude dispersion, altering the dispersion shell as a function of amplitude (see Equation B.1).

$$\omega = \sqrt{gk \tanh(kd) \left[1 + (ka)^2 \left(\frac{8 + \cosh(4kd) - 2\tanh^2(kd)}{8\sinh^4(kd)}\right)\right]} + k \cdot \vec{U} \tag{B.1}$$

The influence of the Stokes correction is tested at various water depths and for various wave heights to understand its effect. Figure B.1 shows the difference between the linear theory (black shell) and the Stokes correction (red shell) for a 1 m wave height. The analyzed depths range from 2.5 m to 12.5 m. The identical frequency level contour for each shell (and for each water depth) was extracted for a peak period of 5 s. This contour was extracted since it aligns with the average metocean climate at the Sand Motor (see Figure 4.5). The influence of a 1 m wave height is quite insignificant on the linear dispersion shell except in extremely

shallow water depth. As expected, the third-order Stokes correction is negligible in deeper water.

The same approach is shown in Figure B.2 but with a wave height of 2 m. The Stokes correction is more pronounced with a higher wave height, which is evident from Equation B.1. The amplitude dispersion tends to shrink that linear dispersion shell by shifting it to a higher frequency level. Note that the first water depth of 2.5 m with a 2 m wave height is quite unrealistic since it is well over the breaker depth limit.

The third-order Stokes correction presented by Chawla and Kirby (2002) is most important in shallow water depths but insignificant in deeper water. The slight difference with the linear dispersion relation follows the work by Flampouris et al. (2011), which found that the signal processing is more influential than the depth inversion physics.

B.2 Influence on XMFit Results

The previous section indicated the relative insensitivity of the Stokes correction in deep water, but it was still tested for all water depths in **XM**Fit. Three different wave heights were investigated - 0.75 m, 1.25 m, and 2.50 m. Both the linear dispersion relation and the non-linear Stokes correction are included for comparison. The results are contained in this section.

This work shows that the third-order Stokes correction for amplitude dispersion is statistically worse than the linear wave theory for various wave heights. The consistent positive bias evident in **XM**Fit is not corrected with non-linear physics. It is also noted that the non-linear wave physics tends to estimate a constant minimum water depth in shallow water due to the shape of the shell in unrealistic conditions (see Figure B.8).

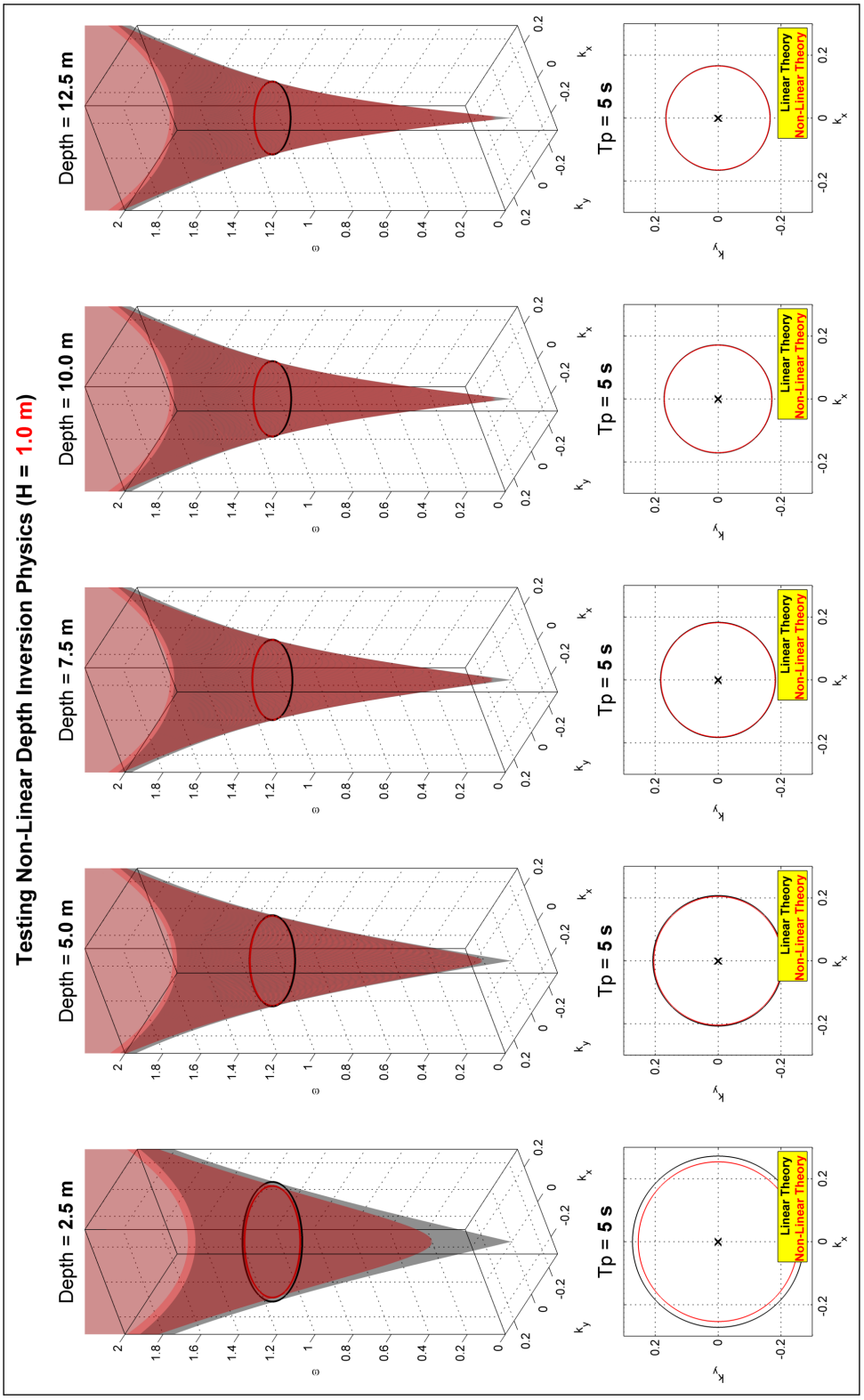

Figure B.1: Visualizing the Non-Linear Dispersion Relation for Hm0 = 1.0 m

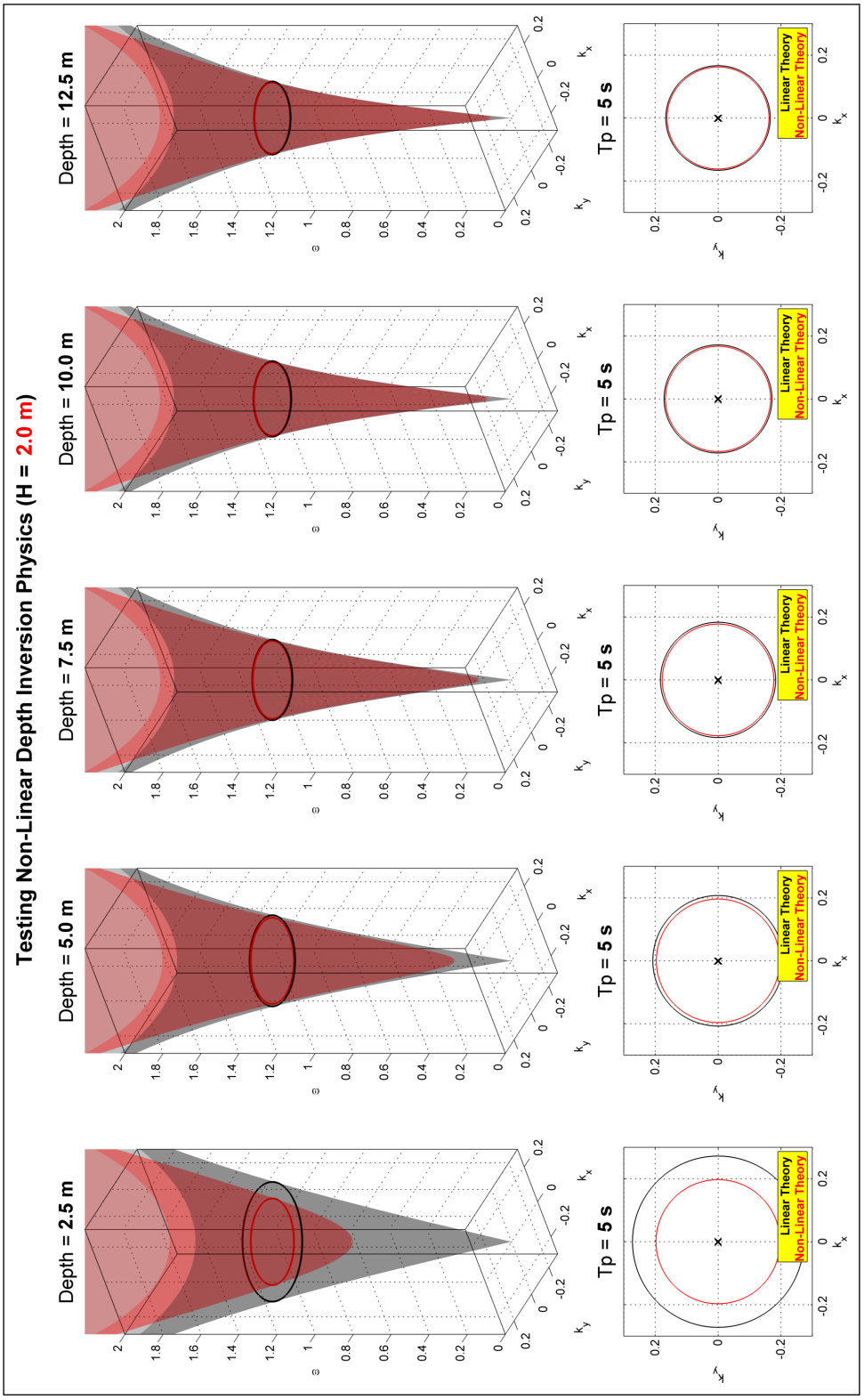

Figure B.2: Visualizing the Non-Linear Dispersion Relation for Hm0 = 2.0 m

Significant Wave Height = 0.75 m

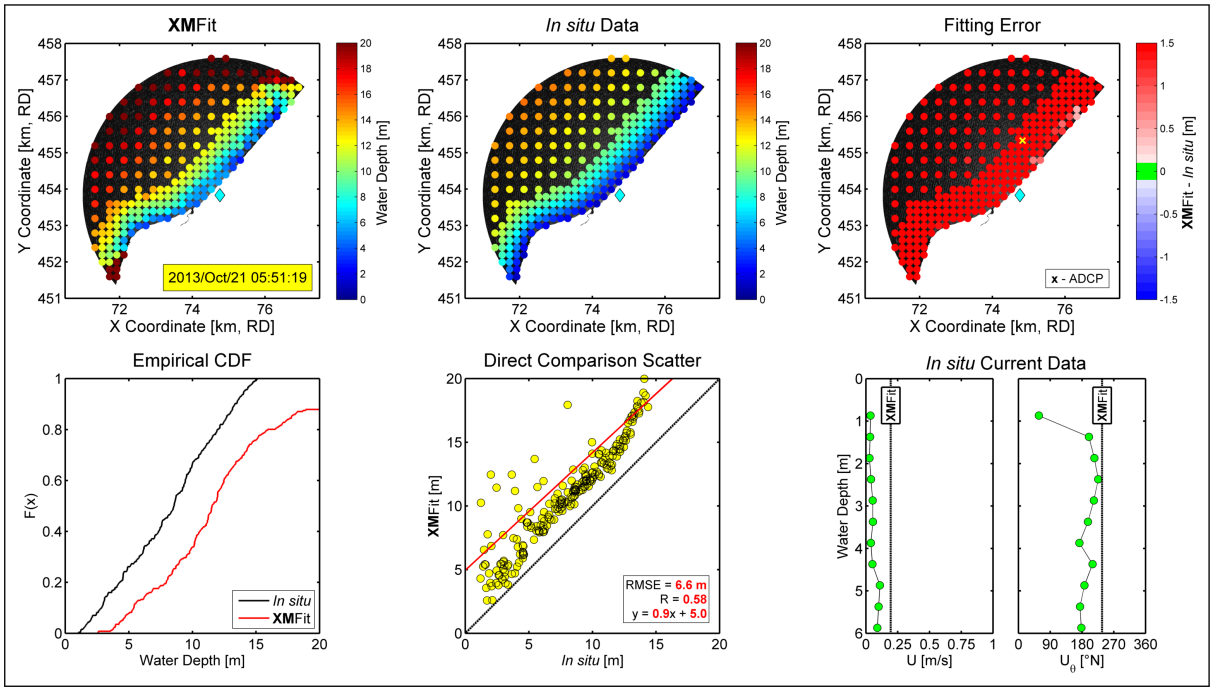

Figure B.3: XMFit Results with **Linear Wave Theory** (Hm0 = 0.75 m)

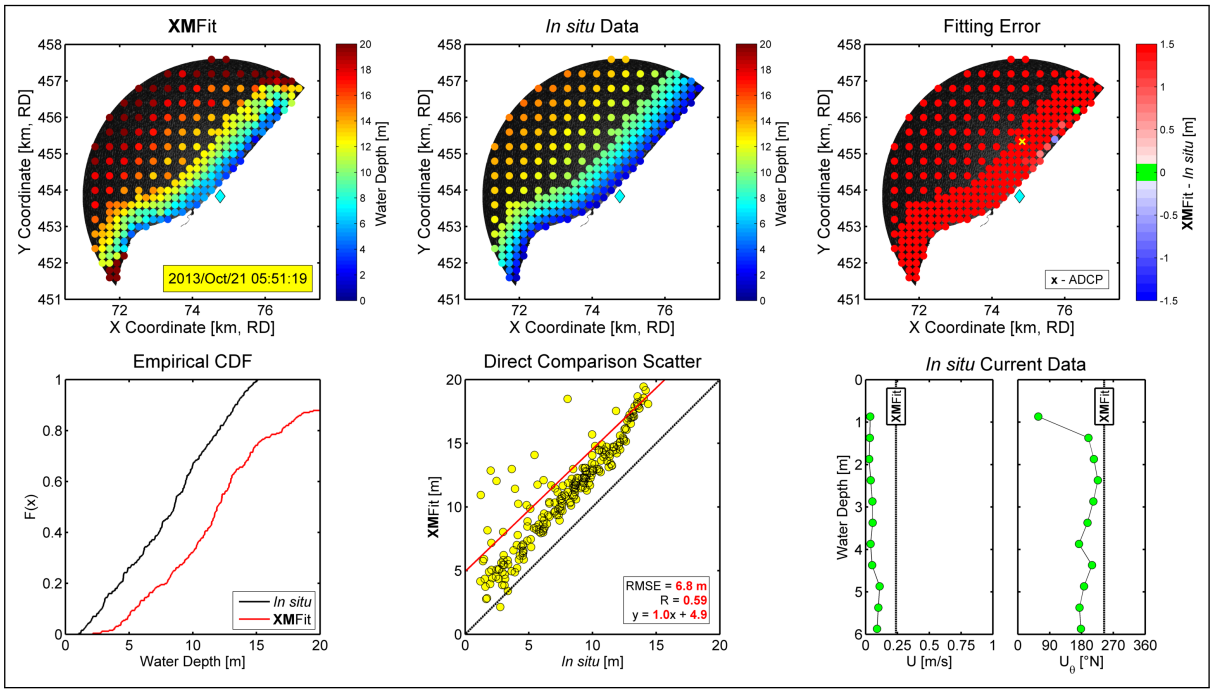

Figure B.4: XMFit Results with the **Non-Linear Stokes Correction** (Hm0 = 0.75 m)

Significant Wave Height = 1.25 m

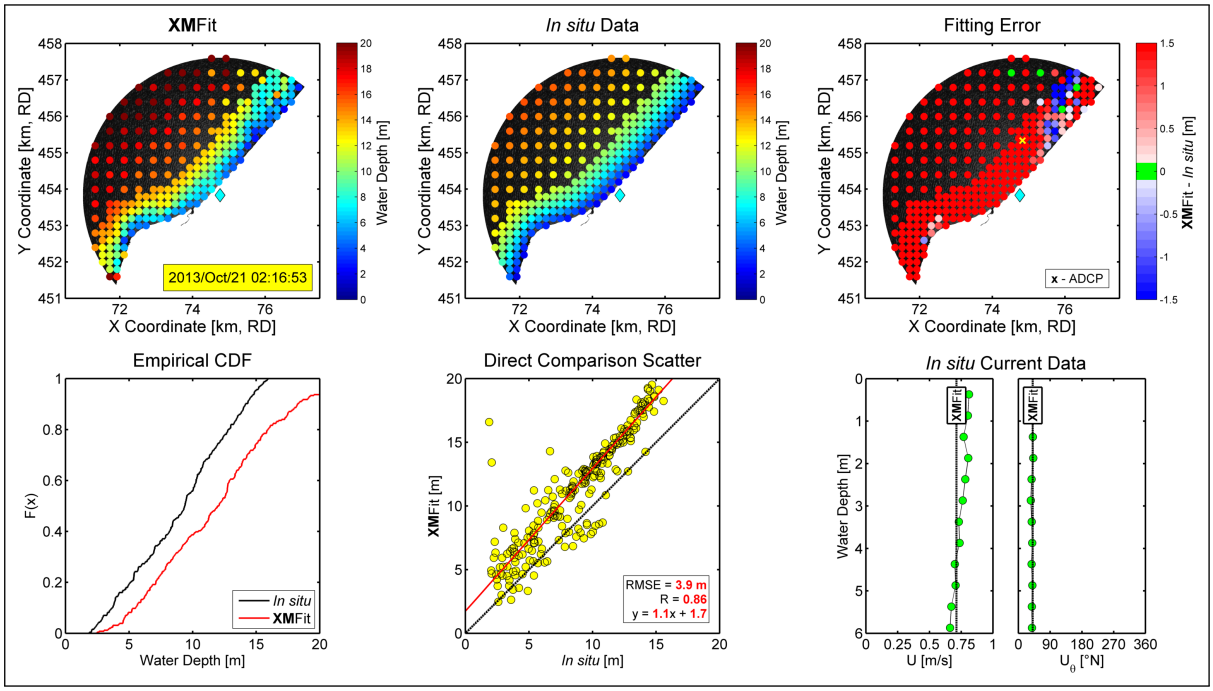

Figure B.5: XMFit Results with **Linear Wave Theory** (Hm0 = 1.25 m)

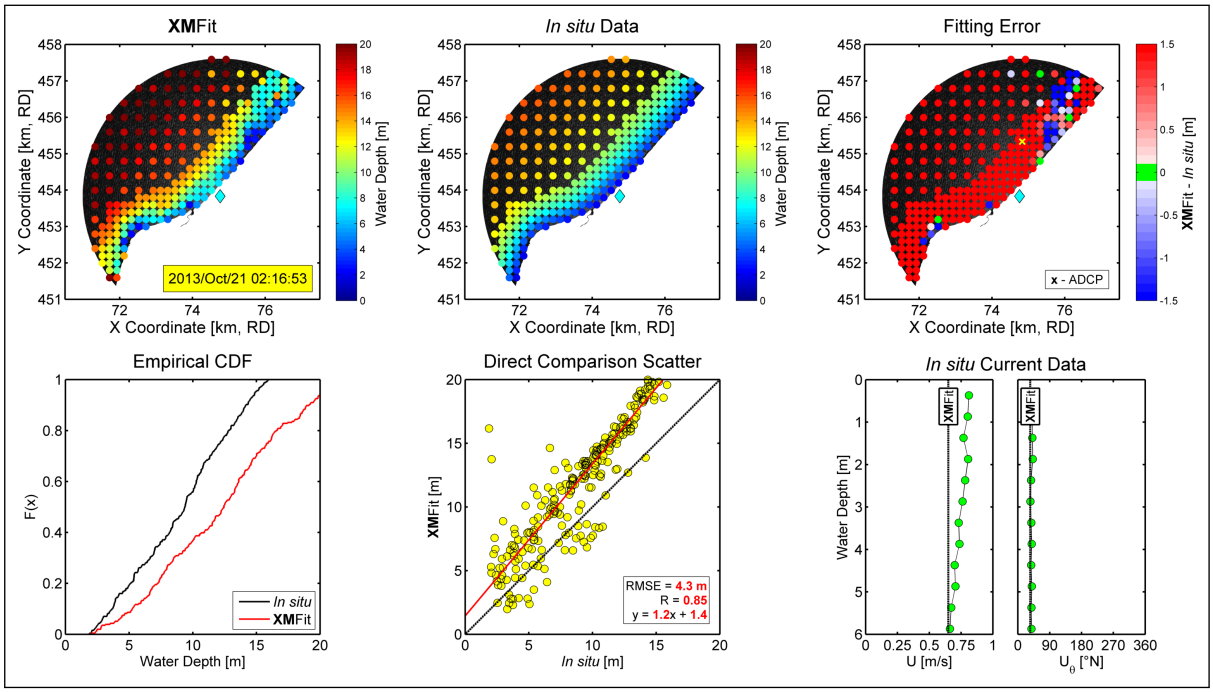

Figure B.6: XMFit Results with the **Non-Linear Stokes Correction** (Hm0 = 1.25 m)

Significant Wave Height = 2.50 m

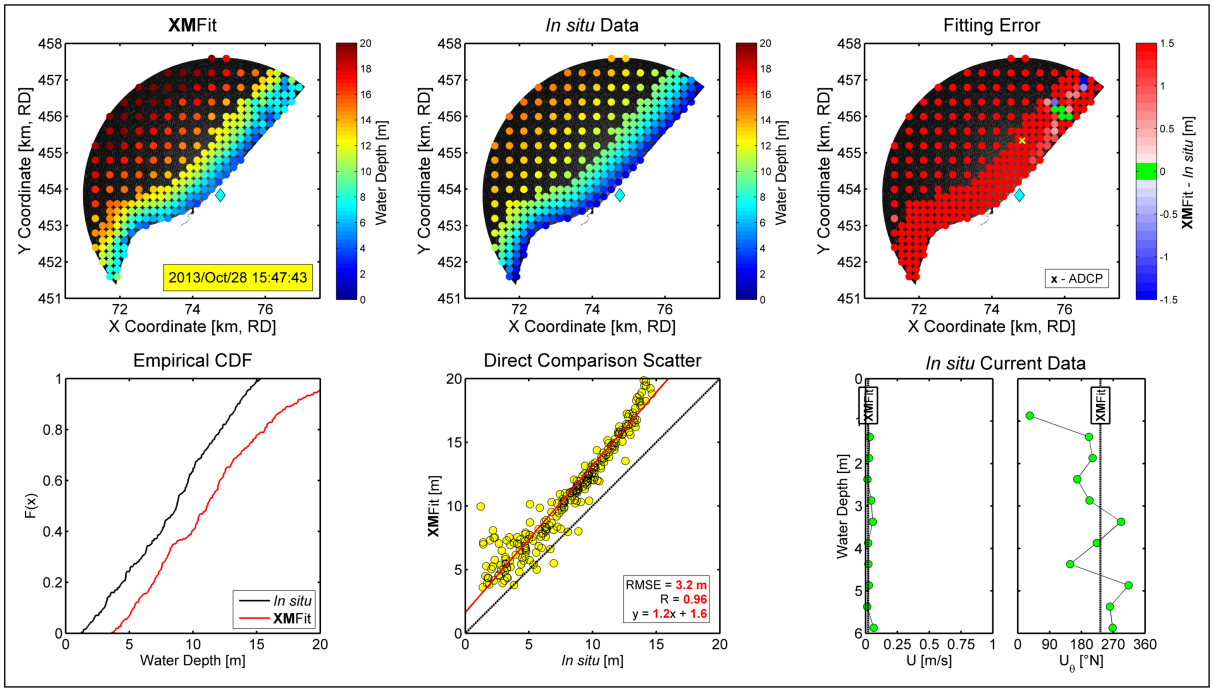

Figure B.7: XMFit Results with **Linear Wave Theory** (Hm0 = 2.50 m)

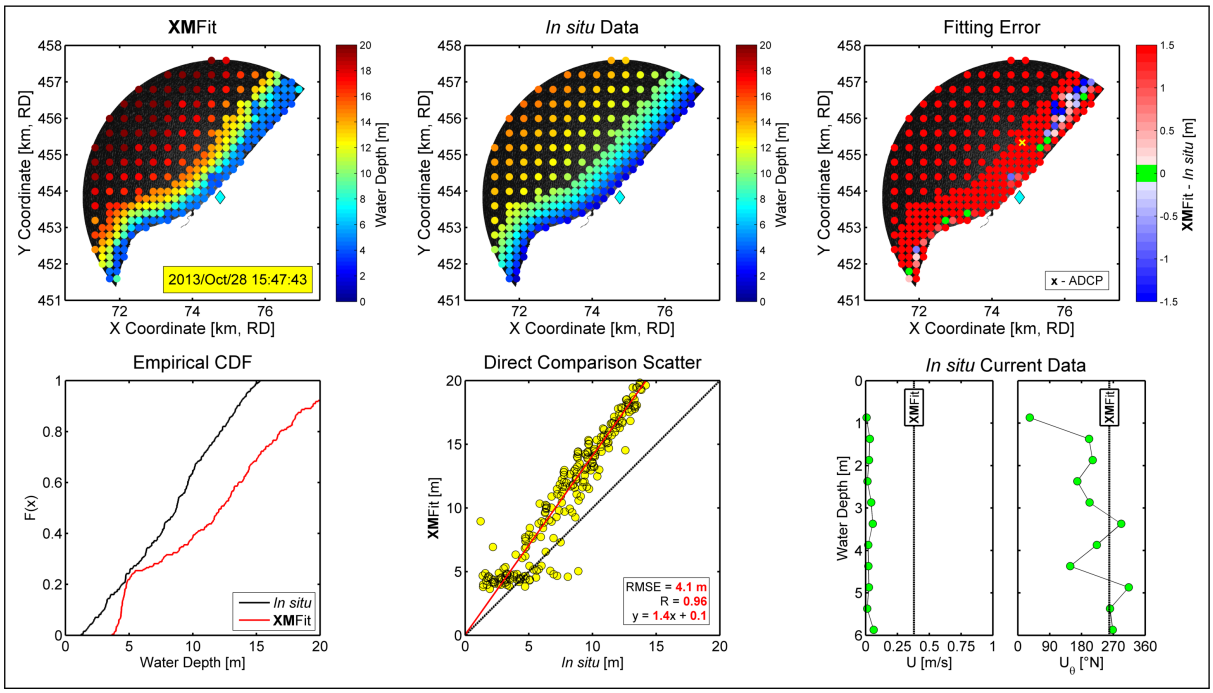

Figure B.8: XMFit Results with the **Non-Linear Stokes Correction** (Hm0 = 2.50 m)

Appendix C

Single Timestep Comparison

C.1 Bathymetric and Hydrodynamic Output

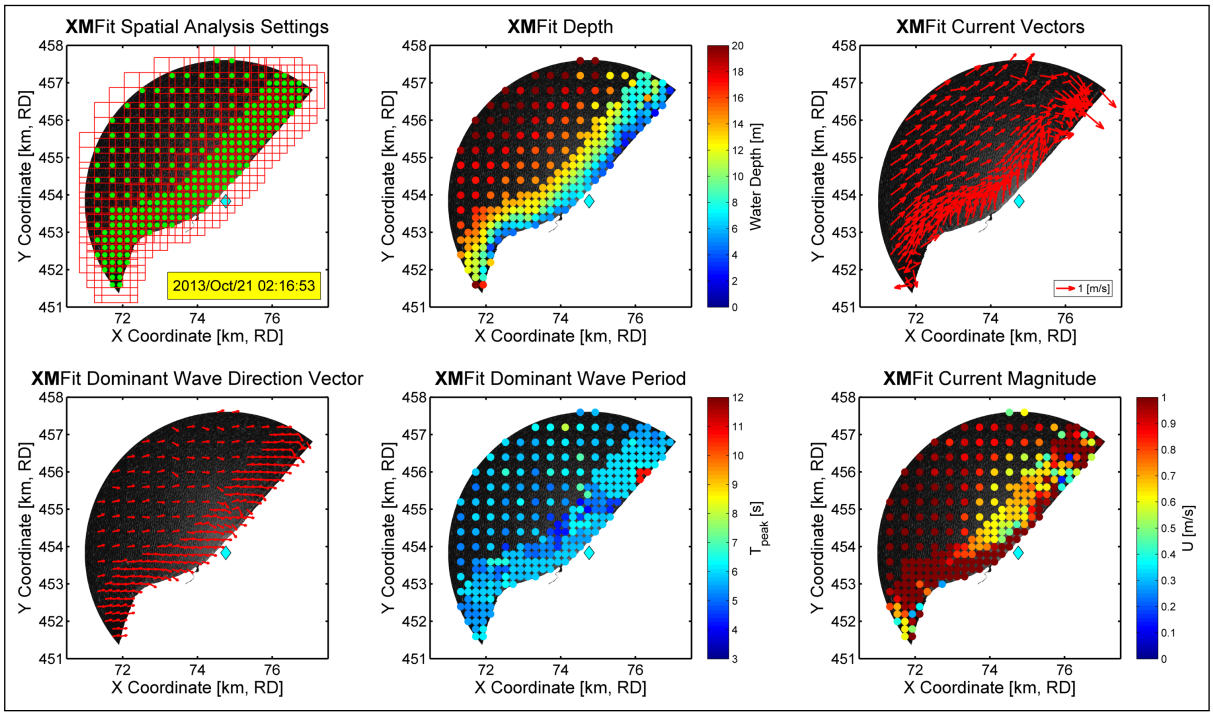

Figure C.1: XM Fit Model Results (2013/10/21 02:16:53)

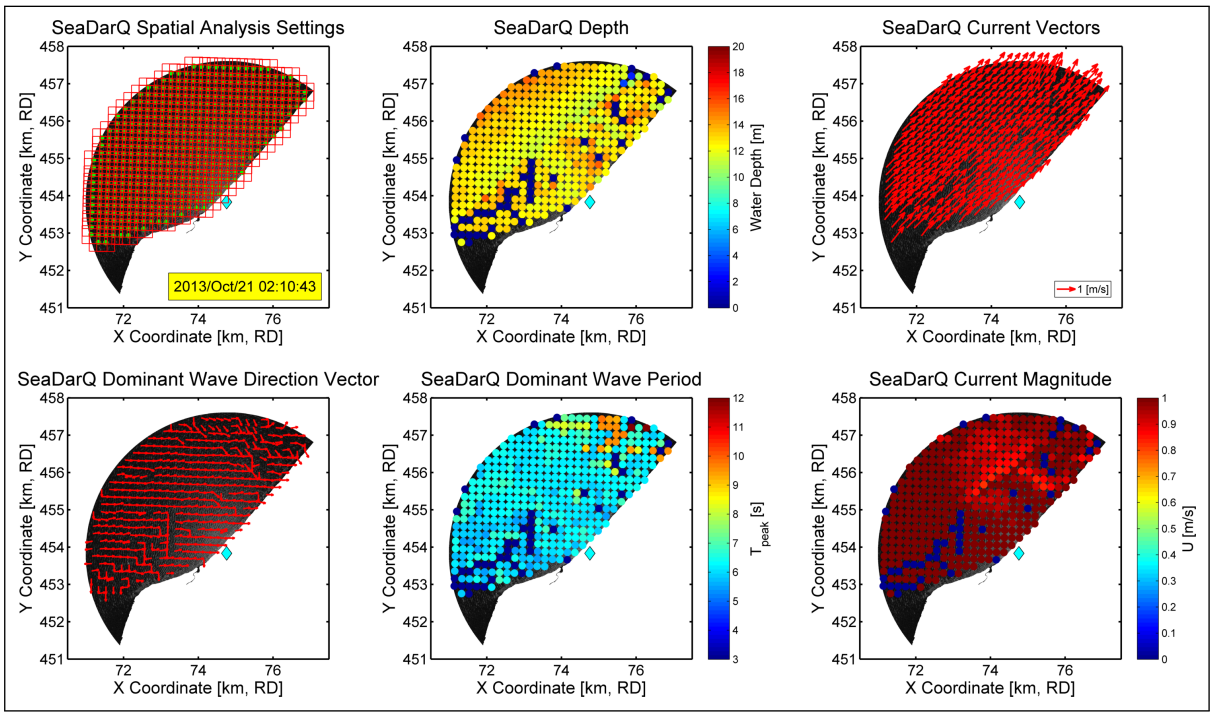

Figure C.2: SeaDarQ Model Results (2013/10/21 02:10:43)

C.2 *In situ* Comparison

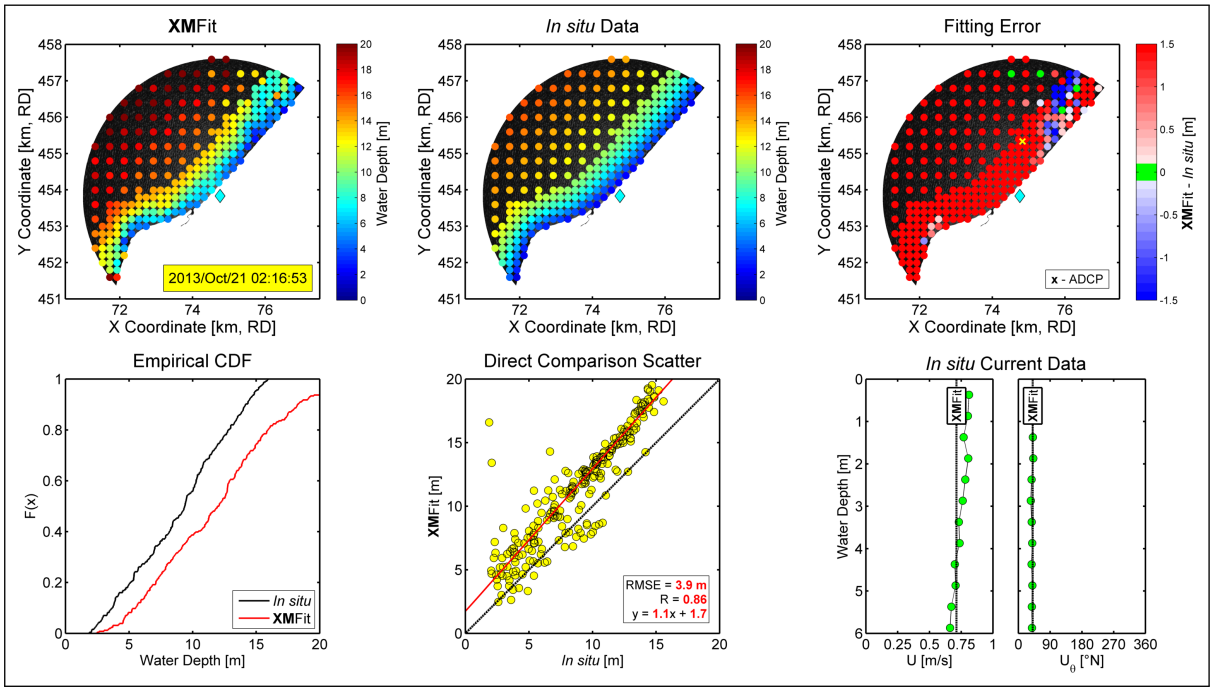

Figure C.3: **XM**Fit *in situ* Comparison (2013/10/21 02:16:53)

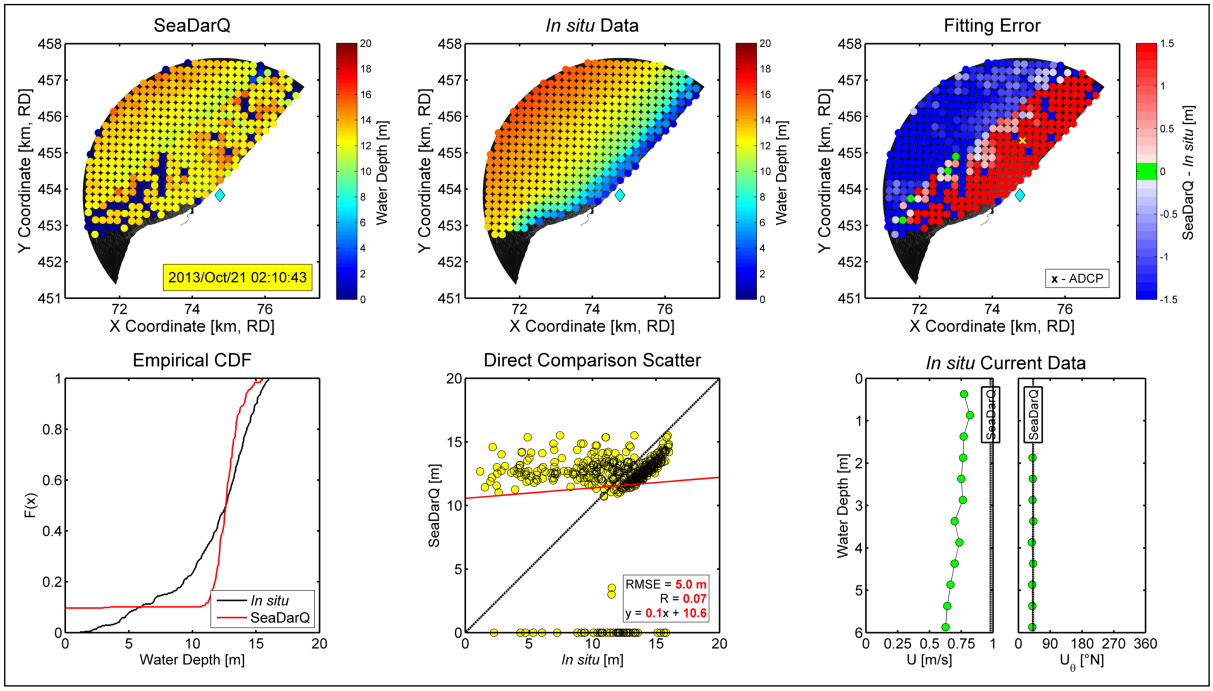

Figure C.4: SeaDarQ *in situ* Comparison (2013/10/21 02:10:43)

C.3 Extracted Profile Comparison

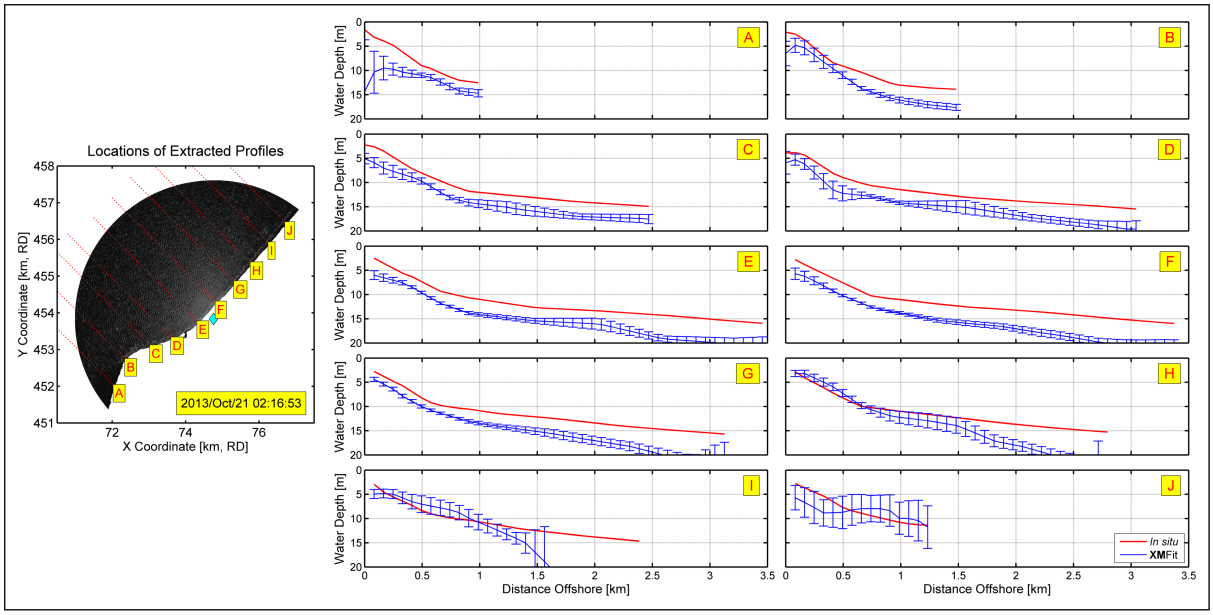

Figure C.5: **XM**Fit Extracted Profiles (2013/10/21 02:16:53)

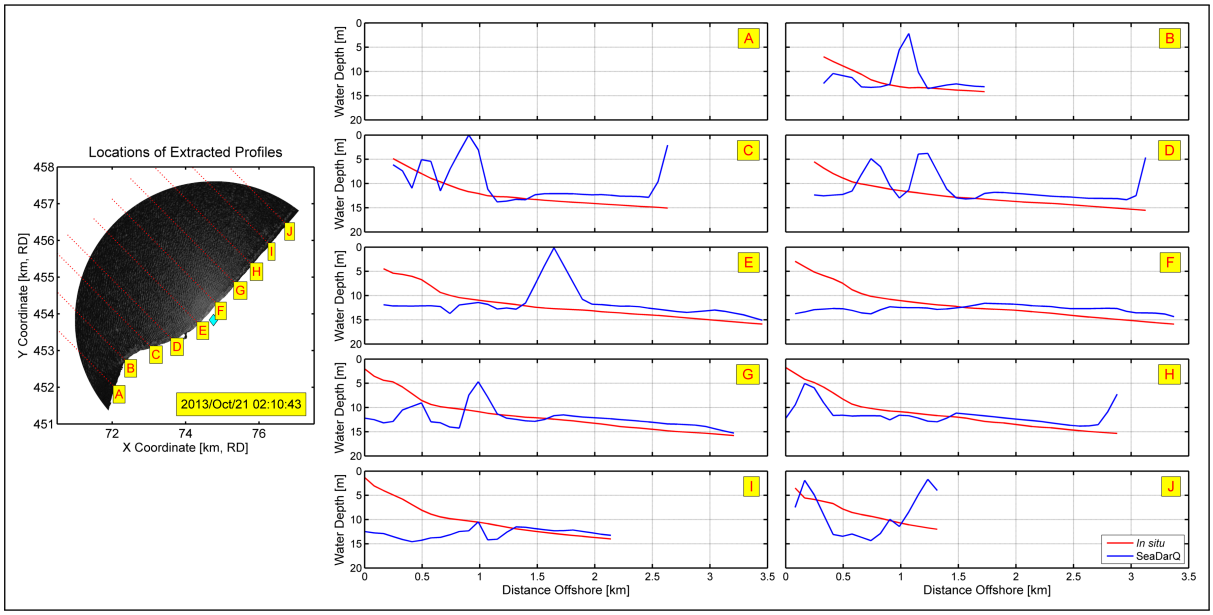

Figure C.6: SeaDarQ Extracted Profiles (2013/10/21 02:10:43)

References

Alpers, W., Ross, D., and Rufenach, C. (1981). On the Detectability of Ocean Surface Waves by Real and Synthetic Aperture Radar. *Journal of Geophysical Research: Oceans (1978–2012)*, 86(C7):6481–6498.

Bell, P. (1999). Shallow Water Bathymetry Derived From an Analysis of X-band Marine Radar Images of Waves. *Coastal Engineering*, 37(3):513–527.

Bell, P. (2008). Mapping Shallow Water Coastal Areas Using a Standard Marine X-band Radar. *Proceedings of Hydro8 Conference*.

Catálan, P. and Haller, M. (2008). Remote Sensing of Breaking Wave Phase Speeds with Application to Non-linear Depth Inversions. *Coastal Engineering*, 55(1):93–111.

Chawla, A. and Kirby, J. T. (2002). Monochromatic and Random Wave Breaking at Blocking Points. *Journal of Geophysical Research: Oceans (1978–2012)*, 107(C7):4–1.

Dankert, H., Horstmann, J., Lehner, S., and Rosenthal, W. (2003a). Detection of Wave Groups in SAR Images and Radar Image Sequences. *Geoscience and Remote Sensing*, 41(6):1437–1446.

Dankert, H., Horstmann, J., and Rosenthal, W. (2003b). Ocean Wind Fields Retrieved from Radar-Image Sequences. *Journal of Geophysical Research: Oceans (1978–2012)*, 108(C11).

Deltares (2011). Storm Hindcast January 2010.

Deltares (2013). Hydrodynamic Modelling of Storm Events.

Deltares and Imares (2012). Uitvoeringsprogramma Monitoring en Evaluatie Pilot Zandmotor.

Flampouris, S. (2010). *On the Wave Field Propagating Over an Uneven Sea Bottom Observed by Ground Based Radar*. PhD thesis, GKSS-Forschungszentrum Geesthacht GmbH, Bibliothek/Library.

Flampouris, S., Seemann, J., Senet, C., and Ziemer, F. (2011). The Influence of the Inverted Sea Wave Theories on the Derivation of Coastal Bathymetry. *Geoscience and Remote Sensing Letters, IEEE*, 8(3):436–440.

Grilli, S. (1998). Depth Inversion in Shallow Water Based on Nonlinear Properties of Shoaling Periodic Waves. *Coastal Engineering*, 35(3):185–209.

Hessner, K. and Bell, P. S. (2009). High Resolution Current & Bathymetry Determined by Nautical X-band Radar in Shallow Waters. In *OCEANS 2009-EUROPE*, pages 1–5. IEEE.

Holman, R. and Haller, M. (2013). Remote Sensing of the Nearshore. *Annual Review of Marine Science*, 5:95–113.

Holthuijsen, L. H. (2007). *Waves in Oceanic and Coastal Waters*. Cambridge University Press.

MATLAB (2013). Version 8.1 (r2013a).

McNinch, J. (2007). Bar and Swash Imaging Radar (BASIR): A Mobile X-band Radar Designed for Mapping Nearshore Sand Bars and Swash-defined Shorelines over Large Distances. *Journal of Coastal Research*, pages 59–74.

Mosterdijk, G. and Miller, H. (2008). SeaDarQ Validation Report.

Nieto Borge, J., Rodríguez, G., Hessner, K., and González, P. (2004). Inversion of Marine Radar Images for Surface Wave Analysis. *Journal of Atmospheric and Oceanic Technology*, 21(8):1291–1300.

Nortek B.V. (2013). SeaDarQ Technical Details.

OceanWaves GmbH (2010). WaMoS II Data Comparison and Error Statistics.

Rijkwaterstraat (2014). Multifunctional Access Tool foR Operational Oceandata Services.

Ruessink, B., Bell, P., van Enckevort, I., and Aarninkhof, S. (2002). Nearshore Bar Crest Location Quantified from Time-Averaged X-band Radar Images. *Coastal Engineering*, 45(1):19–32.

Rutten, J. (2013). *Marine X-Band Radar Derived Wave Field Quality on an Ebb Tidal Delta*. M.Sc. Thesis, Universiteit Utrecht.

Senet, C., Seemann, J., Flampouris, S., and Ziemer, F. (2008). Determination of Bathymetric and Current Maps by the Method DiSC Based on the Analysis of Nautical X-band Radar Image Sequences of the Sea Surface (November 2007). *Geoscience and Remote Sensing, IEEE Transactions on*, 46(8):2267–2279.

Serafino, F., Lugni, C., Nieto Borge, J. C., and Soldovieri, F. (2011). A Simple Strategy to Mitigate the Aliasing Effect in X-band Marine Radar Data: Numerical Results for a 2D Case. *Sensors*, 11(1):1009–1027.

Stive, M., de Schipper, M., Luijendijk, A., Ranasinghe, R., Van Thiel De Vries, J., Aarninkhof, S., Van Gelder-Maas, C., De Vries, S., Henriquez, M., and Marx, S. (2013). The Sand Engine: A Solution for Vulnerable Deltas in the 21st Century?

Swinkels, C., Peters, H., and van Heesen, J. (2012). Analysis of Current Patterns in Coastal Areas using X-band. *Coastal Engineering Proceedings*, 1(33):currents–39.

Van Koningsveld, M., De Boer, G., Baart, F., Damsma, T., Den Heijer, C., Van Geer, P., and de Sonneville, B. (2010). OpenEarth-Inter-Company Management of: Data, Models, Tools & Knowledge. In *Beijing, China: Proceedings WODCON XIX Conference*.

Wengrove, M., Henriquez, M., de Schipper, M., Holman, R., and Stive, M. (2013). Monitoring Morphology of the Sand Engine Leeside using ARGUSS cBATHY.

Young, I. R., Rosenthal, W., and Ziemer, F. (1985). A Three-Dimensional Analysis of Marine Radar Images for the Determination of Ocean Wave Directionality and Surface Currents. *Journal of Geophysical Research: Oceans (1978–2012)*, 90(C1):1049–1059.